Three dimensional Imaging of Multiphase Flows: from Bubbles to Sneezes

by

Barry Ethan Scharfman

Submitted to the Department of Mechanical Engineering
in partial fulfillment of the requirements for the degree of

Doctor of Philosophy in Mechanical Engineering

at the

MASSACHUSETTS INSTITUTE OF TECHNOLOGY

February 2016

Author .... Signature redacted
Department of Mechanical Engineering
February 2016

Certified by .... Signature redacted
Alexandra H. Techet
Associate Professor of Mechanical and Ocean Engineering
Thesis Supervisor

Accepted by .... Signature redacted
Rohan Abeyaratne
Chairman, Department Committee on Graduate Theses

Three dimensional Imaging of Multiphase Flows: from Bubbles to Sneezes

by

Barry Ethan Scharfman

Submitted to the Department of Mechanical Engineering
on September 29, 2015, in partial fulfillment of the
requirements for the degree of
Doctor of Philosophy in Mechanical Engineering

Abstract

Experimental spray flow analysis is a difficult fluid dynamics problem because of the high optical density of many sprays. Flow features such as ligaments and droplets break off the bulk liquid volume during the atomization process and often occlude each other in images of sprays. Therefore, accurate feature detection and measurement requires advanced three-dimensional (3D) imaging techniques. In this thesis, 3D computational photographic methods including light field imaging (LFI) and synthetic aperture (SA) refocusing are combined and extended to resolve multiphase flows in 3D over time. Multiple photographs of the same scene are recorded with a large depth of field by each of the cameras in an array. After calibrating the cameras, images from each of the cameras are transformed and combined at each desired depth to construct a 3D focal stack of the scene. Each depth slice image has a narrow depth of field. Features that are physically located at a particular depth appear in focus, while objects located at other depths appear blurred.

The SA output focal stack images can be filtered to physically locate features that are small relative to the field of view. However, this task becomes more difficult for relatively larger features due to the presence of bigger out-of-focus blur artifacts. In this thesis, a Synthetic Aperture Feature Extraction (SAFE) technique has been developed to measure blobs in 3D. First, raw images from each of the array cameras are preprocessed. Blobs are detected and converted to white pixels, while the rest of the image is made black. These binary images are then refocused using a multiplicative refocusing method that only preserves the detected blobs in the neighborhood of their physical 3D location. For blobs that can be approximated as spheres, 3D centroids and radii can then be reliably extracted after post-processing the focal image stack. This process can be repeated over time while tracking particle motion. As a result, 3D spatial, size, and velocity data distributions can be calculated as functions of time to better understand the flow dynamics and characteristics. The SAFE technique has been verified using simulations and experiments involving flow of spherical soap bubbles in air.

This 3D SAFE method is also applied to the emission of mucosalivary fluid from the mouth during sneezing. Sneezes feature turbulent, multiphase flows containing potentially pathogen-bearing droplets that can play a key role in the spread of numerous infectious diseases, including influenza, SARS, and, possibly, Ebola. The range of contamination of the droplets is largely determined by their size. Despite recent efforts, no consensus on the drop size distribution from violent expirations can be found in the literature. This uncertainty inhibits a mechanistic understanding of disease transmission. Here, high-speed imaging is used to visualize previously unreported dynamics of fluid fragmentation in detail at the exit of the mouth. Droplet radii, positions, velocities, and other measurements are calculated using blob detection and tracking. This is done in two dimensions by recording the scene with a high-speed side and top camera. 3D experiments are then performed using an array of nine cameras and implementing the aforementioned 3D SAFE imaging method. The 3D sneeze data are important for a more complete understanding of the range and contamination potential of airborne disease transmission.

Thesis Supervisor: Alexandra H. Techet
Title: Associate Professor of Mechanical and Ocean Engineering

Acknowledgments

I would like to thank my family and friends both near and far for their continuous support and encouragement. I thank my advisor, Professor Alexandra Techet, for all of the guidance, support, and insights that she has provided during my time at MIT. Many thanks to Professors Douglas Hart, John Bush, and Lydia Bourouiba for their encouragement and for offering their expertise. I also appreciate the great dedication and effort put forth by all of my professors and teaching assistants in each of my MIT courses over the years. To my MIT labmates, Leah Mendelson, Abhishek Bajpayee, and Aliza Abraham - thank you for your help, advice, and friendship. I learned a great deal from you and wish you the best as you complete your graduate studies and beyond. Thanks also to all of the undergraduate students and others who helped me with my research along the way. I would not have been able to make it through my Ph.D. without Leslie Regan, Joan Kravit, Barbara Smith, and Marcia Munger - thank you for your patience and assistance. Thanks to Maria Riefstahl for all of your help and your humor.

Contents

List of Figures

List of Tables

Chapter 1

Introduction

A spray is defined as "a dynamic collection of particles, usually generated by the process of atomization" [26]. Due to the prevalence and importance of multiphase spray flows in both nature and engineering applications, many experimental, computational, and theoretical investigations have been performed [1, 25]. Even sprays generated using simple experimental setups can often be difficult to characterize mathematically and to measure experimentally due to various factors including complex interfacial physics, optical density, turbulence, thermal effects, and evaporation.

Imaging techniques are generally used to perform noninvasive measurements of sprays. Throughout most sprays the flow can be optically dense, with ligaments and droplets often occluding each other. This leads to considerable difficulty in effective image capture and analysis. Many spray imaging methods suffer from a combination of issues including complexity of the setup, limited utility in optically dense regions of sprays, constraints on the optical access to the experimental setup, and resolution in only two dimensions (2D).

Computational photographic techniques based on light field imaging (LFI) are extended here to reconstruct sprays in three dimensions (3D) over time. Synthetic Aperture Feature Extraction (SAFE) method is developed to enhance spray feature identification and analysis. The key SAFE concept involves preprocessing the raw images, recorded by multiple cameras in an array, to make them easier to refocus into a volumetric image and thus enabling the extraction of feature sizes and positions in 3D.

The SAFE method is validated through multiple camera and scene simulations and the experimental investigation of a flow of soap bubbles in air. The SAFE technique, combined with two-dimensional (2D), traditional high-speed imaging, is also applied to the study of human sneezes near the exit of the mouth. Various new sneeze flow features, including beads-on-a-string and multiple bags, are reported here for the first time. Sneeze droplet centroids, radii, and other characteristics are calculated in 3D over time.

1.1 Multiphase Flow Physics and Applications

A fluid sheet is formed when a fluid is injected into another relatively less dense fluid through a narrow slit with a thickness significantly less than its width. Figure 1-1 shows a photograph of the atomization at the underside of an angled liquid sheet that has been launched into the air. The cascade from sheet to ligaments to droplets is clearly observable.

If the slit from which liquid is emitted is circular, then a jet forms rather than a sheet. Figure 1-2 presents side and top views of the atomization of a liquid jet in a perpendicular crossflow of air. A bag instability appears along the length of the jet due to the uneven drag forces on the jet. Below the capillary length of water, single bags appear along the length of the jet. As shown in Figure 1-2, a transition and the multiple bag regime is present when the nozzle exit diameter equals and exceeds, respectively, the capillary length of water. Scharfman and Techet detected the multiple bag instability for the first time in a liquid jet in crossflow [57]. This figure also demonstrates the highly three-dimensional nature of this type of spray flow. These bags are similar to soap bubbles formed in air due to surface tension (e.g., Figure 1-3). In Figure 1-3, the bubbles are generated above the field of view and fall under the influence of gravity. A polydisperse droplet spray is formed from these bubbles when they burst as holes that form on the membrane rapidly expand.

The scale of the volume of liquid that is atomized in a spray can range from light years in astronomical settings [31] to nanometers in a biological context [10].

Figure 1-1: Photograph of atomization of a liquid sheet in air. Scale bar 1 cm.

A thorough knowledge of the physics of atomization is important for understanding the role of breakup behavior in many natural and engineering applications [39]. Ashgriz's book provides a review of the physics and applications related to sprays and jets, including a summary of relevant experimental, computational, and theoretical developments [1].

1.2 Light Field Imaging

1.2.1 Method

Fully spatially- and time-resolved experimental data is paramount for a complete understanding of spray physics. Given recent advances in camera and imaging technologies and the growing prevalence of commercially available light field imaging systems, the opportunities for obtaining such data are achievable at a lower cost and with greater resolution and computational savings. Stemming from the computer vision communities, light field imaging and synthetic aperture refocusing techniques have been combined in an emerging method to resolve three-dimensional flow fields over time [8, 9]. This technique is aptly suited for sprays, particle laden and multiphase

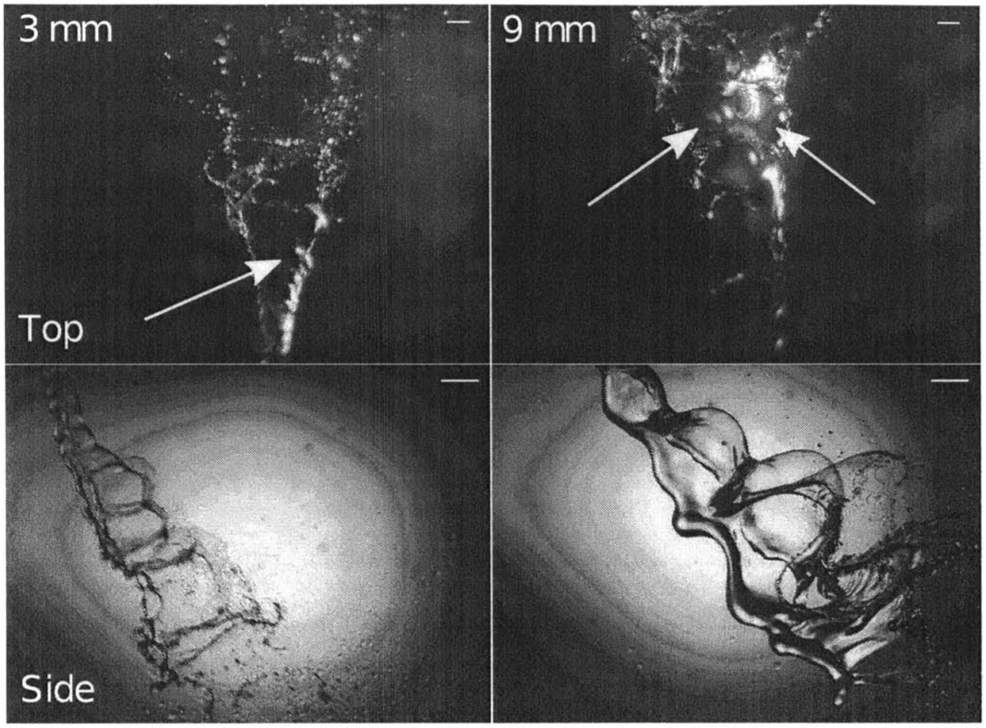

Figure 1-2: Top (first row) and side (second row) views of the multiple bag instability for 3 mm (left) and 9 mm (right) nozzle diameters for a liquid jet in a perpendicular gaseous crossflow. The arrow in the top-left image indicates the continuous sheet in the transition regime, while the arrows in the top-right image show the multiple adjacent bags. All scale bars are 1 cm.

flows, as well as complex unsteady and turbulent flows.

At the core of light field imaging, a large number of light rays from a scene are collected and subsequently reparameterized based on calibration to determine a 3D image [33]. Multiple images are captured using an array of cameras, or from a single sensor and lenslet array (i.e., a plenoptic camera). All cameras record a volumetric scene in-focus, and by recombining images in a specific manner, individual focal planes can be isolated in software to form refocused images [46, 74]. Flow features, such as individual droplets, can be located in 3D by refocusing throughout the volume and extracting features on each plane. An implication of the refocusing is the ability to "see through" partial occlusions in the scene. Utilization of this technique allows for finer measurements of flow quantities and structures that would have been impossible with prior methods.

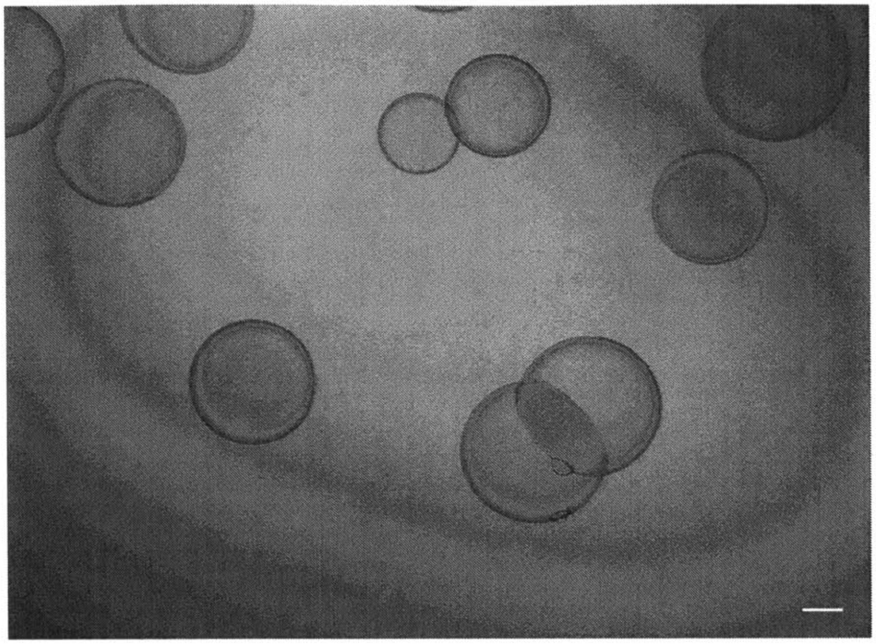

Figure 1-3: Single camera raw image of soap bubble flow in air. The bubbles are flowing from the top of the image down. Scale bar is 1 cm.

1.2.2 Implementations

In practice, one method used by researchers in the imaging community for sampling a large number of rays is to use a camera array [70, 69] or more recently, a single imaging sensor and a small array of lenses (lenslet array) in a plenoptic camera [40]. Figure 1-4 presents several examples of light field imaging arrays. The Google Jump 360 degree 16-camera circular camera array [32], a partnership between Google Inc. and GoPro, Inc., is shown at the top-left of Figure 1-4. This setup can be used to construct panoramas with 3D LFI effects. At the top-right of Figure 1-4, a 16-lens array for use in mobile phone cameras made by Pelican Imaging [22] is presented. Below that, the Raytrix [49] and Lytro [46], respectively, plenoptic cameras as shown. The Lytro is intended for consumer use to either correct "out-of-focus" images or to refocus at different depths after image capture. While the plenoptic cameras are smaller and generally less expensive than multiple camera array setups, the resolution in the depth direction is reduced because of the smaller baseline spacing between image sensors. This depth resolution is critical for resolving sprays with small flow features in 3D.

The 121-camera Stanford array [74] (shown bottom-left in Figure 1-4) is similar in setup to the nine-camera arrays used here for the SAFE technique where ultiple cameras record a scene simultaneously, which is then refocused in 3D.

1.3 Synthetic Aperture Refocusing

The fundamentals of LFI and SA refocusing methods for fluid mechanics are first outlined in Belden [8]. As described above, images of a scene are simultaneously captured by each of the cameras in the array. A checkerboard calibration grid is separately recorded by each of the cameras in different, random positions and orientations, in order to define point correspondences between the cameras and the world coordinate reference frame. Raw images from each of the cameras are mapped to each of the depth planes of interest using a homography, which is a central projection mapping between two planes. Finally, the mapped and shifted images at each depth plane are averaged in some manner to form a refocused image. The set of all of the refocused images in a particular depth range and with a specified focal plane spacing compose a 3D focal stack. By processing this volumetric image, positions and sizes of features may be extracted. Repeating this method for consecutive frames of a raw video from each of the array cameras enables particle tracking in 3D over time, from which velocities and accelerations can be calculated.

1.4 Synthetic Aperture Feature Extraction

The SA output focal stack images can be filtered to physically locate features that are small relative to the field of view [9]. However, this task becomes more difficult for larger features [61]. Using the Synthetic Aperture Feature Extraction (SAFE) technique, it is possible to measure many 3D features in a scene. Figure 1-5 presents a flowchart outlining the SAFE process. First, raw images from each of the array cameras are preprocessed: blobs are detected and converted to white pixels, while the rest of the image is made black. Since the method is best suited to the recon-

Figure 1-4: Light field imaging hardware implementations. Clockwise from top left: Google Jump 360 [32] degree circular camera array consisting of 16 GoPro cameras (credit: Will Shanklin/Gizmag), Pelican Imaging depth sensor array embedded in a cell phone [22], Raytrix [49] and Lytro [46] plenoptic cameras, respectively, and Stanford light field camera array [74].

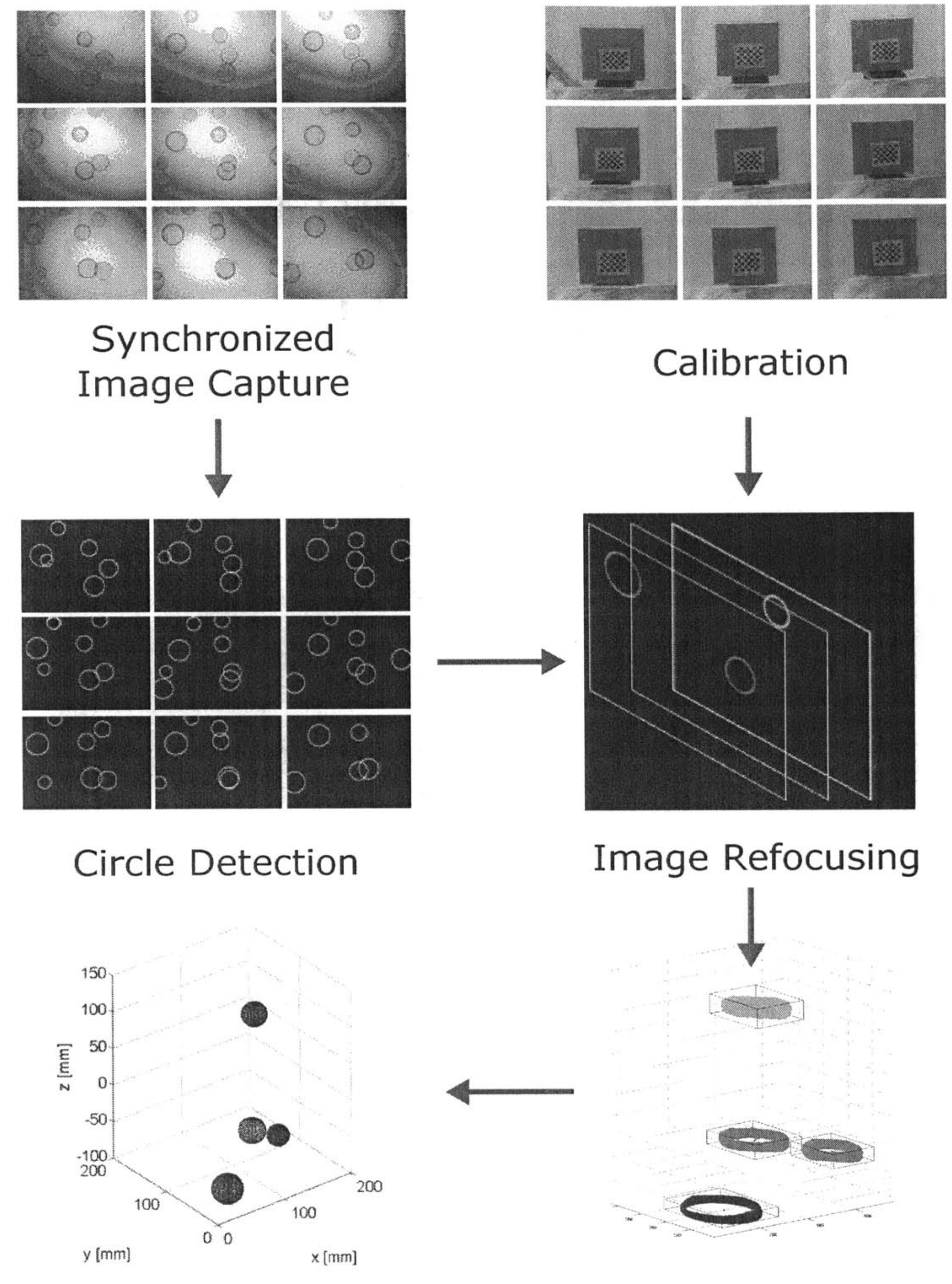

Figure 1-5: Light field imaging and Synthetic Aperture Feature Extraction flowchart, reproduced from [60].

struction of circular blobs, features that do not resemble circles may be filtered out to improve accuracy. These binary images are then refocused either using a multiplicative refocusing method or additive refocusing [8] combined with thresholding. In the multiplicative method, each transformed image is first raised to a power, and then the product of corresponding pixels in each of the images is calculated. Using the additive approach, the mean of the transformed images at each depth is used. The resulting refocused slice at each depth plane may be thresholded to remove pixels representing only a slight overlap of the images recorded by the array cameras.

Clusters are detected in the volumetric image. The centroids and effective radii of these clusters at their central depth planes are used to reconstruct spheres in 3D. This process can be repeated over time while tracking particle motion. As a result, 3D spatial, size, and velocity data distributions can be calculated as functions of time to better understand the flow dynamics and characteristics. The SAFE technique has been verified using both simulations and experiments consisting of a flow of spherical soap bubbles in air [59, 58, 60].

SAFE has also been validated for both light field and dark field setups, featuring direct and indirect scene illumination, respectively [61]. Dark field imaging produces essentially binary images directly and eliminates the need for more complex blob detection during preprocessing. Light field imaging is generally more cost effective because the scene can be illuminated from a single location (directly behind the scene), rather than surrounding the objects being recorded. When fast-pulsed lighting is needed, e.g., for high-speed flows, the dark field method could be significantly more expensive to implement. In addition, the increase in computational expense is small for the preprocessing required in the light field versus dark field setup.

1.5 Analysis of Sneeze Ejecta

The emission of mucosalivary fluid from the mouth during sneezing is an example of a complex spray flow. Sneezes feature turbulent, multiphase flows containing potentially thousands of pathogen-bearing droplets that can play a key role in the spread

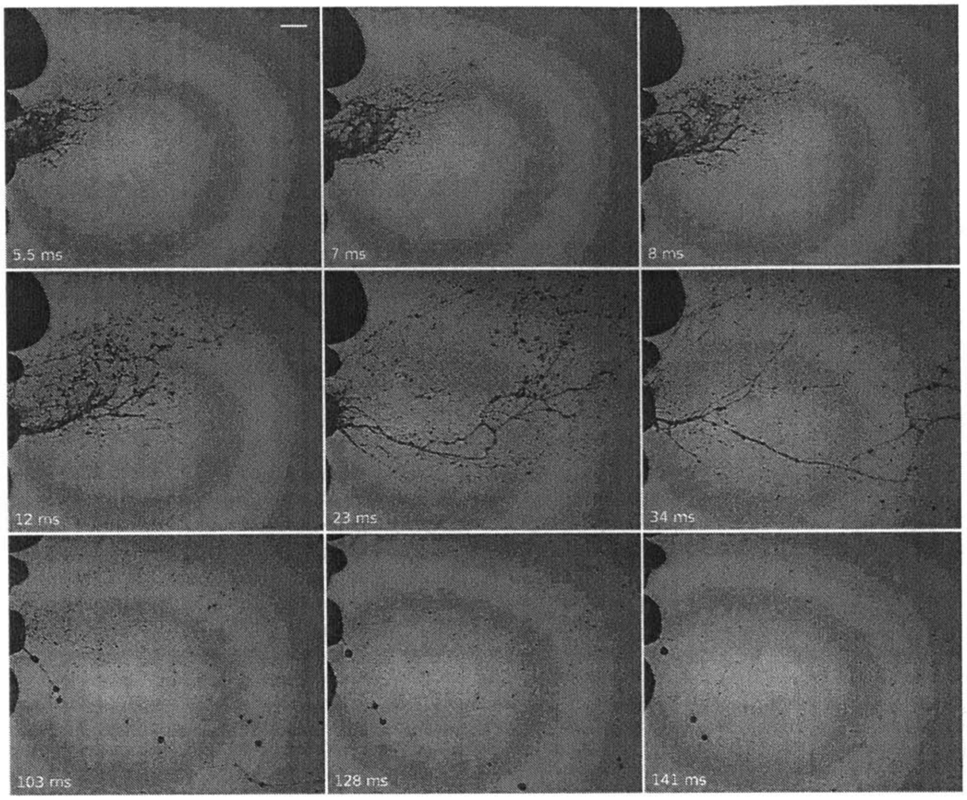

Figure 1-6: Side view sequence of the fluid ejected from the mouth of a healthy male while sneezing. Three phases are observed. Top rows: First, sheets of fluids are ejected. Middle rows: Second, the sheets break into ligaments. Bottom rows: Third, droplets are formed from the breakup of the ligaments. Scale bar is 1 cm.

of numerous infectious diseases, including influenza, SARS, and, possibly, Ebola [16]. The range of contamination of the droplets is largely determined by their size. Despite recent efforts, no consensus on the drop size distribution from violent expirations can be found in the literature. This uncertainty inhibits a mechanistic understanding of disease transmission.

Direct observations of the physical mechanisms involved in droplet formation during sneezing are reported in this thesis. Traditional 2D high-speed imaging is utilized to visualize the dynamics of fluid fragmentation in detail at the exit of the mouth. This work builds upon that of Bourouiba, Dehandschoewercker, and Bush [16], in which the cloud of droplets generated during coughs and sneezes are analyzed. Fluid sheets and bags break into ligaments, which then separate into droplets. These frag-

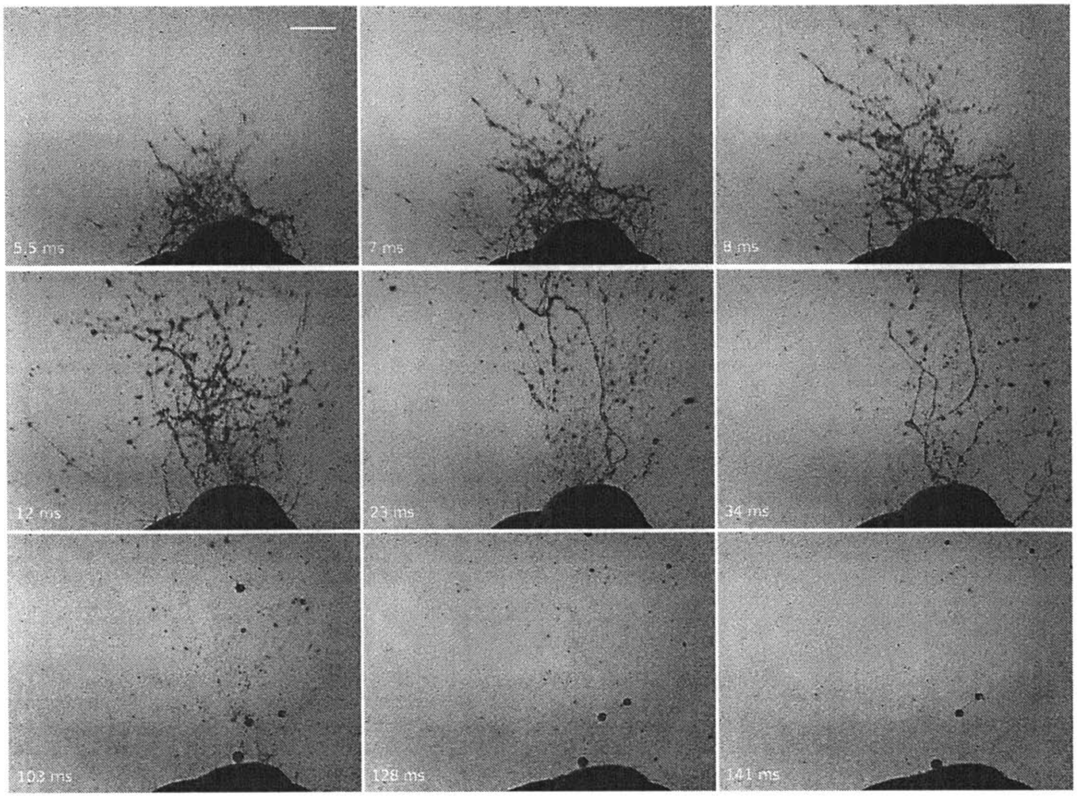

Figure 1-7: Top view of the same sneeze shown in Figure 1-6. Scale bar is 1 cm.

mentation steps share analogous governing physics with the fragmentation processes reported in some industrial applications. Insight into the dynamics shaping the final size distribution of droplets generated by sneezes and coughs can be gained by analyzing these fragmentation phases.

Figure 1-6 presents a side view sequence of the fluid ejected from the mouth of a healthy male, recorded at 8000 frames per second (fps). The corresponding top view of the same sneeze, which was recorded at 2000 fps, is shown in Figure 1-7. Three phases are observed. The top rows show the sheets of fluids that are initially ejected. Second, the sheets break into ligaments (as seen in the middle rows of these figures). Finally, the bottom rows of these figures show daughter droplets being formed from the breakup of the ligaments. Figure 1-8 shows droplets being formed during beads-on-a-string formation.

Figure 1-8 displays the beads-on-a-string phenomenon during sneezing. The bot-

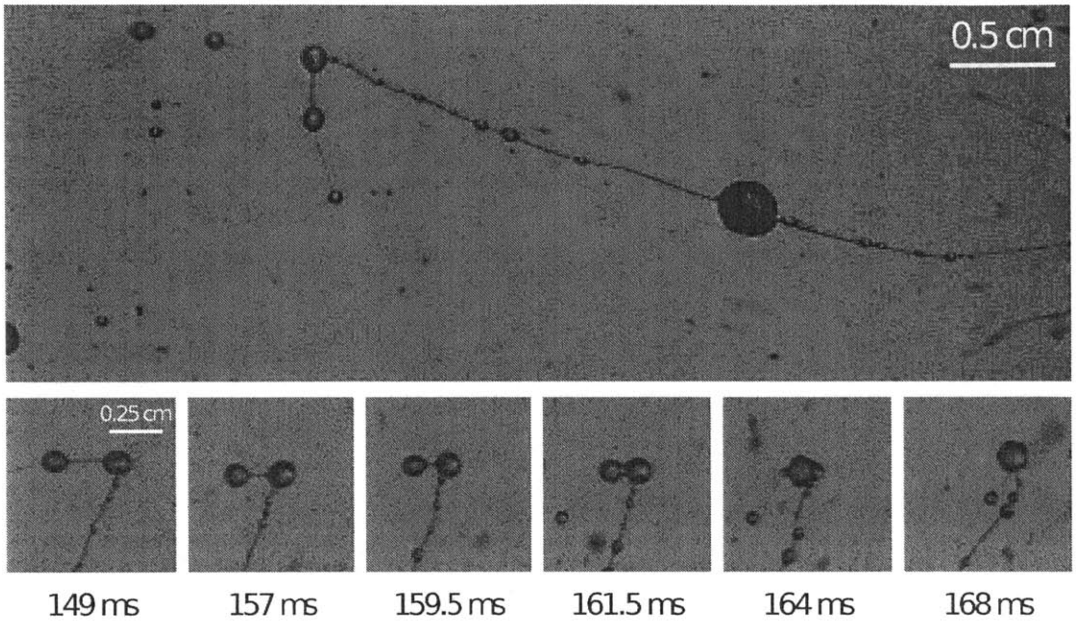

149 ms 157 ms 159.5 ms 161.5 ms 164 ms 168 ms

Figure 1-8: Beads on a string found in sneeze ejecta ligaments. Top: Multi-scale droplets or "pearls" form on stretching ligaments owing to the influence of non-Newtonian effects. Bottom: Time sequence showing two consecutive mergers of adjacent pearls. This particular sequence is observed on the largest ligament shown in the top part of the figure, which has a width of about 0.2 mm.

tom panel of this figure displays a 90-degree clockwise rotated view of droplet coalescence due to viscoelasticity at the left of the mucus ligament in the top panel. The bead merger and breakup along ligaments influences the overall droplet size distribution in a sneeze.

To better understand the 3D nature of sneeze ejecta, the SAFE method is used with an array of nine high-speed cameras. An additional high-speed camera is utilized to track the motion of the head during sneezing. The reconstructed 3D droplet centroids and radii enable a more complete understanding of the physical extent and fluid dynamics of sneeze ejecta. By tracking the droplets over time, velocities and accelerations can also be calculated. These measurements are important for understanding the airborne disease transmission potential of sneezes and can be used to develop or validate theories and numerical simulations.

1.6 Outline of Thesis

Experimental methods and results are presented in subsequent chapters. Chapter 2 discusses the development of the SAFE method for detecting the centroids and sizes of blobs in a 3D scene. Simulations using the open source software package Blender [18] and experiments using soap bubble flows in air are utilized to validate this approach.

In chapter 3, a 2D experimental analysis of sneeze ejecta is presented. Blobs are detected in high speed videos of a human subject sneezing. These videos are recorded from both a side and top view of the scene. This investigation examines the individual droplets in the spray close to the mouth. Previously unobserved phenomena and instabilities are observed in this multiphase, non-Newtonian flow.

Chapter 4 describes the application of the SAFE method to 3D reconstructions of high-speed sneeze ejecta videos. Scenes are recorded simultaneously with nine cameras arranged in a rectangular array. Blobs are detected in the raw images, which are then preprocessed before being refocused to form a 3D reconstruction. Droplet centroids and radii can then be extracted and features can be tracked over time. Various flow parameter distributions are also measured.

Finally, Chapter 5 presents overall conclusions for the thesis. The capabilities of the SAFE method and the physical insights about sneeze ejecta that have been gained are summarized, and avenues for future work are outlined.

Chapter 2

Three-Dimensional Synthetic Aperture Feature Extraction in Multiphase Flows

2.1 Introduction

In this chapter, the Synthetic Aperture Feature Extraction (SAFE) method, which can be used to resolve multiphase flows, is discussed in detail. Specifics of the method used and advantages and limitations are discussed herein. Further results using this technique are presented in Chapter 4.

Stemming from the computer vision communities, light field imaging (LFI) and synthetic aperture (SA) refocusing techniques have been combined in an emerging method to resolve three-dimensional (3D) flow fields over time [8]. This technique is aptly suited for sprays, particle laden and multiphase flows, as well as complex unsteady and turbulent flows. LFI involves a large number of light rays from a scene being collected and subsequently reparameterized based on calibration to produce a 3D image [33]. In practice, one method used by researchers in the imaging community for sampling a large number of rays is to use a camera array [69, 70] or, more recently, a single imaging sensor and a small array of lenslets (lenslet array) in a plenoptic camera [40].

Light field imaging involves the reparameterization of images captured using an array of cameras, or from a single senor and lenslet array, to digitally refocus a flow field post-capture. All cameras record a volumetric scene in-focus, and by recombining images in a specific manner, individual focal planes can be isolated in software to form refocused images. Flow features, such as individual droplets, can be located in 3D by refocusing throughout the volume and extracting features on each plane. An implication of the refocusing is the ability to "see through" partial occlusions in the scene. Initial applications by Belden et al. [8] also proved that these techniques are viable for quantitative flow measurements when combined with 3D particle imaging velocimetry (PIV) algorithms. High-speed cameras were used by Belden et al. [9] with similar success for bubbly flows but with significant equipment cost increase. Techet et al. [67] discuss the application of these techniques to the atomization of a turbulent sheet in air as well as other spray flow conditions. On the underside of the turbulent sheet, breakup is analyzed using LFI and SA techniques. Issues preventing the extraction of complete droplet shape, size, and position information using these techniques are discussed. Mendelson and Techet [42] have applied the SA method to perform 3D PIV analysis on freely swimming fish. Bajpayee and Techet [4] used simulations to demonstrate the applicability of similar techniques to particle tracking velocimetry (PTV).

Dark field imaging is a technique that relies on indirect illumination of a scene, rather than having light pass through the object being imaged into the camera lens. This method has traditionally been used in microscopy to image lightly-colored or translucent subjects. Zsigmondy [77] developed the first ultramicroscope, or dark-field microscope, in 1903. Sipperley and Bachalo [64] discuss an application of dark field imaging to a solid object along with considerations relevant for imaging spray flows. They utilized lighting surrounding the target and recorded images of it at different positions and focal depths with a single camera to simulate the concept of inserting multiple complementary metal-oxide-semiconductor (CMOS) sensors into a single multi-focal plane camera.

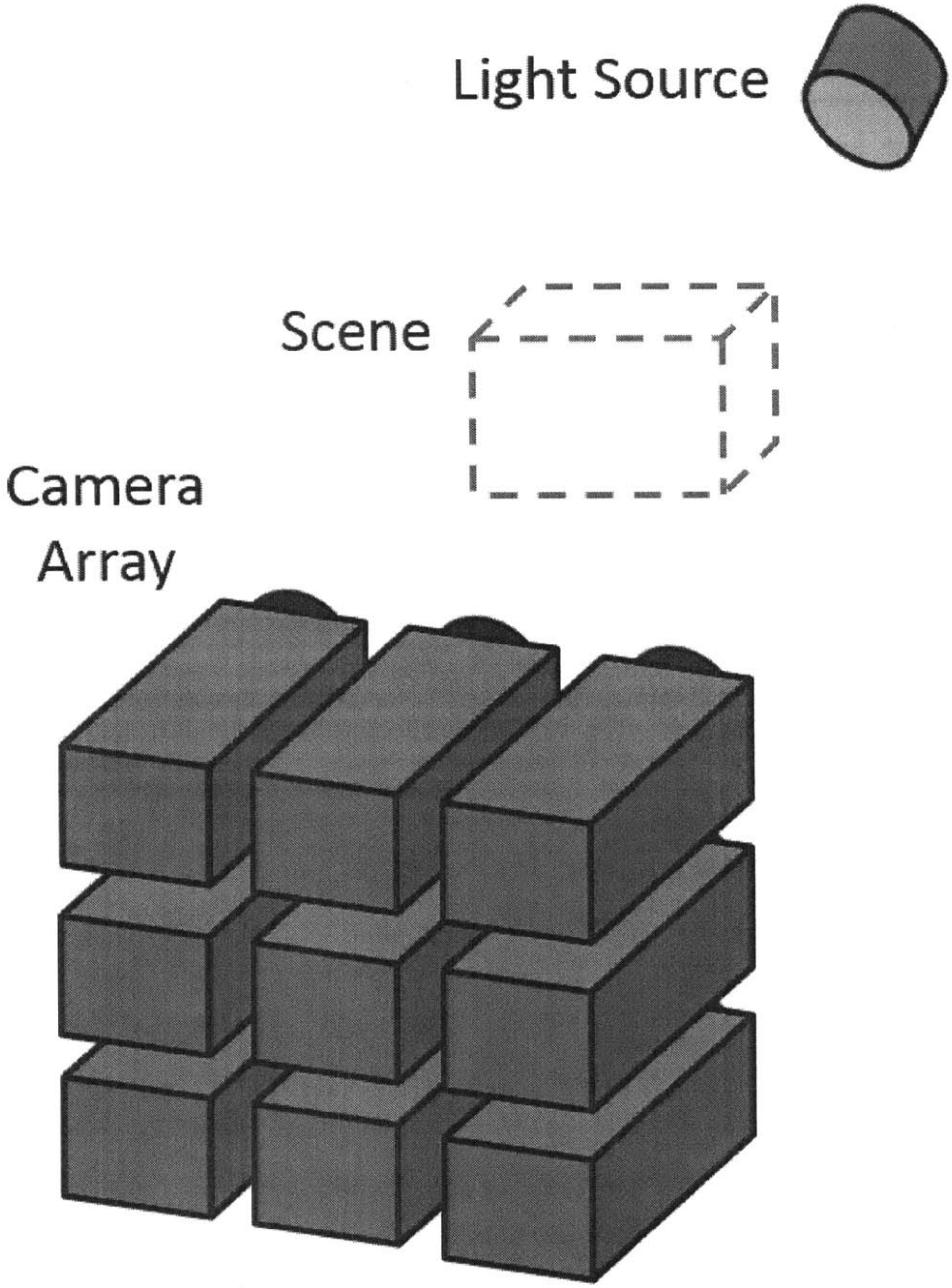

Figure 2-1: Three-dimensional light field imaging experimental setup schematic.

A dark field imaging technique has been developed by Scharfman et al. [61] that relies on the use of a camera array and synthetic aperture refocusing techniques. This method has been tested using simulations of the cameras and lights that would be used in an actual experimental setup. The essentially binary images that are produced allow for simpler image post-processing and the extraction of center coordinates and radii of imaged spheres in 3D. This method is useful for finding droplet or bubble size and location distributions in 3D space over time.

Although this dark field imaging technique simplifies the task of feature extraction, a more expensive and complex experimental setup is required than in LFI due to the need to have lights surrounding the scene. Such a lighting setup is not always feasible due to spatial constraints. Scharfman and Techet [58, 60] have demonstrated that it is possible to extract features using an LFI setup with a backlit scene. Raw camera images from the array are binarized prior to the application of the SA refocusing algorithm. After these binary images are refocused, spheres are formed from centroid and radius data that are extracted from the reconstructed image volumes. The results obtained from this new method match those reached using the dark field setup, but at lower potential cost and without significant increase in computation time.

Here, the SAFE LFI method is applied to 3D simulations of particles with various volume fractions are used to assess 3D reconstruction error. In addition, this technique is applied to an experimentally produced polydisperse bubble field in air. 3D positions and radii of the bubbles are extracted from the refocused, processed image volume. Using this information, the 3D scene can be reconstructed and feature sizes, shapes, and velocities of particles can be calculated. Bubbles are an ideal experimental test case because the feature borders are sharply defined and bubbles can easily be seen behind each other even if they are partially occluded. The 3D bubble locations can also be found by refocusing the raw images of the bubbles themselves. However, for more complex droplet sprays, the feature boundaries may not be as easily observable, especially in the presence of occlusions. In this case, refocusing the preprocessed binary images would yield improved results.

2.2 LFI and SA Refocusing

The starting point for volume reconstruction is the implementation of the synthetic aperture algorithm to generate refocused images on planes throughout the volume. Thereafter, the actual particle field must be extracted from the refocused images and organized into a volume with quantifiable locations. First, mapping functions must be established between the camera image planes and world coordinates

$$\mathbf{u}^i{}_j = F(\mathbf{X}_j; p^i) \tag{2.1}$$

where $\boldsymbol{u}_j$ is the 2x1 vector of the j^{th} image point coordinates, $[u_j, v_j]^T$, $\boldsymbol{X}_j$ is the 3x1 vector of the j^{th} world point coordinates, $[X_j, Y_j, Z_j]^T$, p^i is a set of parameters defining the model of the i^{th} camera, and F defines the form of the model. This model allows each image from each of the N cameras in the array to be projected onto k focal planes. I_{FPki} denotes the image from camera i aligned on the k^{th} focal plane. The resulting, refocused SA image, I_{SAk}, may be generated by averaging each of these images over the number of cameras in the array

$$I_{SAk} = \frac{1}{N}\sum I_{FPki} \tag{2.2}$$

where I_{SAk} is the image from camera i aligned on the k^{th} focal plane [8]. Combining images using this averaging technique is known as additive refocusing. A variant of the additive SA algorithm that can enhance the signal-to-noise ratio for well calibrated images is given by the multiplicative refocusing algorithm

$$I_{SAk} = \prod_{i=1}^{n}[(I_{FPki})^n] \tag{2.3}$$

where n is an exponent between 0 and 1. This allows for enhancement of the signal-to-noise ratio without letting any camera with an occluded view of an object prevent that object from being refocused. This is because a small number raised to an exponent between 0 and 1 is non-zero. For ordinary light field SA refocusing, it has been

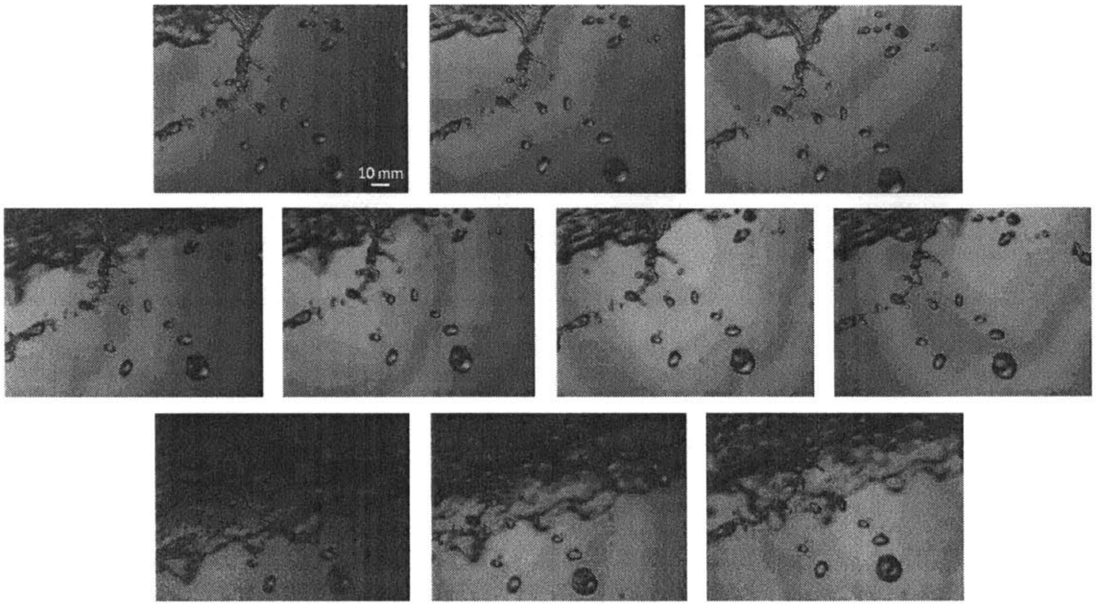

Figure 2-2: Raw images from individual cameras at a particular instant in time (reproduced from [61]). Image positions correspond to physical camera positions when looking head-on at the array.

determined that n in the range of $\frac{1}{5} \leq n \leq \frac{1}{3}$ works best.

Although the location and size of in-focus features in a particular plane of focus can be detected, feature centroids and complete shapes cannot be fully reconstructed using the LFI SA refocusing method described above. The apparent extent of features like droplets and ligaments in the depth direction is larger than the true depth due to the out-of-focus blur. This blur also creates blur artifacts, or "ghosts," that complicate the extraction of in-focus features at each plane.

Figures 2-2 and 2-3 illustrate an example of this ghosting issue. Raw images of a spray recorded by an array of ten cameras are shown in Figure 2-2. These ten individual camera images are processed using the multiplicative refocusing method with a multiplicative exponent of 1/5 (Eq. 2.3). Sample refocusing results are shown in Figure 2-3 at various depths throughout the focal stack. Features that are in focus at each particular plane in the Z (depth) direction are indicated. Negative Z values indicate image planes that are in front of the reference plane (closer to the camera array) at the center of the volume of interest, while positive values of Z are behind

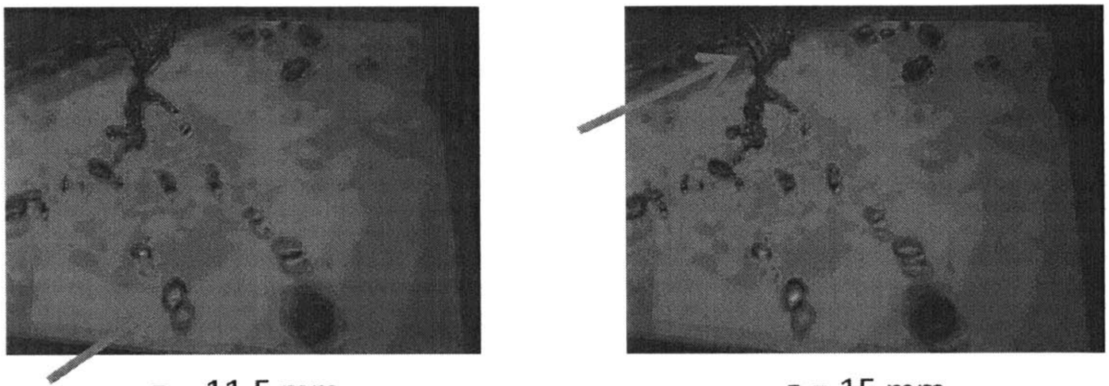

z = 11.5 mm

z = 15 mm

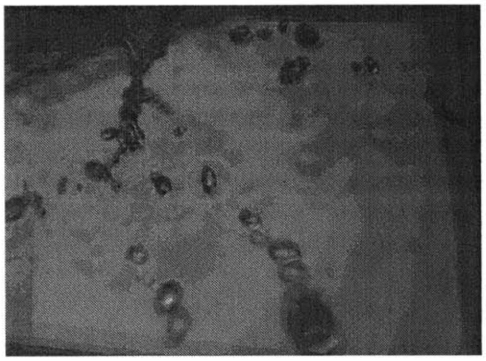

z = 18.5 mm

Figure 2-3: Synthetic aperture refocused images corresponding to the raw images in Figure 2-2 (reproduced from [61]). The arrows and circle indicate features that are in focus at the particular planes shown.

the reference plane. The features that appear to be blurred are actually located at a different depth in the volume and are not in focus on that Z plane. The identification of the plane(s) of focus of particular features allows their positions in the volume to be determined.

In Figure 2-3, it can be seen that these ghosts are large and often make it impossible to perceive which shapes are actually in focus at a particular depth plane. Ghosts from other features are often also located at the same X-Y position as in-focus features in many of the planes, which also cause difficulty in processing the images to find sharp features. In this Figure, ghosting from the sheet is present in the background of other in-focus droplets and ligaments. Although it has been demonstrated that it is possible to refocus through the reconstructed image volume, prior experimental results have revealed several important difficulties in the extraction of 3D flow features when using a relatively small number of cameras [61]. The presence blur pattern artifacts limits the feasibility of extracting flow features via image processing. While it has been shown that it is possible to remove these artifacts of the blur pattern for PIV and the tracking of particles that are small relative to the field of view [8, 9], this removal becomes more challenging when the artifacts are larger and are overlapping.

2.3 Synthetic Aperture Feature Extraction (SAFE)

2.3.1 SAFE Dark Field Imaging

Spherical objects can be reconstructed by modifying the lighting setup so that a dark field, rather than a light field, approach is utilized. This method is identical to that described in the previous section, except no light enters the cameras in the array directly. Rather, lights are placed around the scene with a black sheet blocking any light directly opposite the cameras. This results in essentially binary images containing solid white shapes on a black background. Using the multiplicative refocusing method in Eq. 2.3, the out-of-focus "ghosts" are eliminated. This is because a pixel value of zero for the black background in even one camera image from the array will produce a value of zero for that pixel in the reconstructed volume. As a result, only fully in-focus features appear at each depth slice in the refocused volume as white blobs that can be extracted via image analysis. Although this method eliminates shading information, it is beneficial because it simplifies the image analysis. Similar results can be achieved using additive refocusing (Eq. 2.2) and thresholding.

2.3.2 SAFE Light Field Imaging

Scharfman and Techet have shown that similar binary input images and refocused results can be produced using a light field backlit experimental setup [58, 59]. LFI can be more cost effective than dark field imaging because lights must only be located behind, rather than surrounding, the scene being imaged. Figure 2-4 provides a flowchart of the SAFE method image processing pipeline, and Algorithm 1 displays more details about each step. Raw images are captured simultaneously by each camera in the array. If video is being recorded rather than single snapshots, then the following process is repeated for each frame of the video. Features must first be detected in the raw images. The feature pixels are then converted to white, while the background is made black. Any feature detection approach may be used, and the one that best suits the data should be selected for the most accurate 3D reconstruction. For instance, a Circular Hough Transform (CHT) [2] based algorithm has been applied to the detection of bubbles that are known to generally have a circlular shape [58]. For blob-like features, especially those with irregular shapes, the maximally stable extremal regions (MSER) algorithm [41] can also be effective. MSER locates features of interest in an image by testing for region stability over a variety of threshold values.

The binary images are then transformed based on the camera array calibration results and refocused using either the additive (Eq. 2.2) or multiplicative (Eq. 2.3) refocusing method. The resulting focal stack extends in the z depth dimension from z_{min} to z_{max} with an increment of dz between successive focal slices. If necessary, the intensities of the voxels in the focal stack may be thresholded. True detected features will generally have higher intensities than false blur artifacts due to the

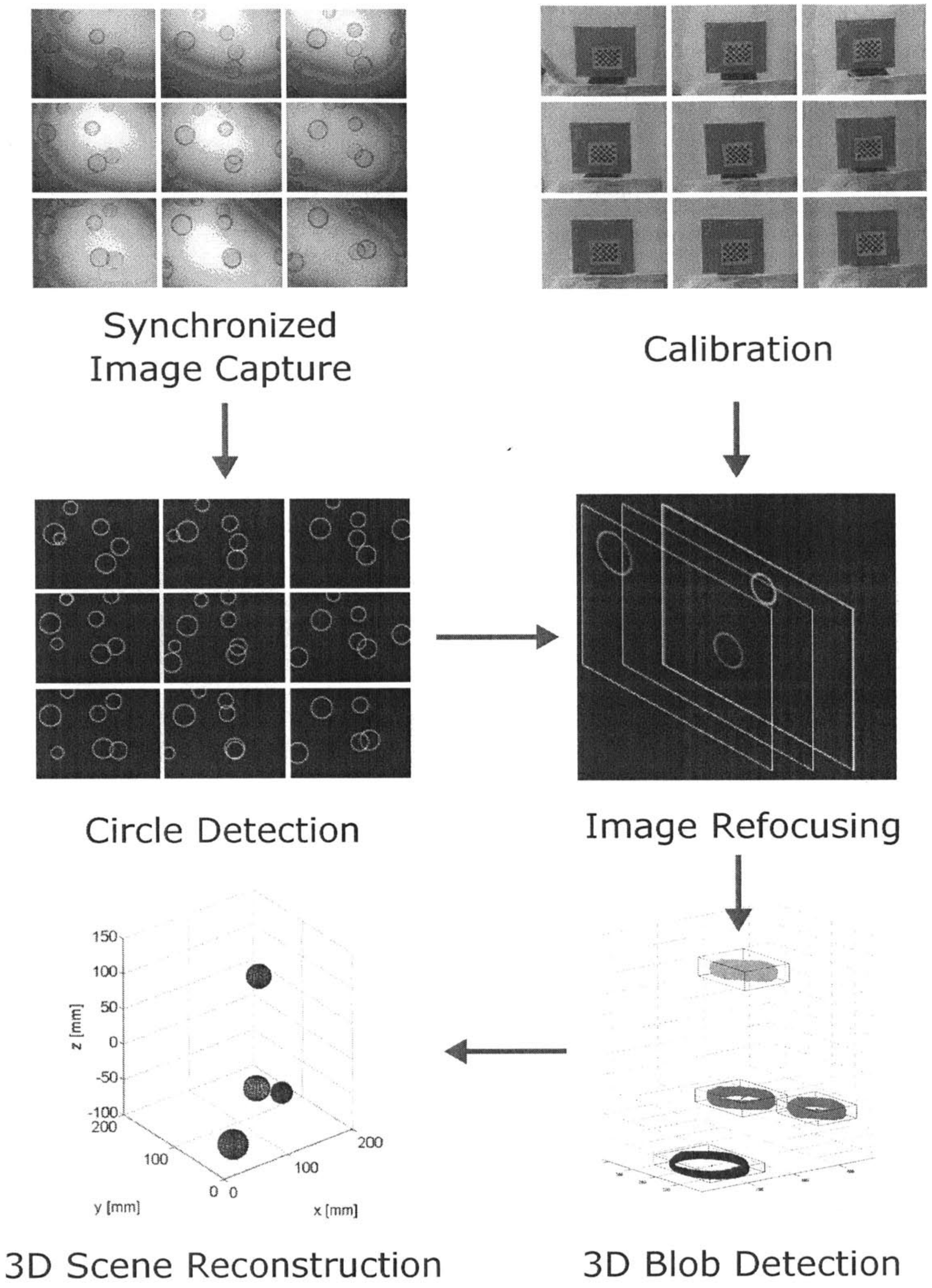

Figure 2-4: Light field imaging and Synthetic Aperture Feature Extraction flowchart, reproduced from [60].

Algorithm 1 SAFE LFI

```
for each time step do
    for each image from each camera do
        Perform any necessary preprocessing.
        Detect features.
        Convert feature pixels to white and all other pixels to black.
    end for
    Refocus the binary images from all cameras.
      Use additive (Eq. 2.2) or multiplicative (Eq. 2.3) refocusing.
    Filter focal stack.
      Threshold intensity.
    for $z := z_{min}$ to $z_{max}$ step $dz$ do
        Find $(X, Y)$ coordinates of voxels.
    end for
    for each nonzero voxel in focal stack do
      Search for the next unlabeled voxel, $p$.
      Use flood-fill to label all voxels in connected component containing $p$.
    end for
    for each cluster do
      if number of voxels in cluster is below threshold then
          Remove cluster.
      else
          Find geometric centroid.
          Estimate size of particle from depth plane containing centroid.
      end if
    end for
end for
```

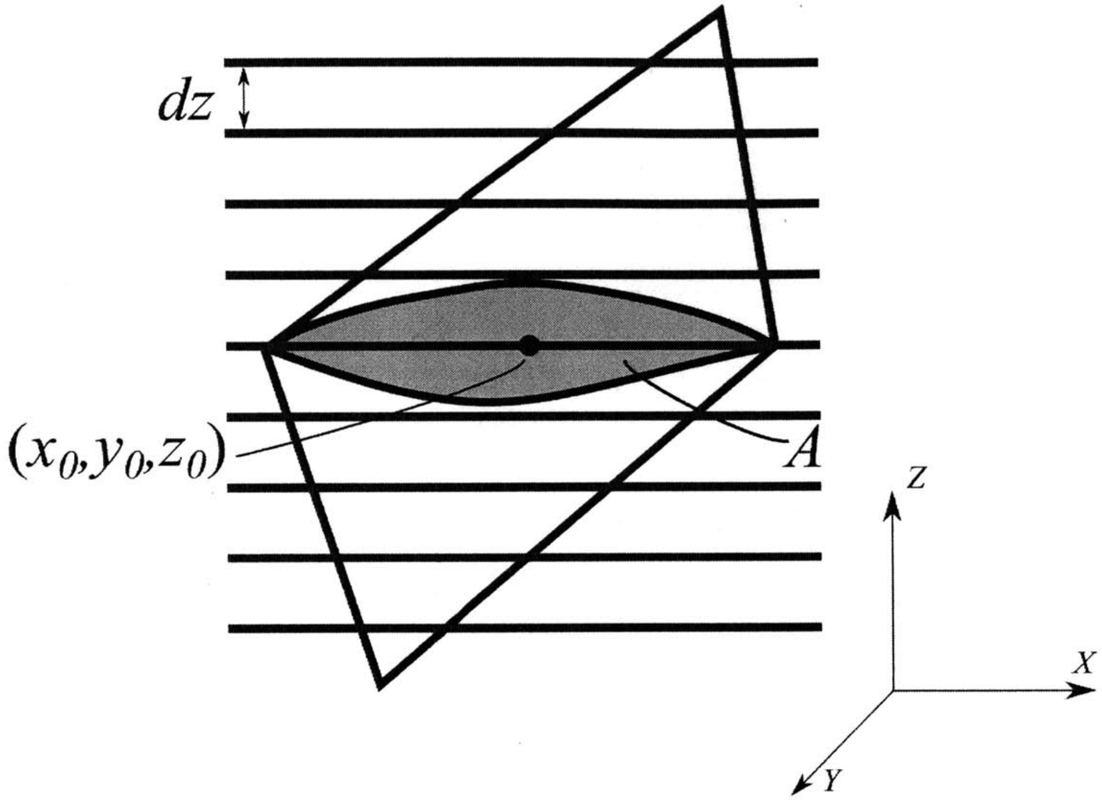

Figure 2-5: Z depth slices drawn through a cluster extracted from a focal stack. The centroid of the cluster is $[x_0, y_0, z_0]^T$. A is the area corresponding to the boundary of voxels lying in the Z depth slice containing the centroid. $[x_0, y_0, z_0]^T$ is the centroid of the actual feature corresponding to the cluster. The length scale of the feature is proportional to $\sqrt{A}$ if the true particle is nearly spherical.

greater overlap of transformed binary images from each camera. After thresholding, all nonzero voxels in the focal stack are located. A flood-fill algorithm is used to associate all voxels in connected components with the corresponding cluster ID. A minimum voxel size per cluster threshold can be set to eliminate small clusters if this reduces the presence of noise. Finally, the geometric centroid of each cluster is calculated (see Figure 2-5). This is considered to be the true particle centroid, and the particle size is estimated from the area, A, of the cluster depth plane containing the centroid. If particles are nearly spherical, then the radius is proportional to $\sqrt{A}$.

2.3.3 Volume of Interest Extrema

When refocusing an image volume, a practical consideration is the physical boundaries of the volume of interest. Refocusing beyond these boundaries can lead to incorrect 3D reconstructions because there are no in-focus features to be detected in these outer regions. In addition, processing a greater volume than necessary can potentially lead to a substantial increase in computational cost. An upper limit on the extent of the volume in each dimension can be calculated by examining the intersection of rays emanating from the cameras with planes passing through the world coordinates origin. Figure 2-6 depicts two cameras pointed at a scene. The camera center vector in world coordinates is denoted by $[X_0, Y_0, Z_0]^T$. w and h define the physical width and height of each camera's horizontal and vertical field of view, respectively. The conversion factor from pixels to physical units is determined during calibration. Rays are drawn from the four corners of each camera image projection in the direction of the scene being imaged. The position vector corresponding to the j^{th} corner of a particular camera is denoted by $\boldsymbol{p}_j$. The default orientation of each camera is assumed to be in the $+Z$ direction, and then the camera and its corner rays are rotated about its center of projection into the camera orientation direction determined by calibration. The camera matrix for each camera, denoted by P, is determined from calibration [8, 29]. In the absence of refractive interfaces, the pinhole calibration model may be used. The equation for the projection of world points onto the image plane is

$$\begin{gathered} P = KR[I| - \mathbf{X}_{cam}] = K[R|\boldsymbol{t}] \\ [R|\boldsymbol{t}] = K^{-1}P, \end{gathered} \tag{2.4}$$

where P is the 3x4 pinhole camera matrix, R is the 3x3 rotation matrix, I is the 3x3 identity matrix, $\boldsymbol{X}_{cam}$ are the Cartesian coordinates of the camera center expressed in the world coordinate frame, and $\boldsymbol{t}$ is the translation vector. $[R|\boldsymbol{t}]$ is the extrinsic camera matrix. K is the 3x3 intrinsic camera calibration matrix, defined as

$$K = \begin{bmatrix} -b & 0 & u_0 \\ 0 & -b & v_0 \\ 0 & 0 & 1 \end{bmatrix}, \tag{2.5}$$

where b is the focal length in pixels, and u_0 and v_0 are the principal point offsets in the horizontal and vertical directions. The camera center vector, $[X_0, Y_0, Z_0]^T$, is defined as

$$\boldsymbol{X}_{cam} = \begin{bmatrix} X_0 \\ Y_0 \\ Z_0 \end{bmatrix} = -R^{-1}\boldsymbol{t} = -R^T\boldsymbol{t}. \tag{2.6}$$

The camera orientation vector components, A, B, and C, are equal to the third row elements of the rotation matrix, respectively:

$$\begin{bmatrix} A \\ B \\ C \end{bmatrix} = R^T \begin{bmatrix} 0 \\ 0 \\ 1 \end{bmatrix} = \begin{bmatrix} R_{3,1} \\ R_{3,2} \\ R_{3,3}. \end{bmatrix} \tag{2.7}$$

In order to find the intersection points of the rays emanating from the four camera corners, the camera corner points must be rotated in the direction of the local camera axis, which is in the $+Z$ direction. The four original (unrotated) corner points of the camera image area in physical units are

$$\boldsymbol{p}_{original} = \begin{bmatrix} X_0 \\ Y_0 \\ Z_0 \end{bmatrix} + \left\{ \begin{bmatrix} -w/2 \\ h/2 \\ 0 \end{bmatrix}, \begin{bmatrix} w/2 \\ h/2 \\ 0 \end{bmatrix}, \begin{bmatrix} w/2 \\ -h/2 \\ 0 \end{bmatrix}, \begin{bmatrix} -w/2 \\ -h/2 \\ 0 \end{bmatrix} \right\}. \tag{2.8}$$

The required rotation angle, θ, to properly orient the camera is calculated as

$$\theta = acos(\begin{bmatrix} A \\ B \\ C \end{bmatrix} \cdot \begin{bmatrix} 0 \\ 0 \\ 1 \end{bmatrix}) = acos(C) \tag{2.9}$$

and $\boldsymbol{r}$ is the corresponding rotation axis, which is

$$\boldsymbol{r} = \begin{bmatrix} r_X \\ r_Y \\ r_Z \end{bmatrix} = \begin{bmatrix} A \\ B \\ C \end{bmatrix} X \begin{bmatrix} 0 \\ 0 \\ 1 \end{bmatrix} = \begin{bmatrix} B \\ -A \\ 0 \end{bmatrix}. \qquad (2.10)$$

The 3D rotation matrix, M, corresponding to $\boldsymbol{r}$ is defined as

$$M = \begin{bmatrix} (1-c_\theta){r_X}^2 + c_\theta & (1-c_\theta)r_X r_Y - s_\theta r_Z & (1-c_\theta)r_X r_Z + s_\theta r_Y \\ (1-c_\theta)r_X r_Y + s_\theta r_Z & (1-c_\theta){r_Y}^2 + c_\theta & (1-c_\theta)r_Y r_Z - s_\theta r_X \\ (1-c_\theta)r_X r_Z - s_\theta r_Y & (1-c_\theta)r_Y r_Z + s_\theta r_X & (1-c_\theta){r_Z}^2 + c_\theta \end{bmatrix}, \qquad (2.11)$$

where c_θ and s_θ are the sine and cosine of the rotation angle. By substituting the values from Eq. 2.10, M becomes

$$M = \begin{bmatrix} B^2(1-c_\theta) + c_\theta & -AB(1-c_\theta) & -As_\theta \\ -AB(1-c_\theta) & A^2(1-c_\theta) + c_\theta & -Bs_\theta \\ As_\theta & Bs_\theta & c_\theta \end{bmatrix}. \qquad (2.12)$$

The mean X, Y, and Z coordinates of the rotated camera corner points are

$$\begin{bmatrix} \hat{p}_X \\ \hat{p}_Y \\ \hat{p}_Z \end{bmatrix} = \frac{1}{4}\sum_{j=1}^{4} M\boldsymbol{p}_{j,original}, \qquad (2.13)$$

where $\boldsymbol{p}_{j,original}$ is the j^{th} camera corner point position vector. The rotated corner point vectors can then be calculated as

$$\begin{bmatrix} p_{X,j} \\ p_{Y,j} \\ p_{Z,j} \end{bmatrix} = M\boldsymbol{p}_{j,original} - \begin{bmatrix} \hat{p}_X \\ \hat{p}_Y \\ \hat{p}_Z \end{bmatrix} = M\boldsymbol{p}_{j,original} - \frac{1}{4}\sum_{j=1}^{4} M\boldsymbol{p}_{j,original}. \qquad (2.14)$$

Parametric line equations for each rotated camera corner ray are

$$\begin{aligned} X_j(s) &= p_{X,j} + As \\ Y_j(s) &= p_{Y,j} + Bs \\ Z_j(s) &= p_{Z,j} + Cs, \end{aligned} \tag{2.15}$$

where s is the parameter variable. The Z focal bounds can finally be calculated by examining the intersection of each of the camera rays with a plane cutting through the world origin. For instance, at the plane $Y = 0$:

$$s = -\frac{p_{Y,j}}{B}. \tag{2.16}$$

The Z coordinate at the intersection of the plane $Y = 0$ is then

$$Z_j(-\frac{p_{Y,j}}{B}) = p_{Z,j} - \frac{C}{B}(p_{Y,j}). \tag{2.17}$$

Similarly, the X coordinate at the intersection of the plane $Y = 0$ is

$$X_j(-\frac{p_{Y,j}}{B}) = p_{X,j} - \frac{A}{B}(p_{Y,j}). \tag{2.18}$$

By setting $X = 0$, the Y intersection points may be calculated. At the plane $X = 0$,

$$s = -\frac{p_{X,j}}{A}. \tag{2.19}$$

Then, the y intersection points are

$$Y_j(-\frac{p_{X,j}}{A}) = p_{Y,j} - \frac{B}{A}(p_{X,j}). \tag{2.20}$$

The Z intersection points with the plane $X = 0$ can also be calculated as

$$Z_j(-\frac{p_{X,j}}{A}) = p_{Z,j} - \frac{C}{A}(p_{X,j}). \tag{2.21}$$

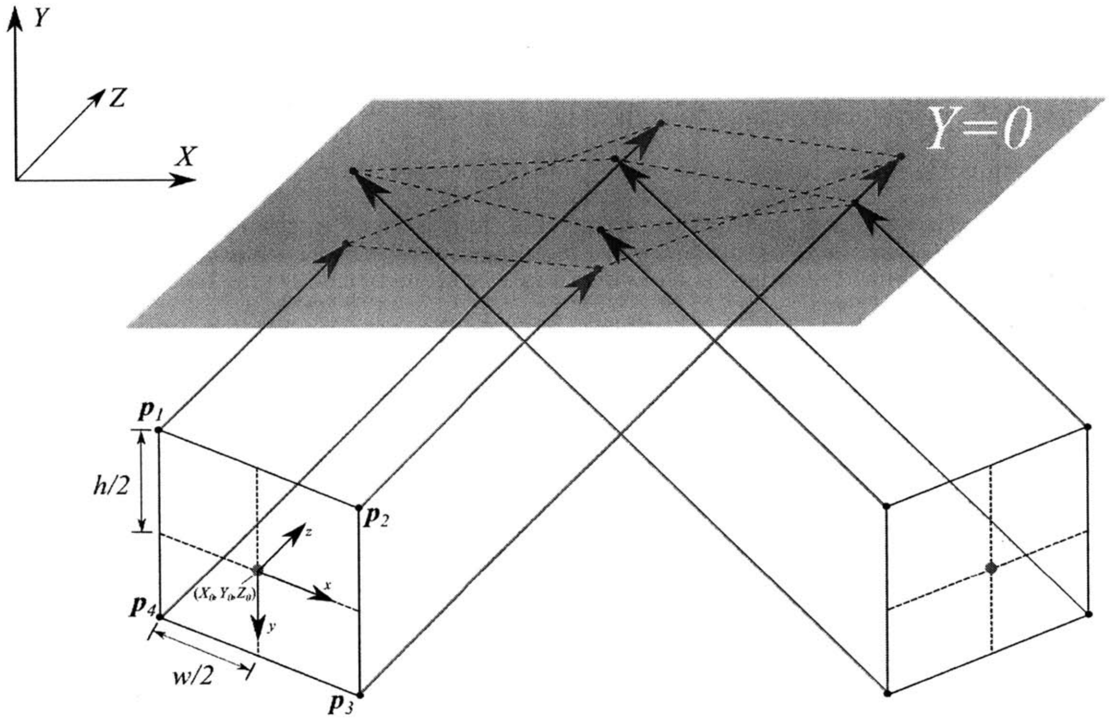

Figure 2-6: Schematic of camera rays defining focal extrema. Rays emanating from the camera image projection corner boundaries (measured in physical units) intersect the plane $Y = 0$. The extreme values of the intersection coordinates in the X and Z dimensions define the focal bounds in each of these directions, respectively. The Y focal extrema can be found by calculating the intersection points of camera rays with the plane $X = 0$.

This process can be carried out for the corner points of each camera being used to calculate the field of view and depth of field. The overall 3D bounds in all dimensions are calculated as the extrema of all of the intersections of the four camera corner vectors with the planes $X = 0$ and $Y = 0$, respectively. The boundaries calculated using this method are upper bounds on the focal extrema. In practice, complete 3D reconstructions may still be attained by processing a volume with smaller bounds than those calculated here, depending on where the particles are located in 3D space relative to the estimated physical focal bounds.

2.3.4 Sources of Error

Error may be introduced during the four main stages of the SAFE process: calibration, image acquisition, raw image processing, and focal stack post-processing. Bajpayee [3] describes two types of calibration error. The first is error in the alignment of the calibration coordinate system to the coordinate system of the scene being imaged. Scaling, rotation, and translation errors are included in this type of error. The second type of calibration error is the error in the relative pose of the array cameras with respect to each other and the origin.

Error may also be introduced during image acquisition and processing as a result of the experimental setup. Recorded features that are out of focus in the raw images will not be reconstructed correctly. A camera array with small baseline spacing between sensors will result in decreased depth resolution during refocusing [8]. Although it is not necessary for objects to be visible in all array camera images at each time step, features are more likely to be localized correctly if they can be found in most of the camera images. Noise in the images or low contrast between the features and the image background may lead to incorrect raw image processing. Missing or inaccurate feature detections will result in erroneous scene reconstruction during post-processing of the focal stack, when found clusters are analyzed. Finally, improper thresholding of the clusters may lead to incorrect object centroid and size measurements.

2.3.5 Limitations

The Synthetic Aperture Feature Extraction method defined above does not enable the reconstruction of arbitrary 3D shapes. Figure 2-7 provides an overview of the limitations on the types of objects that can be reconstructed. Features must be detectable in at least some of the raw camera images. In general, only spherical (or approximately spherical) objects can be reconstructed. The symmetry in the reconstruction of spheres is critical to the current implementation of the SAFE method. This is why the average centroid values may be accurately used when searching for blobs in the focal stack. The knowledge that the reconstructed circles at successive

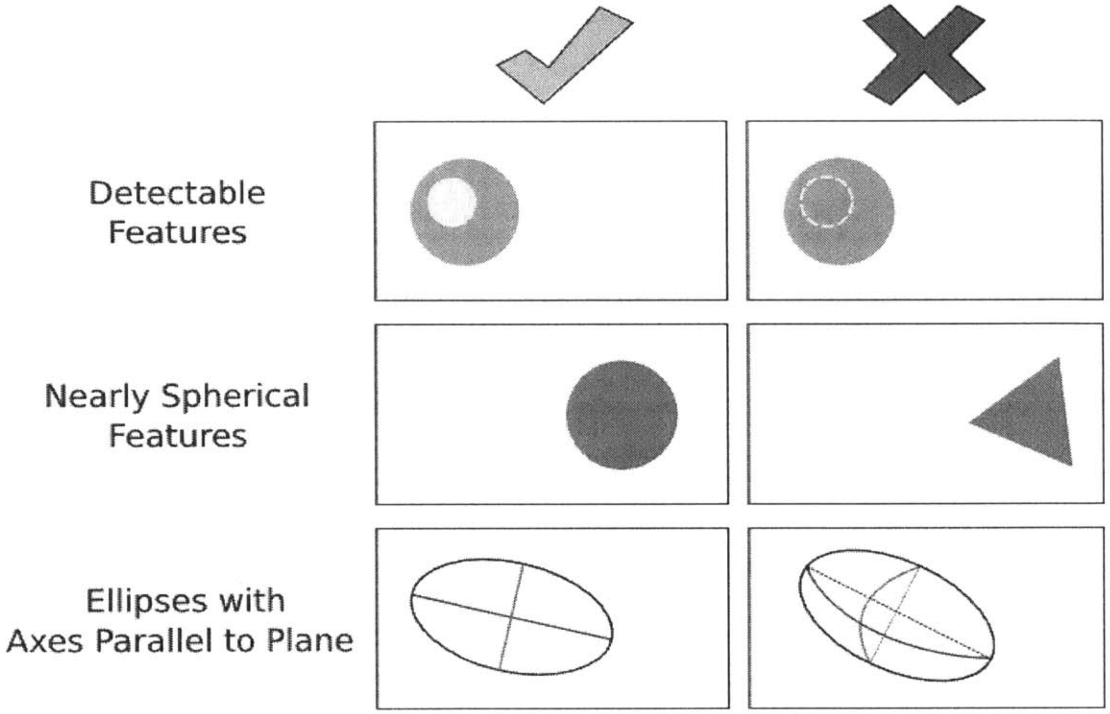

Figure 2-7: Limitations of SAFE technique. The left column displays requirements of feature appearance in raw camera images, while the right column shows unacceptable cases. In order to a SAFE reconstruction to be accurate, image features must be detectable. They also must be nearly spherical, except for the special case in which the objects being detected are elliptical with axes parallel to the image plane.

depths for a particular blobs grow and shrink, respectively, symmetrically around the central depth plane enables the radius of the blob at this depth to be taken as the radius of the spherical blob. The SAFE method may be used to reconstruct ellipsoids in a scene if it is known that their major and minor axes all lie in planes parallel to the imaging plane. If this is the case, then the reconstructed ellipses will grow as the central depth plane of the blob is approached. Then, the major and minor axes may be measured from the central depth plane. Although such reconstruction is possible, it is unlikely that this situation would occur naturally.

2.4 SAFE Simulations

2.4.1 Dark Field Imaging SAFE Simulation

The free Blender 3D modeling software package [18] is used to simulate scenes as well as the cameras, lights, and calibration grids to test the Synthetic Aperture Feature Extraction method. Both dark field and light field imaging simulations have been created by Scharfman and Techet to validate this technique [58, 59, 60]. It has been shown that these two methods produced similar results, as long as the objects in the scene can be detected in the raw camera images in each case.

The simulations performed by Scharfman et al. [61] serve as an example to illustrate application of the SAFE technique to a dark field imaging setup. These simulations extend the work of Bajpayee [3] on the application of SA imaging to Particle Tracking Velocimetry (PTV). In this simulation, three spheres with varying radii are placed at different points in 3D space. These rendered spheres are shown in the top image in Figure 2-10. The colors of the spheres are only used as a visual aid for comparison with the plot at the bottom of Figure 2-10, which shows the same spheres reconstructed using SAFE. Table 2.1 lists the geometric input parameters of this simulation. To model a dark field imaging experiment, a black sheet is placed in front of the camera array, but behind the scene being recorded. Lights are situated around the scene, so that no light directly enters the cameras, but is rather reflected

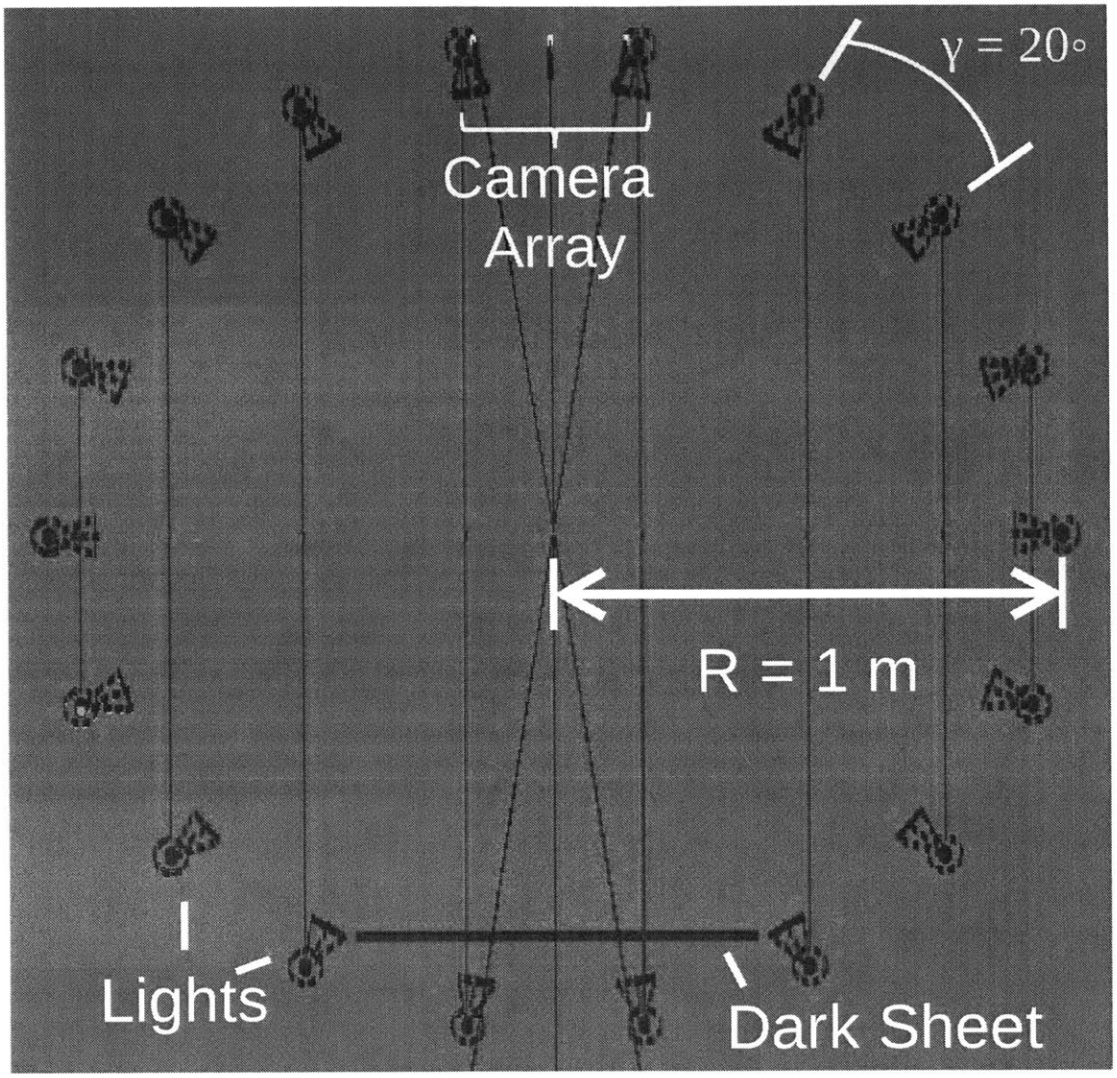

Figure 2-8: Dark field imaging Blender three sphere simulation setup schematic (top view). Lights surround the scene in a circle of radius 1 m. A dark sheet is positioned across from the camera array for the dark field imaging technique.

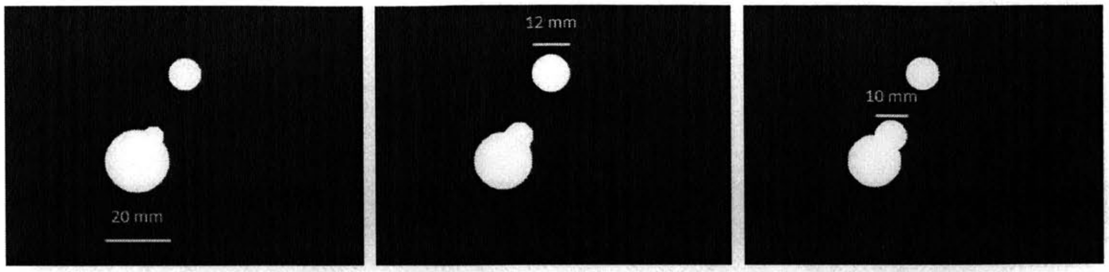

z = -10 mm z = -3 mm z = 3 mm

Figure 2-9: Refocused depth slices for the three sphere rendering shown in Figure 2-10. At each depth shown, a different sphere's center is in focus. Scale bars indicate the diameter of the in-focus sphere center at each depth. The circle corresponding to the in-focus sphere center has a larger diameter at the central plane of focus than at any other plane.

into the cameras by the objects in the scene (Figure 2-8). The black sheet's centroid is located at the center of the $X - Y$ plane and at a depth of 800 mm. It is square with each side measuring 800 mm and has a thickness of 2 mm all symmetric about its center. Columns of lights 400 mm high with a vertical spacing of 20 mm between lights surround the scene, dark sheet, and the array and are located at a radius of 1 m from the world center and are separated by an angle of 20 degrees. These lights, which are known as lamp objects in Blender, were created such that the light's intensity linearly attenuates to half of its original value at a distance of 2 m from the light's position. Light energy is set at 2000 and environment lighting is turned off except during calibration, when only environment lighting is used and the lamps are removed.

Sphere Index	X_{true}	Y_{true}	Z_{true}	r_{true}
1	0	-20	-3	6
2	-15	8	-10	10
3	-10	0	3	5

Table 2.1: Dark field simulation input geometric parameters (measured in mm).

Following the first step of Algorithm 1 for the SAFE LFI approach, raw camera images must first be binarized before refocusing. This task is simplified by using a dark field imaging setup since the raw images are essentially already binary. Minor thresholding may still be necessary to produce completely binary images. Multiplicative refocusing (Eq. 2.3) is utilized with an exponent of 1/9. However, since the images are binarized, the exponent value is arbitrary.

Z_{min} [mm]	-20
Z_{max} [mm]	20
dZ [mm]	1.0
Refocusing Threshold	0

Table 2.2: Dark field imaging SAFE simulation processing parameters.

Sphere Index	**d_X^j [mm]**	**d_Y^j [mm]**	**d_Z^j [mm]**	**d_r^j [mm]**	**d_r^j/r^j [%]**
1	-0.019	0.245	0	0.135	2.252
2	0.071	0.311	0	0.210	2.105
3	-0.046	0.467	0	0.221	4.427

Table 2.3: Dark field simulation SAFE centroid and radii error (as defined in Eq. 2.22) as well as radii percent error.

Figure 2-9 presents three refocused depth slices for the three spheres from Figure 2-10. At each depth shown, a different sphere's center is in focus. Scale bars indicate the diameter of the in-focus sphere center at each depth. The circle corresponding to the in-focus sphere center has a larger diameter at the central plane of focus than at any other plane. In this case, the exact Z center can be found simply because all Z centroid coordinates of these spheres are values that are included in the interval of Z depth slices being processed. For objects located at arbitrary depths, error can be introduced if the particles are not located at a multiple of dZ from the starting Z_{min} plane. Table 2.2 lists the processing parameters for this simulation. Since Z_{min} is an integer value and dZ is 1.0 mm, all three sphere Z centroids plane depth slices will be included in the focal stack and can be located exactly in Z.

The bottom-left two spheres in Figure 2-9 (which are the green and red spheres on the right in both images in Figure 2-10), overlap in the refocused image. The centers and radii of these circles are found by calculating the radius of curvature from three

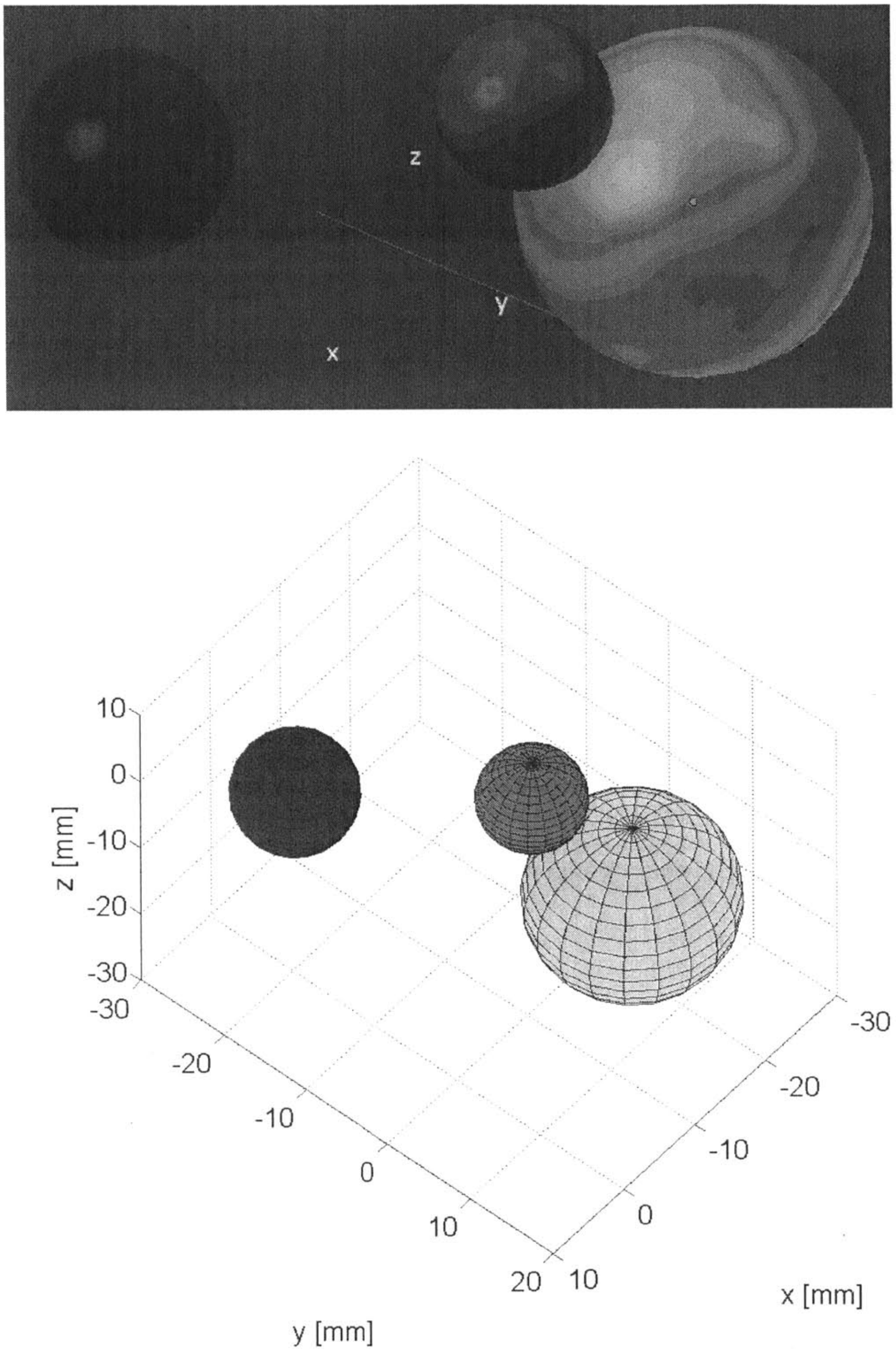

Figure 2-10: (Top) Three sphere Blender dark field imaging simulation. (Bottom) Sphere reconstruction using SAFE method. Matching sphere colors indicate correspondence between the original simulation and the 3D reconstruction result plot.

points on each circle's circumference. This can be done as long as the circles do not completely overlap when their faces are close enough together in the depth direction. Two circles that are far enough apart in Z such that their blur depth extents do not overlap can be distinguished even if they completely overlap in $X - Y$ planes.

To study the accuracy of sphere localization and radius measurement in 3D space, the dimension error, d_i^j, and average dimension error, ϵ_i, are defined as

$$\begin{aligned} d_i^j &= \hat{x}_i^j - x_i^j \\ \epsilon_i &= \frac{1}{N}\sum_{j=1}^{N} |d_i^j|, \end{aligned} \tag{2.22}$$

where $\hat{x}_i^j$ is the i dimension (X, Y, or Z coordinate or the radius, r) of the j^{th} reconstructed sphere, x_i^j is the i dimension of the j^{th} simulated sphere and N is the number of spheres. Table 2.3 presents the error in the calculation of these quantities based on the refocused image volume of the spheres. All coordinate measurements in each dimension have an absolute error below 0.5 mm. The Z coordinates of the spheres were measured exactly by determining the plane containing the largest diameter circle corresponding to a particular sphere, as mentioned above. As expected based on the single sphere simulations, the percent error in radius measurement decreases with increasing sphere radius. The maximum error in any of the radii measurements is less than 4.5%, indicating relatively good agreement between the simulated and measured scene properties. This simulation demonstrates the ability to locate spheres and measure their radii at positions other than the origin, even in the presence of occlusions. Scharfman and Techet [59] have shown that similar results can be attained using a generally more cost effective light field imaging setup (since a light source must only be located behind, rather than surrounding, the scene) as long as the features can be detected and binarized in the raw camera images.

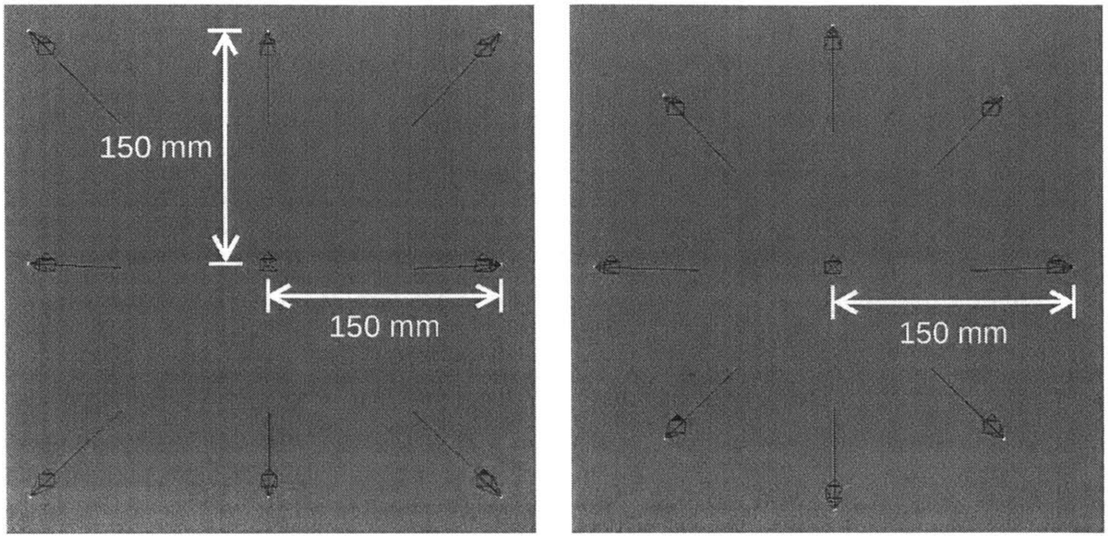

Figure 2-11: (Left) Simulated rectangular camera array orientation schematic (viewed from behind the array looking in the same direction as the center camera). (Right) Circular camera array viewed from the same angle as the rectangular array. All cameras are located at a depth of Z = -1 m relative to the center of the simulated world at the origin.

2.4.2 Camera Array Configurations

Two different camera array configurations were used in Blender simulations (see Figure 2-11) to assess the effect of array shape on reconstruction error [61]. The coordinates of all nine cameras in both of the arrays are planar. In the left array in Figure 2-11, the cameras are arranged in a square grid with X and Y spacing of 150 mm between cameras. The circular configuration on the right in the same figure features a central camera surrounded by eight other cameras at a radius of 150 mm, each separated by 45 degrees. All cameras in both configurations are oriented toward the center of the simulated world, which is located at the origin at a Z distance of 1 m from the center camera (which has the same coordinates and orientation in both arrays).

To test the dark field imaging SA method and compare the accuracy of the results from the two array configurations, single spheres were plotted at the origin in Blender with radii varying from 4 to 40 mm in increments of 4 mm. These spheres are illu-

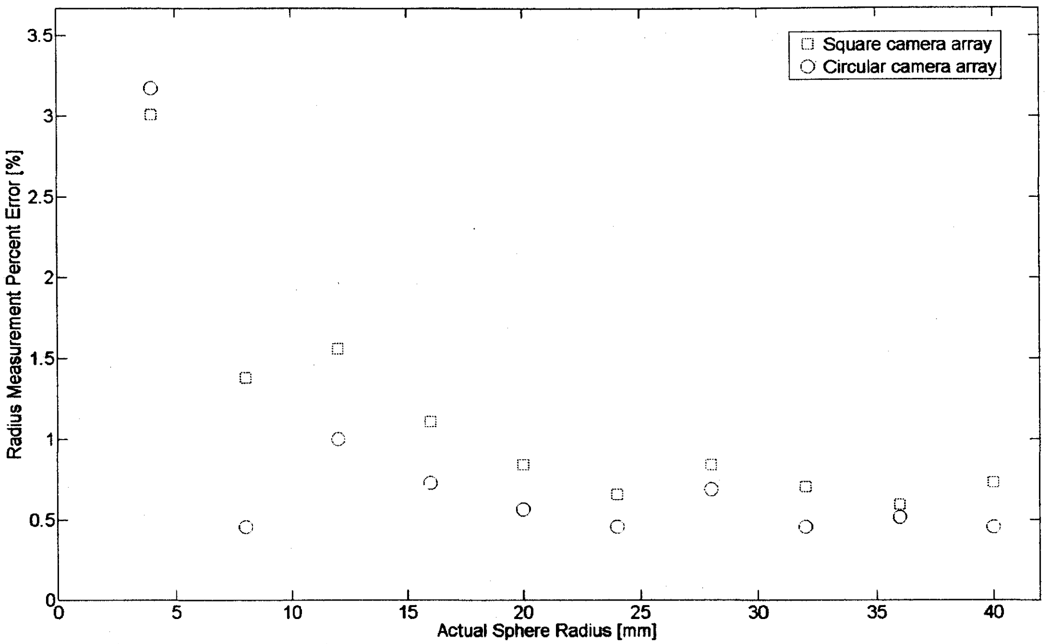

Figure 2-12: Single sphere error for both the square and circular, respectively, camera arrays shown in Figure 2-11. For each measurement, a single sphere is located at the origin of the simulated world with a radius in the range of 4 to 40 mm in increments of 4 mm.

minated using the surround lighting shown in Figure 2-8 with a black sheet blocking the light across from the cameras. The refocused Z depth slice containing the circle of greatest diameter is found, indicating that the center of the sphere is located there. Then the radius is measured using image analysis functions from MATLAB's Image Processing Toolbox. No threshold is applied to the refocused images used for the radii calculations. All of the spheres are found correctly found to be located precisely at the origin in the Z dimension and very close to the origin in the X and Y dimensions.

Figure 2-12 presents the percent error in the calculation of the spheres' radii using both the square and circular camera arrays. As expected, the error decreases with increasing radius since differences in pixel measurement for the radius become smaller relative to the actual radius value as the sphere radius increases. Due to the small size of the 4 mm sphere, small errors in radius measurement have a larger impact on the error. In all cases except for the 4 mm sphere, the circular array outperforms the square one. This should generally be the case because the relative orientation of the cameras for the circular array results in a more natural blur pattern. In the case of the square array, it is observed that the reconstructed sphere appears more angular in the refocused Z depth slices due to the angles and orientations of the cameras in this array. The slices of the sphere look more circular, as they should, for the circular camera array configuration. All percent errors are below 3.5%, with most being below 2%. All of the percent errors for the circular array measurements other than the 4 mm sphere are below 1%. This indicates relatively good agreement between the simulated and measured sphere radii.

2.4.3 Light Field Imaging SAFE Simulation

Light Field Imaging SAFE simulations are used to test the performance of the SAFE method as a function of optical density. This is achieved by simulating opaque spheres in a constant volume with a successively increasing occupied volume fraction. As in the previously mentioned dark field simulation, sphere centroids and radii are calculated by reconstructing the scene using the SAFE technique. Table 2.4 lists the geometric parameters used in each of the six simulation trials. Spheres are simulated such that their centroids and radii are of random values within the specified bounds. In addition, a minimum inter-sphere distance of 0.5 mm is enforced.

X Bounds	$[-100, 100]$
Y Bounds	$[-100, 100]$
Z Bounds	$[-100, 100]$
r Bounds	$[1.5, 4.0]$
Min Inter-sphere Distance	0.5

Table 2.4: LFI SAFE simulation input geometric parameters (measured in mm).

In the processing of these simulation data, calibration, image acquisition, and raw image processing errors are eliminated. Therefore, the only error is due to post-processing of the focal stack and found clusters. The camera calibration P matrices are extracted directly from the Blender simulation (no calibration is performed using

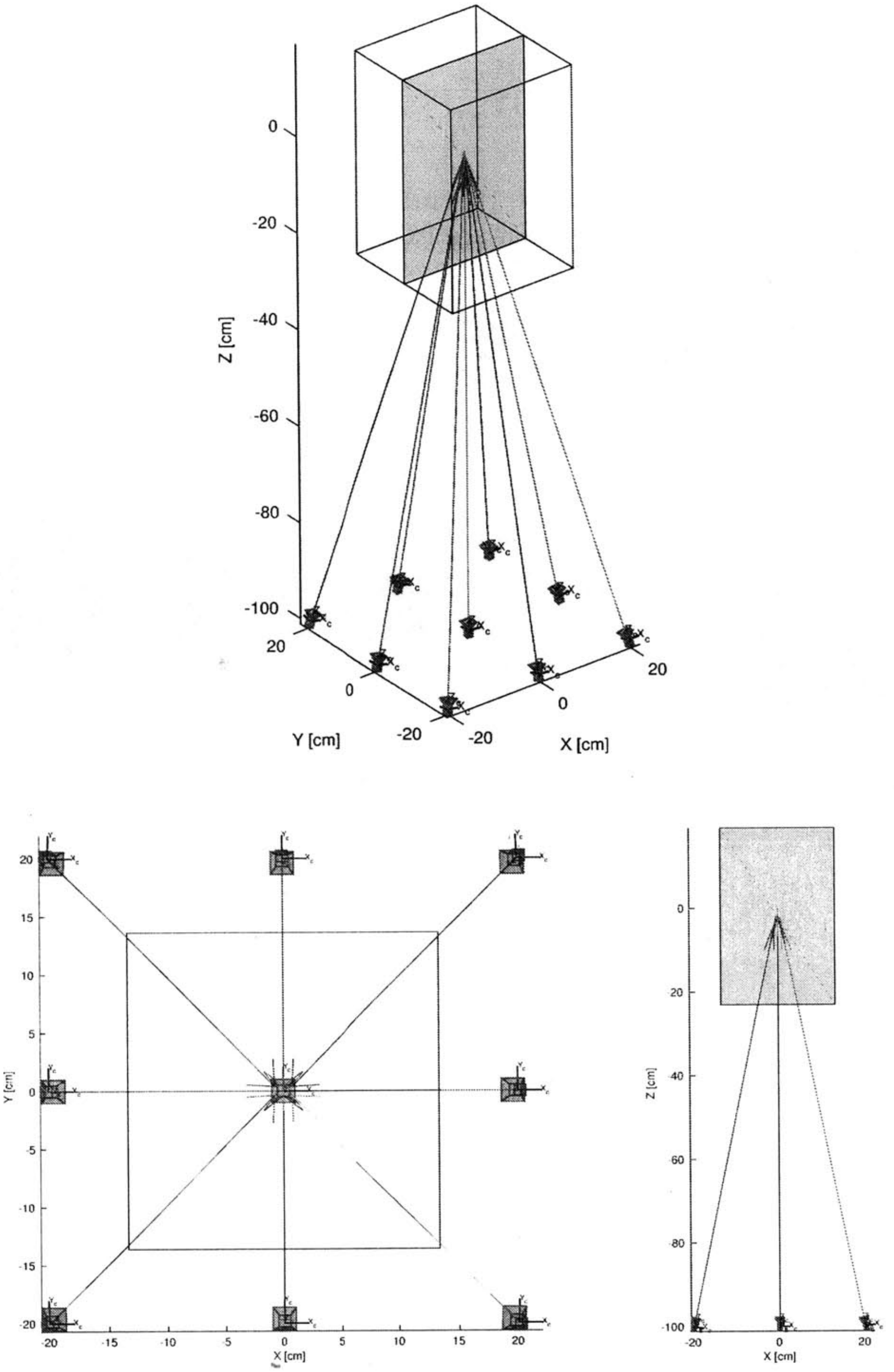

Figure 2-13: Camera locations, orientations, and focal bounds (indicated by the blue bounding box) used in the simulations of spheres with increasing volume fraction. The plane $Y = 0$ (shown in pink) is used along with the plane $X = 0$ to calculate the focal bounds (see section 2.3.3). Clockwise from top: isometric, $X - Z$, and $X - Y$ views, respectively.

DOF	42.26
FOV_{hor}	26.71
FOV_{vert}	27.24

Table 2.5: Camera array focal bounds (in cm) in all sphere simulations of increasing volume fraction. These focal extrema are calculated using the formulas in section 2.3.3.

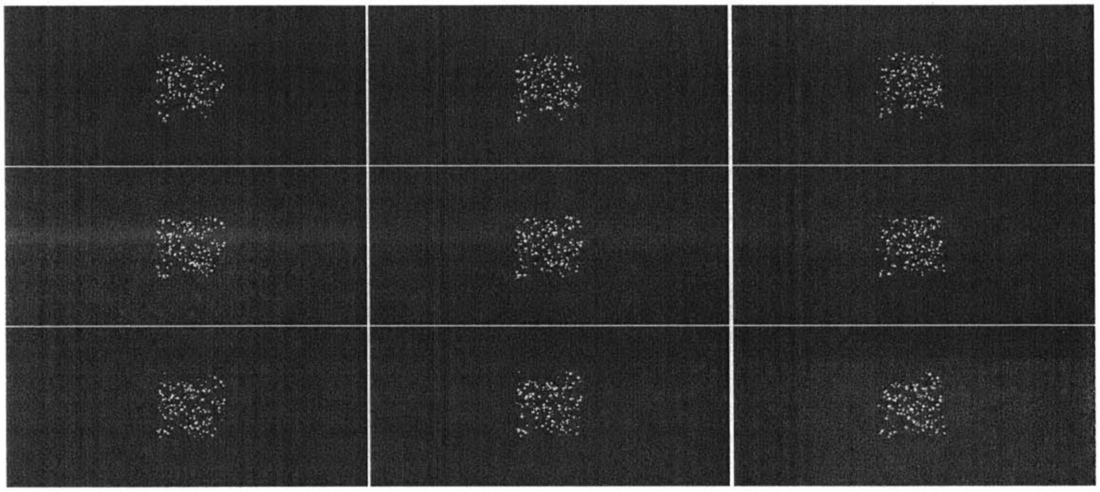

Figure 2-14: Raw rendered camera array images in trial 6 simulation. Each image has a resolution of 1292 x 581 pix, with each mm corresponding to 4.84 pix. 160 spheres are shown in each image.

simulated images of a calibration grid). Figure 2-13 displays the camera positions and orientations that are set in these simulations. Nine cameras are arranged in a square grid with a spacing of 20 cm in both the X and Y directions. All cameras are located at Z = -1 m and are all oriented at the origin of the world coordinate frame. The focal bounds in the X, Y, and Z dimensions are indicated by the blue bounding box. The depth of field (DOF) in the Z direction and the horizontal and vertical field of view (FOV) in X and Y, respectively, are listed in Table 2.5. These focal bounds are calculated as described in section 2.3.3.

Raw images from each of the cameras, which are shown for simulation trial 6 in Figure 2-14, are all recorded in focus. The scene is fully contained within the volume of interest in all directions. Circles in the raw images are found simply via thresholding since the background is black, and the features of interest are gray. There

Z_{min} [mm]	-110
Z_{max} [mm]	130
dZ [mm]	0.5
Refocusing Threshold	120
Cluster Voxel Count Threshold	10

Table 2.6: LFI SAFE simulation processing parameters for all six trials. The refocusing threshold of 120 is selected from the range [0, 255] to reduce the 3D reconstruction error.

is no error in the feature detection process. After the features are thresholded, only the boundaries are retained, as this simplifies cluster extraction. The overlapping blur patterns are not as optically dense when only boundaries are kept in the raw images.

The raw images from each camera are transformed based on the P matrices and are then refocused using the additive approach (Eq. 2.2) with thresholding. Table 2.6 lists the parameters used during refocusing and in post-processing the focal stack. The refocused Z range is within the overall depth of field. A dZ depth increment 1/3 of the lower bound sphere radius is used. Figure 2-15 shows four slices of the resulting focal stack at different Z depths. Spheres that are actually located at each respective depth are shown in sharp focus, while the other spheres are seen as blur artifacts. While progressing through the focal stack in the Z direction, the blur pattern from each of the nine cameras can be observed converging as the sphere center is approached and then diverging. The blur patterns also move radially outward from the Z axis with increasing Z and inward with increasing Z. This is likely caused by the relatively low camera focal length, f, of 35 mm of the cameras in this simulation. Figure 2-16 shows the effect of thresholding slices of the focal stack. All images shown are at the same Z slice. As the threshold is increased, blur artifacts are removed, leaving only the features that are located at this depth. For all of the six trials, a threshold of 120 is used. The threshold is not increased beyond this value because that would potentially lead to the elimination of correct spheres in the final reconstruction.

Figures 2-17 through 2-22 present the 3D scene reconstruction results for trials 1 to 6. At the top of each figure, the ground truth simulated spheres are plotted. The final

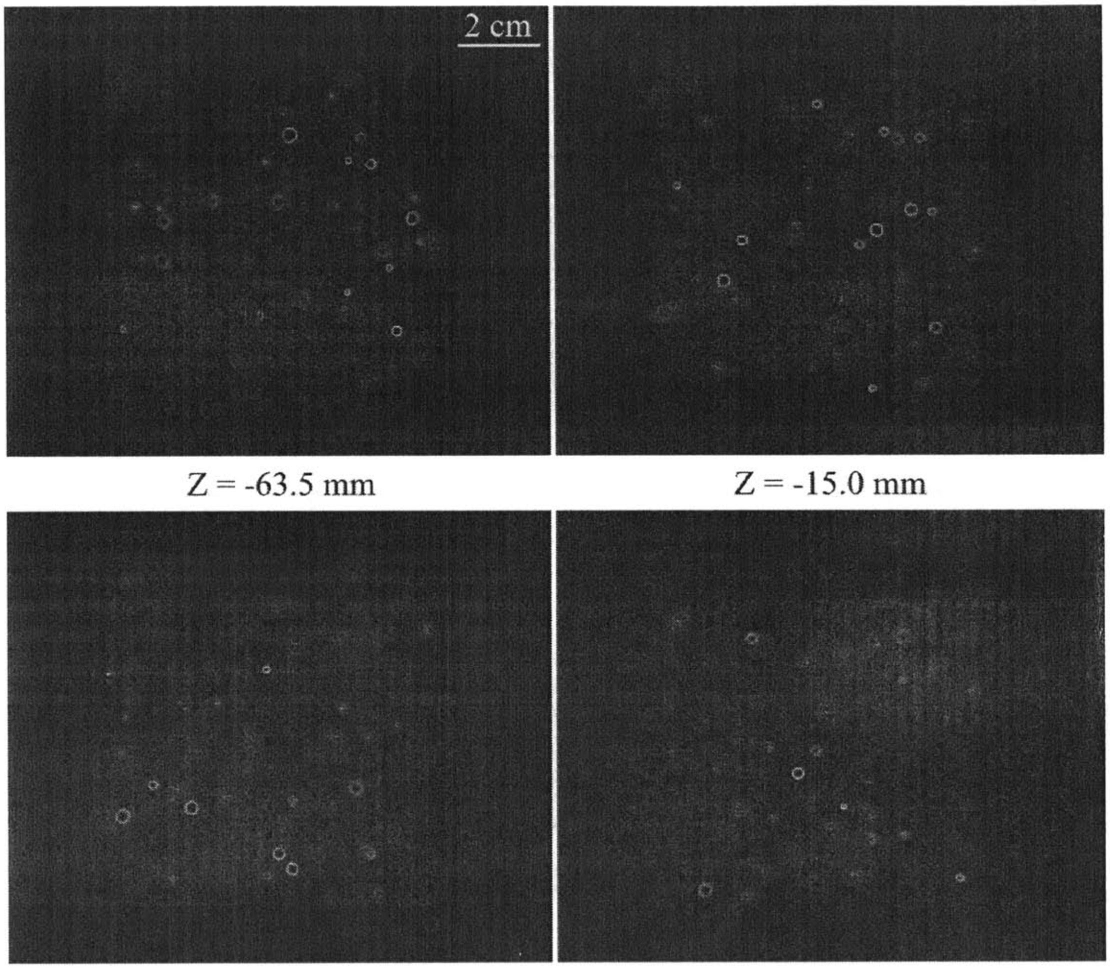

Z = -63.5 mm

Z = -15.0 mm

Z = 1.5 mm

Z = 65.0 mm

Figure 2-15: Trial 6 simulation focal stack depth slices. In these images, no thresholding is applied after refocusing. Spheres that are actually located at each depth appear in focus, while spheres at other depths are seen as blur artifacts.

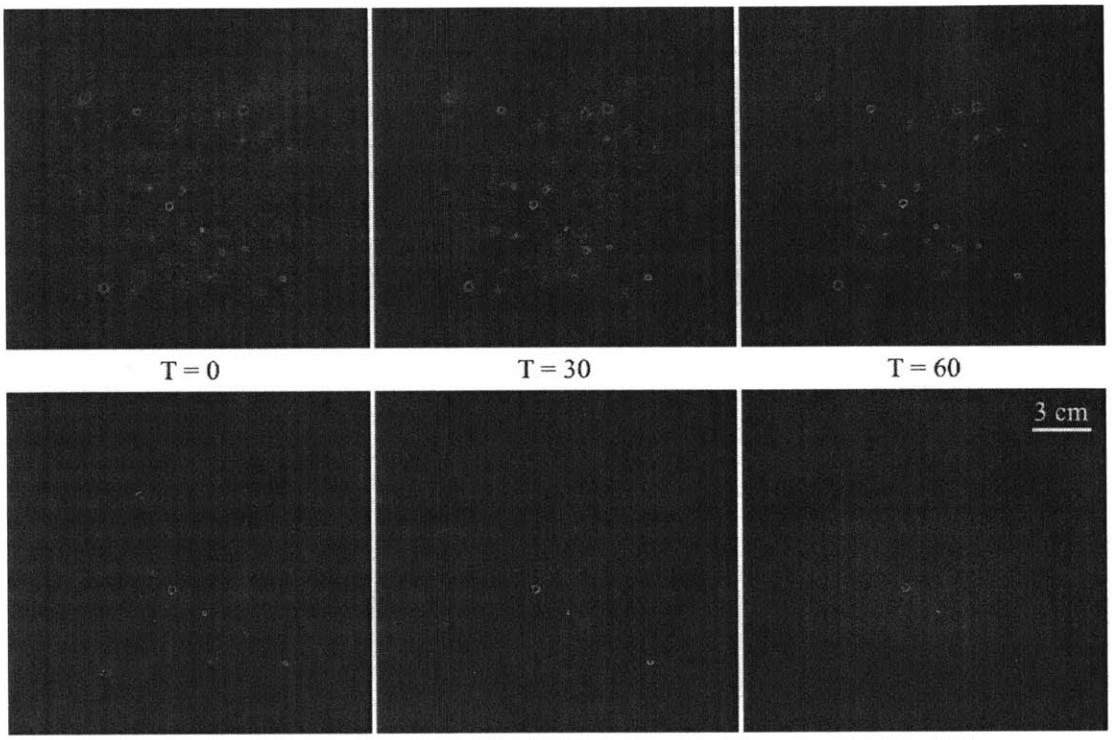

T = 0 T = 30 T = 60

T = 90 T = 120 T = 150

Figure 2-16: Trial 6 simulation focal slice at depth $Z = 65.0$ mm with thresholds ranging from 0 to 150 (out of a possible maximum of 255). Blur artifacts are removed during thresholding, and only in-focus features corresponding to spheres actually located at this depth remain.

reconstructed spheres are shown in the middle plot, and the bottom graph displays the clusters of voxels extracted from the focal stack prior to final thresholding. The final thresholding step is used to remove small clusters that represent noise due to blur artifacts or breaks in the blur pattern near the Z borders of each voxel cluster. These gaps would incorrectly lead to separate small blobs in the final set of clusters. The final reconstructed spheres are observed to generally match the number and centroid values of the simulated spheres. However, the sphere radii tend to be underestimated.

Figures 2-23 through 2-28 present the error in the centroid and radii values as functions of each of these quantities, respectively, for each sphere in all six trials. There is generally greater variance in d^j_Z than for errors in the other dimensions. This may be due to the elongation of objects in Z during refocusing. Greater baseline spacing between array cameras would increase Z resolution. Refocusing using a finer dZ increment is also likely to reduce error in the Z dimension. d^j_r is also smaller in magnitude than the error for X, Y, or Z. The SAFE method as applied here tends to under-estimate the radii of the simulated spheres, as indicated by the generally negative values of $d_r{}^j$ in the last row of error plots in Figures 2-23-2-28. This may be due to thresholding applied to the slices of the focal stack. However, applying a lower threshold could lead to greater error in the final reconstruction.

Table 2.7 provides summary data for each of the trials. The low average errors in X, Y, Z, and r (with a maximum of 1.567 for ϵ_Z in trial 6) indicates good agreement between the simulated and reconstructed scene. Average dimension error for X, Y, Z, and r tends to increase with increasing simulated (ground truth) sphere occupied volume fraction, ϕ_{true}. The simulated and reconstructed number of spheres, N_{true} and N_{rec}, respectively, agree exactly in trials 1-4. The percent error in the number of detected spheres is 2.5% and 5% in trials 5 and 6, respectively. Error generally increases with increasing ϕ_{true} because it becomes more difficult to distinguish individual spheres. For instance, in Figure 2-22 two particles seen at the top-left of the simulated spheres in the top plot appear as one larger particle in the middle plot. These occurrences increase the average centroid and radius error.

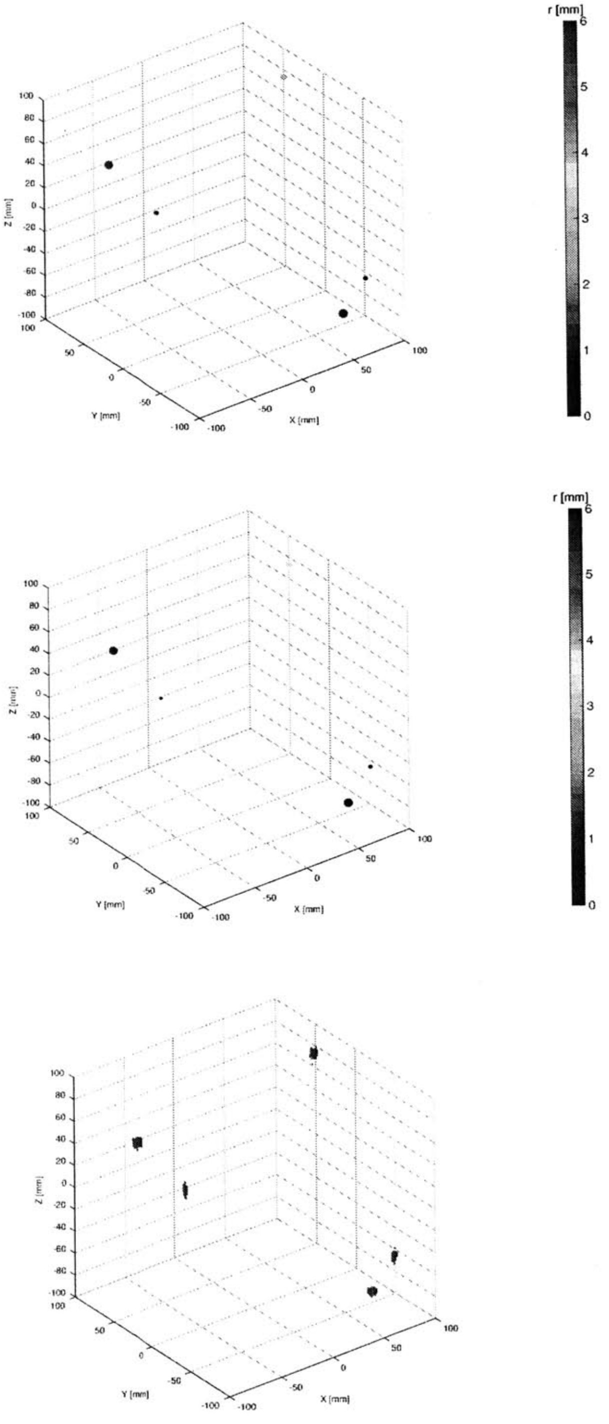

Figure 2-17: Trial 1 simulation of five spheres. (Top) Spheres plotted in simulation volume bounds with ground truth centroids and radii. (Middle) Reconstructed scene using the SAFE method. All five spheres have been reconstructed. (Bottom) Voxels extracted from focal stack prior to final thresholding based on cluster size.

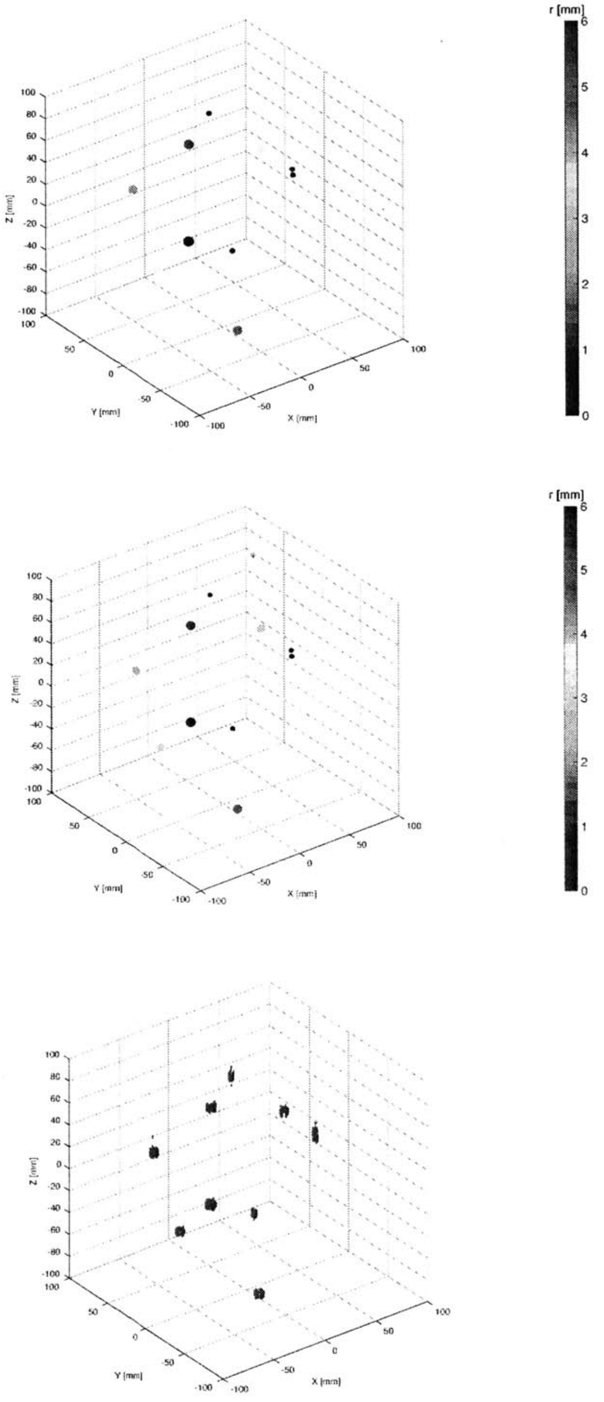

Figure 2-18: Trial 2 simulation of ten spheres. (Top) Spheres plotted in simulation volume bounds with ground truth centroids and radii. (Middle) Reconstructed scene using the SAFE method. All ten spheres have been reconstructed. (Bottom) Voxels extracted from focal stack prior to final thresholding based on cluster size.

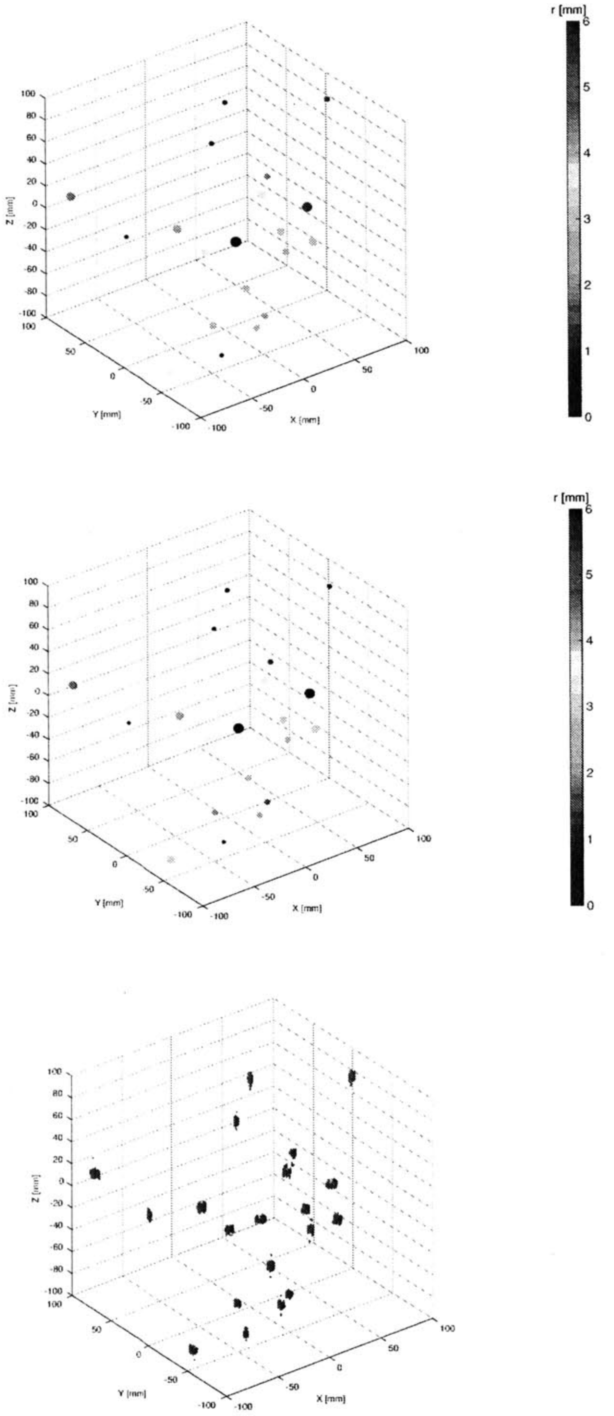

Figure 2-19: Trial 3 simulation of 20 spheres. (Top) Spheres plotted in simulation volume bounds with ground truth centroids and radii. (Middle) Reconstructed scene using the SAFE method. All 20 spheres have been reconstructed. (Bottom) Voxels extracted from focal stack prior to final thresholding based on cluster size.

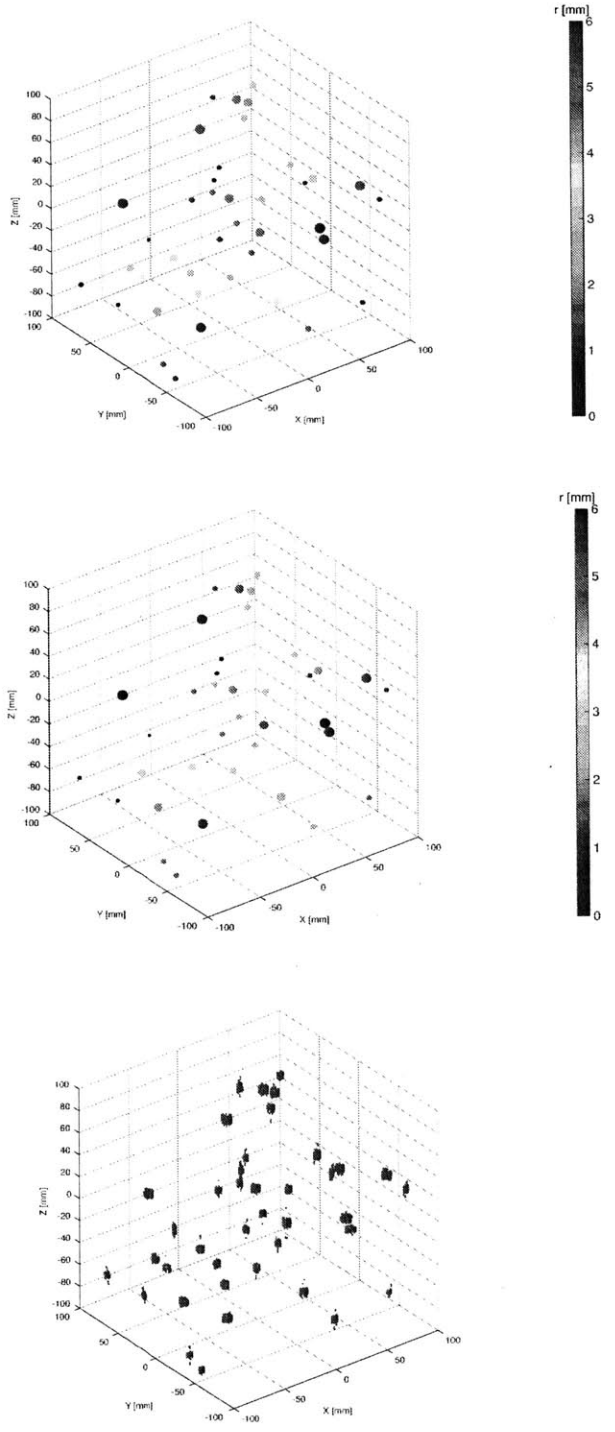

Figure 2-20: Trial 4 simulation of 40 spheres. (Top) Spheres plotted in simulation volume bounds with ground truth centroids and radii. (Middle) Reconstructed scene using the SAFE method. All 40 spheres have been reconstructed. (Bottom) Voxels extracted from focal stack prior to final thresholding based on cluster size.

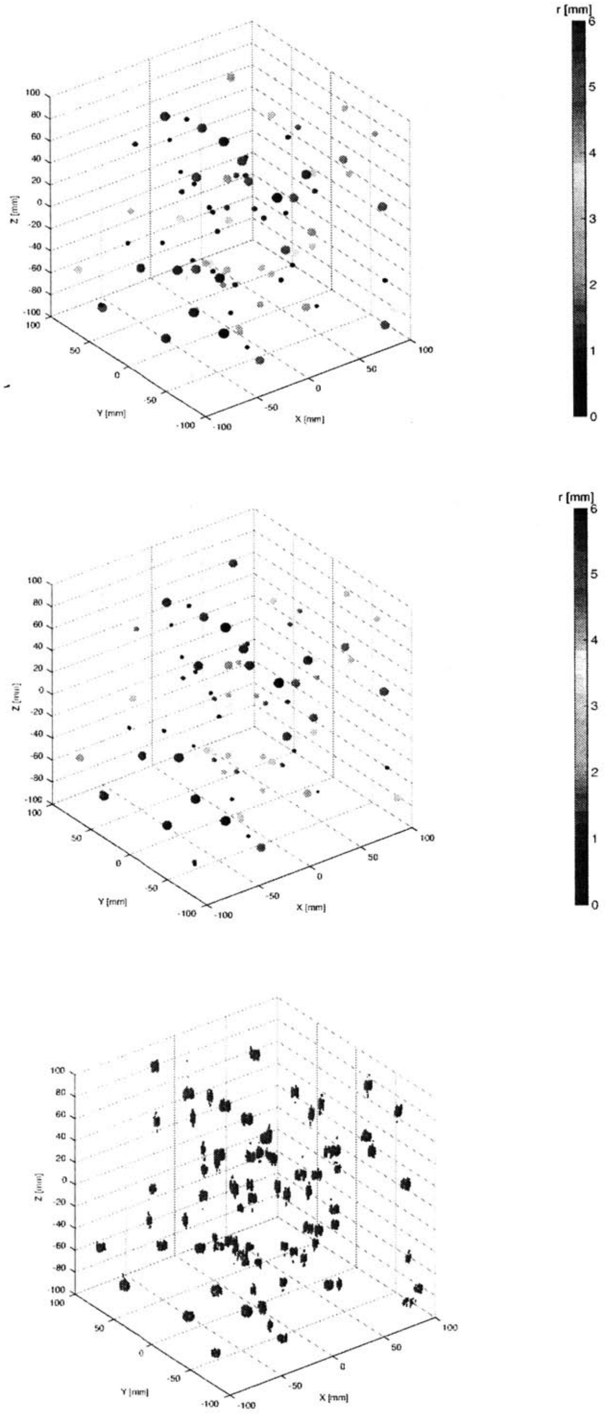

Figure 2-21: Trial 5 simulation of 80 spheres. (Top) Spheres plotted in simulation volume bounds with ground truth centroids and radii. (Middle) Reconstructed scene using the SAFE method. 78 of the 80 spheres have been reconstructed. (Bottom) Voxels extracted from focal stack prior to final thresholding based on cluster size.

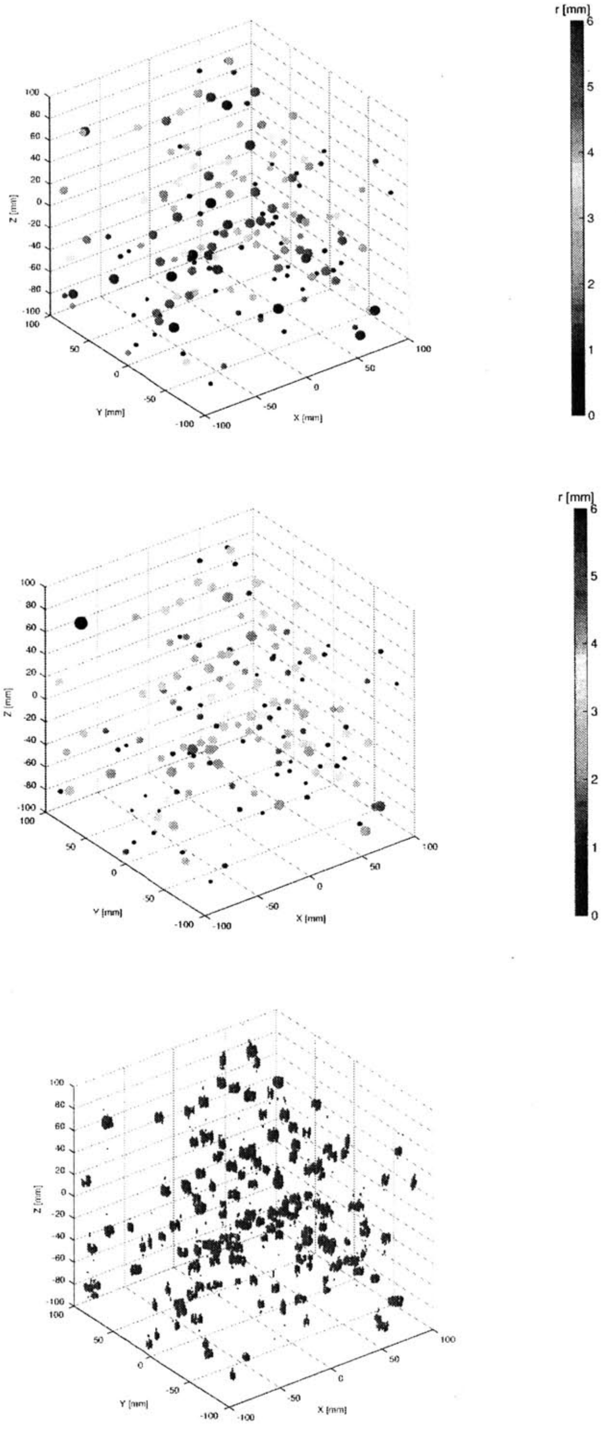

Figure 2-22: Trial 6 simulation of 160 spheres. (Top) Spheres plotted in simulation volume bounds with ground truth centroids and radii. (Middle) Reconstructed scene using the SAFE method. 152 of the 160 spheres have been reconstructed. (Bottom) Voxels extracted from focal stack prior to final thresholding based on cluster size.

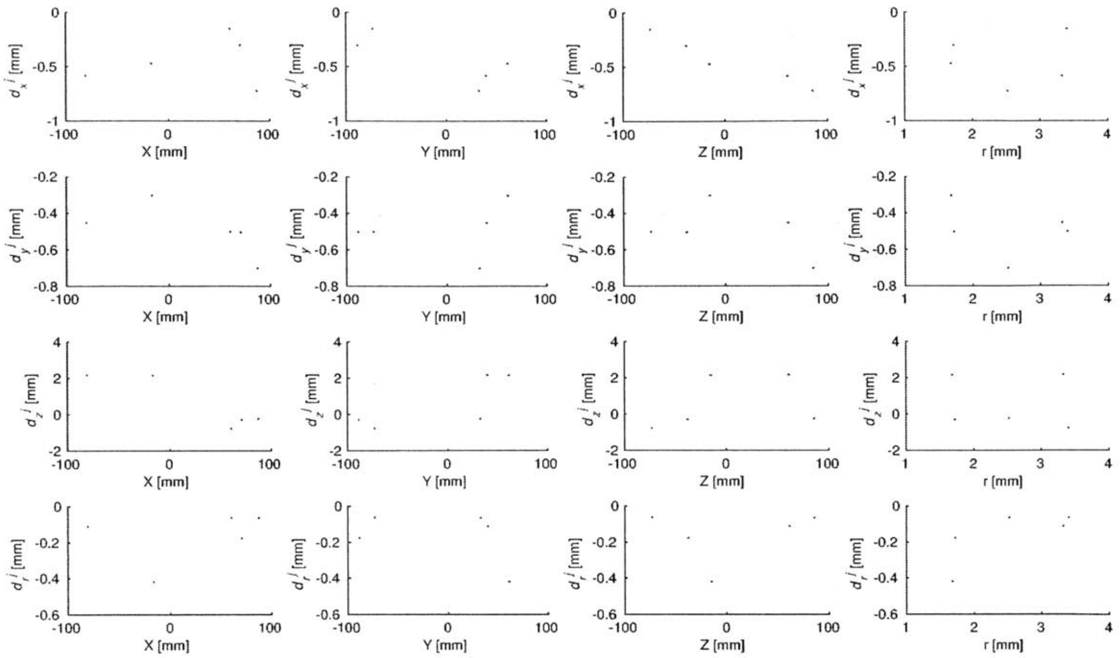

Figure 2-23: Trial 1 simulation localization errors d_i^j of sphere centroids in the X, Y, and Z dimensions and of sphere radius, r.

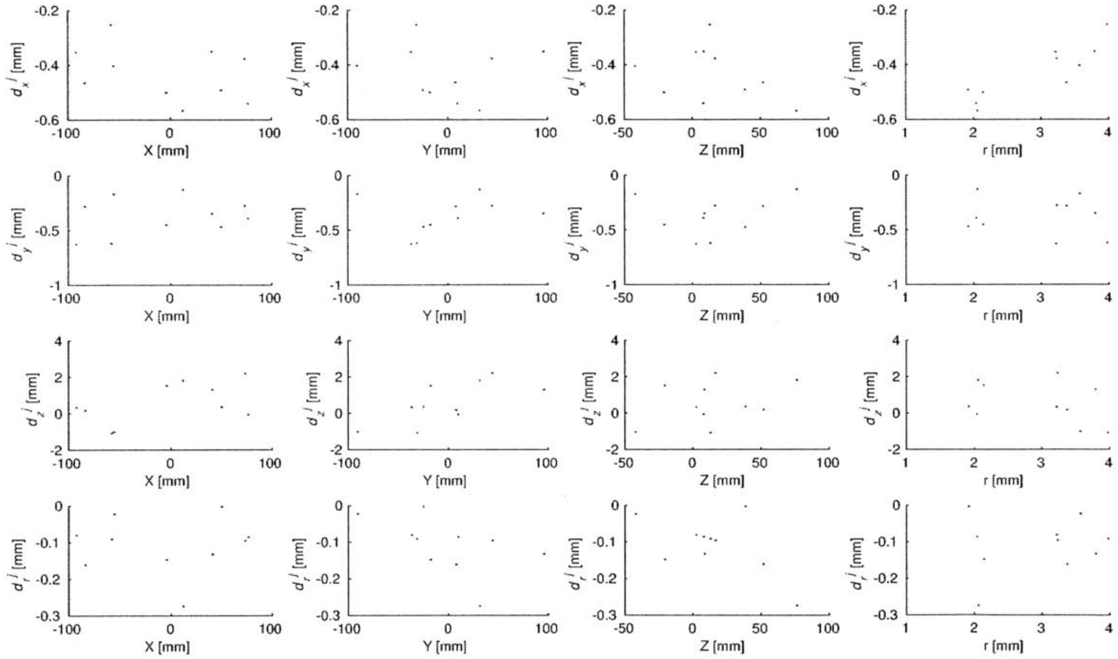

Figure 2-24: Trial 2 simulation localization errors d_i^j of sphere centroids in the X, Y, and Z dimensions and of sphere radius, r.

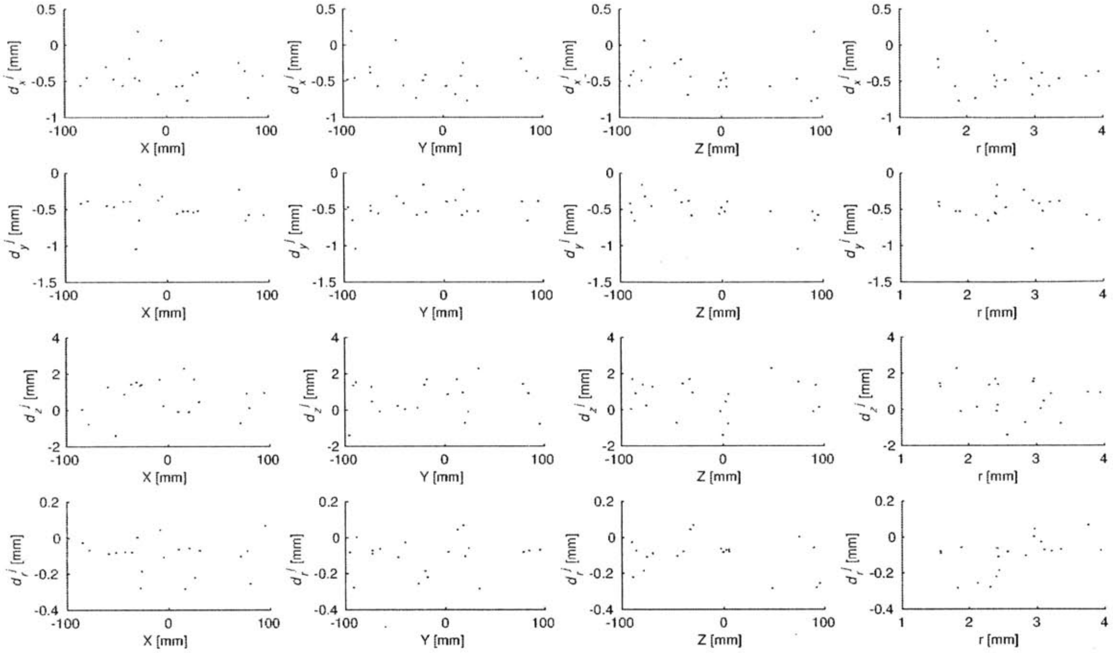

Figure 2-25: Trial 3 simulation localization errors d_i^j of sphere centroids in the X, Y, and Z dimensions and of sphere radius, r.

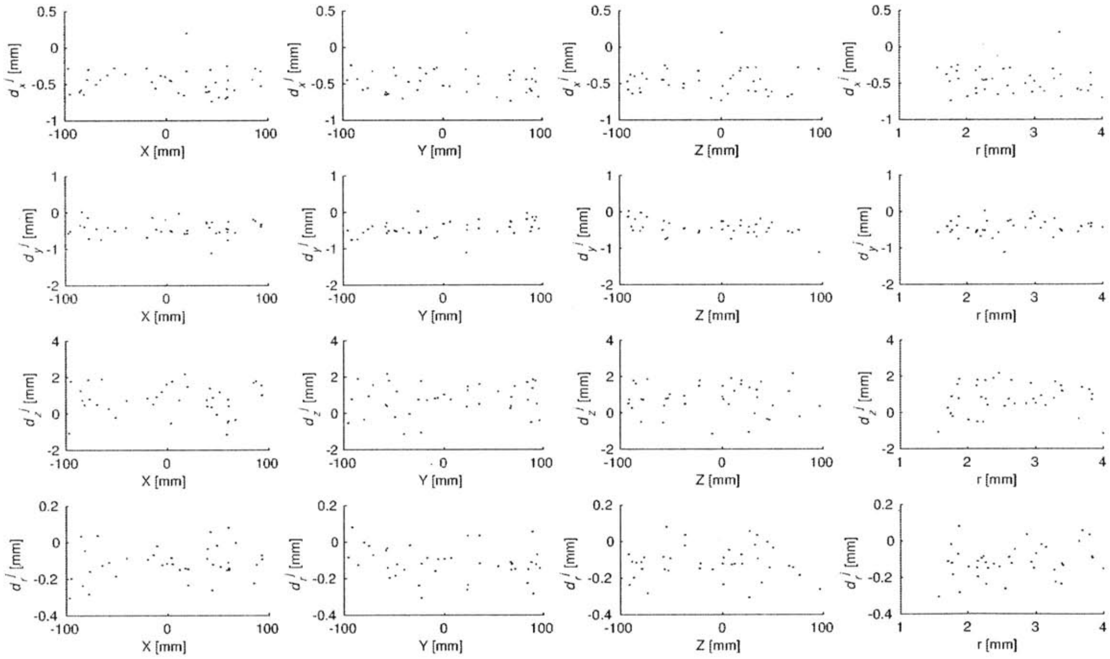

Figure 2-26: Trial 4 simulation localization errors d_i^j of sphere centroids in the X, Y, and Z dimensions and of sphere radius, r.

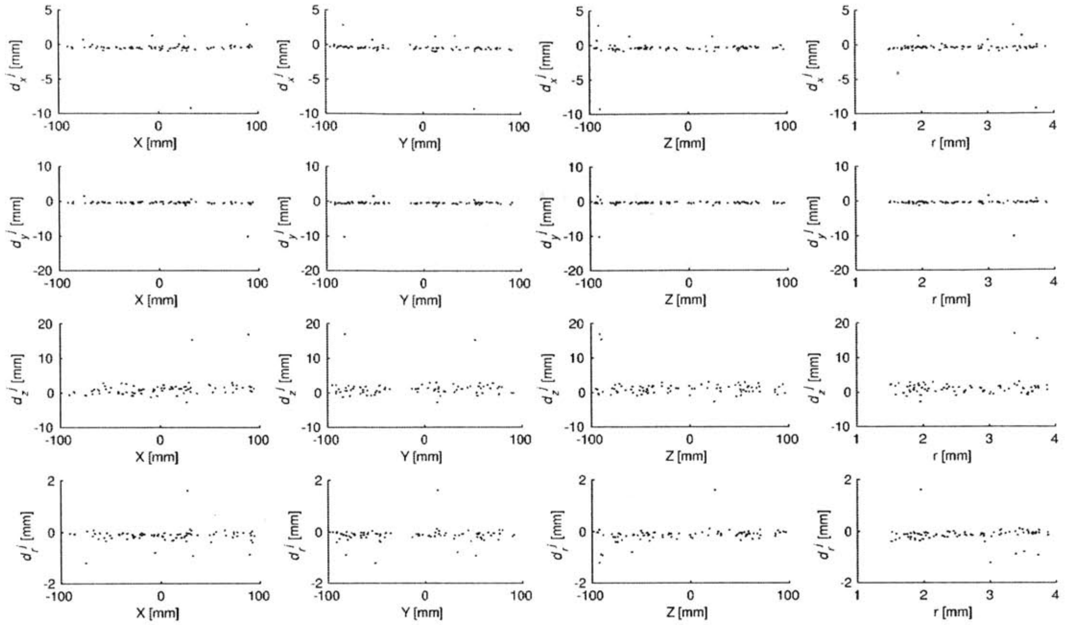

Figure 2-27: Trial 5 simulation localization errors d_i^j of sphere centroids in the X, Y, and Z dimensions and of sphere radius, r.

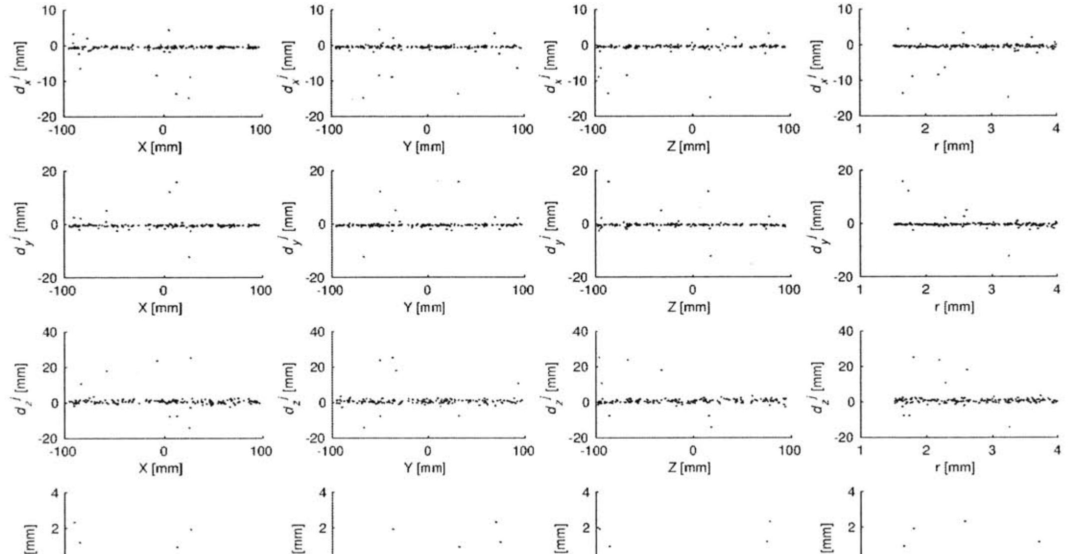

Figure 2-28: Trial 6 simulation localization errors d_i^j of sphere centroids in the X, Y, and Z dimensions and of sphere radius, r.

Trial Index	N_{true}	N_{rec}	ϕ_{true} [%]	ϵ_X [mm]	ϵ_Y [mm]	ϵ_Z [mm]	ϵ_r [mm]	ϵ_r [%]
1	5	5	5.34e-3	0.445	0.493	1.126	0.167	8.577
2	10	10	1.59e-2	0.430	0.377	0.987	0.109	4.124
3	20	20	2.28e-2	0.444	0.490	0.970	0.111	4.800
4	40	40	4.82e-2	0.476	0.437	0.990	0.124	5.220
5	80	78	9.41e-2	0.607	0.581	1.531	0.185	7.794
6	160	152	0.203	0.863	0.817	1.567	0.230	9.495

Table 2.7: LFI SAFE simulation results. N_{true} and N_{rec} are the simulated and reconstructed, respectively, number of spheres in each trial. ϕ_{true} is the volume fraction of the total simulation volume (see Table 2.4) occupied by the simulated spheres. ϵ_X, ϵ_Y, ϵ_Z, and ϵ_r are the average dimension error for the X, Y, and Z sphere centroid coordinates and the sphere radius, r. The last column displays ϵ_r as a percent error of the simulated sphere radii.

2.5 SAFE Bubble Experiments

Here SAFE LFI technique is applied to a soap bubble flow field generated using an Ever Bubble Blaster produced by Imperial. Pulsed lighting is used with an array of nine cameras recording at 30 fps (Figure 2-29), which is a high enough frame rate to minimize streaks due to motion blur in this case. All cameras are Mantas produced by Allied Vision. Each recorded image has a resolution of 1292 by 964 pixels, or 210.5 mm by 157 mm. Bubbles that are approximately spherical in shape are located and measured in 3D using the SAFE method described in Algorithm 1. After 3D centroids are found, velocities and other flow quantities can be calculated by tracking the bubbles over time.

Figure 2-31 shows raw images of the calibration grid recorded by each of the nine cameras used in the present experiments. The calibration target has seven horizontal and five vertical internal grid points, respectively. Each grid square's side length is 5 mm. The layout of the images corresponds to the orientation of the array cameras when looking in the -Z direction (into the camera lenses). Each lens has a focal length of 35 mm and the F-stop is 4.

The top half of Figure 2-30 presents raw camera array images of a bubble flow field at a particular time instant. Circles are detected in these images, and binary

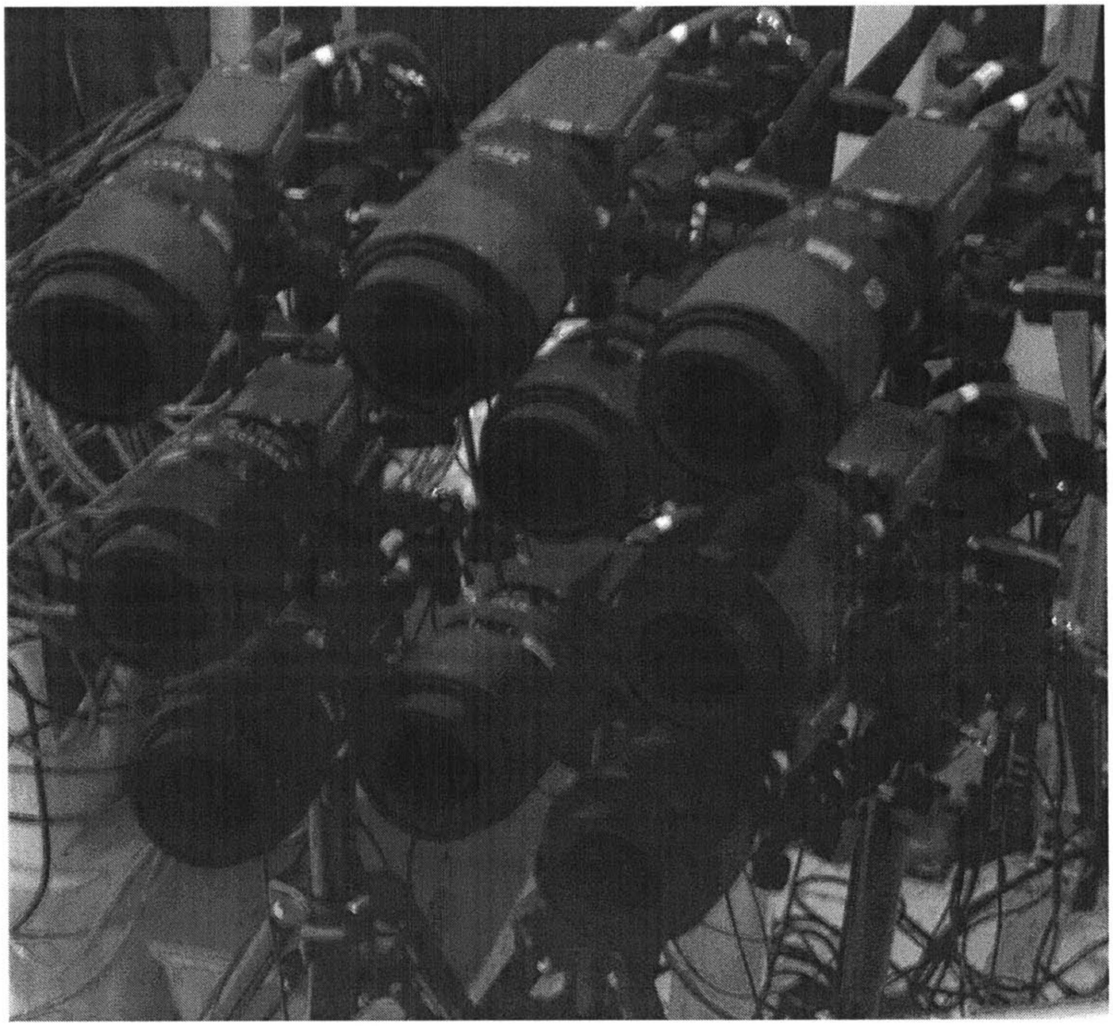

Figure 2-29: Light field imaging array consisting of nine cameras.

images are produced with black backgrounds and white thickened rings corresponding to circle edges (bottom of Figure 2-30).

After finding the circles, new binary images are created with black backgrounds and white thickened rings at the borders of the found circles. The circle borders are thickened so that it is easier to detect the central Z plane of each sphere. (Rings are used rather than filled circles because the latter may sometimes be too large and merge in the resulting 3D volume, making them indistinguishable from each other.) These images are then refocused using multiplicative SA refocusing with an exponent of 1/9 at a depth interval dZ of 0.1 mm (two orders of magnitude below the average bubble radii) within a depth range of 400 mm. Multiplicative refocusing is used here, as in dark field imaging [61], because black pixels in transformed images will cause pixels to assume a value of zero where out-of-focus blur artifacts would otherwise be found. This results in clean refocused image depth slices at the Z centers of the spheres. From these refocused depth slices, the in-focus features can be detected at each plane. Once the Z coordinate sphere centroids are found, the X and Y centroids as well as radii can be extracted at the appropriate depth.

The 3D centroids and radii of each sphere are then detected in the refocused image stack. The 3D plot at the bottom-right of Figure 2-4 presents another example of all of the detected voxels with bounding boxes enclosing discrete blobs in 3D for another particular time step. The 3D final centroids and radii are calculated as the mean centroids and radii, respectively, of such clusters. Centroids are tracked over time using MATLAB software developed by Blair and Dufresne [12].

By calculating and tracking centroids and radii over time, the final scene can be reconstructed, as shown in Figure 2-32. In this Figure, the two spheres shown correspond to two of the bubbles depicted in Figure 2-30. (Only two bubbles are shown from this time step because they are not touching the image borders, were detectable in multiple frames, and were separated by more than the minimum threshold distance used to distinguish discrete bubbles.) Blue curves represent the trajectories of all of the other spheres detected. These are spline fits to the estimated centroids. Red arrows are velocity vectors. Gravity is acting downward (in the -Y direction). The

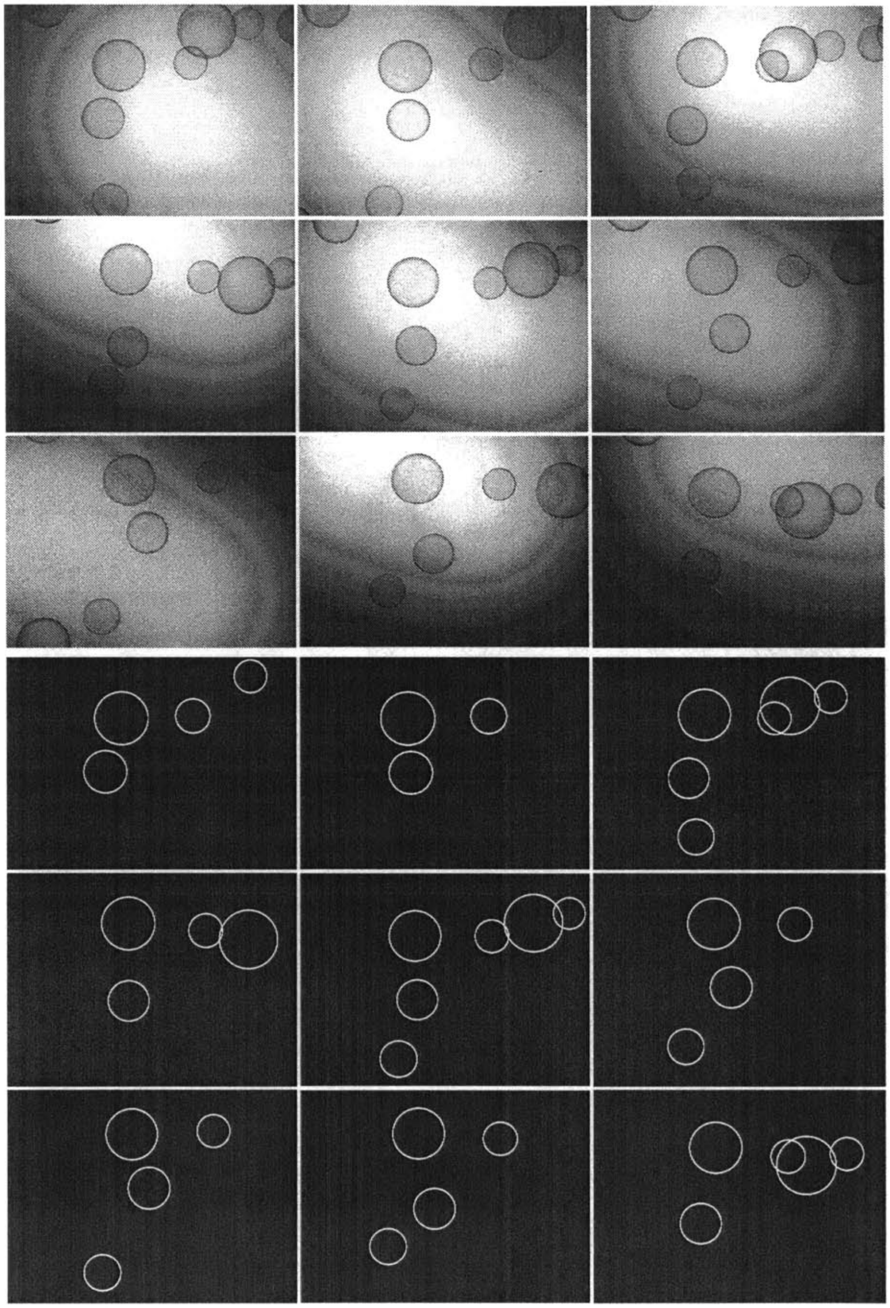

Figure 2-30: The upper nine raw images of bubbles were recorded by each of the nine cameras in the array at a particular instant in time. The lower nine binary images contain the circles that were detected in the upper raw images using a Circular Hough Transform.

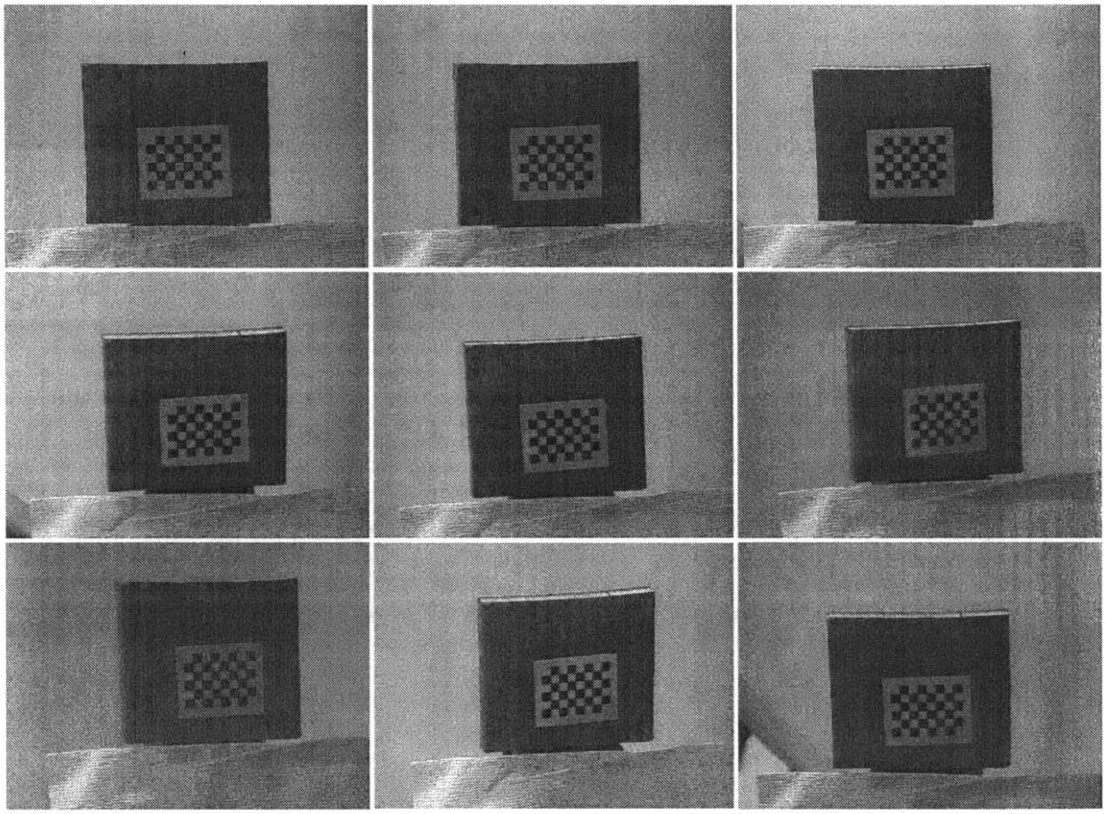

Figure 2-31: Images from each of the nine array cameras of the calibration grid in one particular orientation. Each grid square side length is 5 mm.

position and Lagrangian velocity data match the observed physical behavior of these bubbles, which are generally descending into the field of view, but have some motion in the X and Z directions as well. Figure 2-33 displays a histogram of the mean radii calculated over time for each of the unique 31 bubbles found. Consistent with observations from the two-dimensional videos, the overall mean radius is 17.00 mm with a standard deviation of 3.09 mm. Figure 2-34 presents a histogram of mean speeds for each of the detected bubbles. The overall mean and standard deviation are 0.30 and 0.10 m/s, respectively.

2.6 Conclusions

Spray flows are typically highly unsteady, three-dimensional, and often densely saturated with features, such as droplets or bubbles, that impact other droplets, leading to coalesce or breakup. This work shows the potential for imaging these complex features with novel three-dimensional imaging methods derived from the combination of light field imaging and synthetic aperture refocusing. Synthetic Aperture Feature Extraction is a novel method for reconstructing 3D scenes with partial occlusions. Multiple cameras arranged in an array may be used in a dark field or light field imaging setup to capture light rays from many angles from a 3D scene. Raw camera images are binarized using image processing techniques, such as circle or blob detection. After the cameras in the array are calibrated, the pre-processed raw images are then transformed and refocused using a synthetic aperture refocusing method. The resulting focal stack may then be thresholded in order to eliminate blur artifacts of features that are located at depths other than the target depth. This simplifies the task of extracting 3D voxel clusters. Finally, clusters with a number of voxels below a threshold may be eliminated to remove noise.

Simulations were used to validate the SAFE technique and to assess the error in sphere localization and radius measurement. Both dark and light field imaging setups have been tested and shown to be effective. Both square and circular camera array configurations with the same inscribed circle radius were tested in the reconstruction

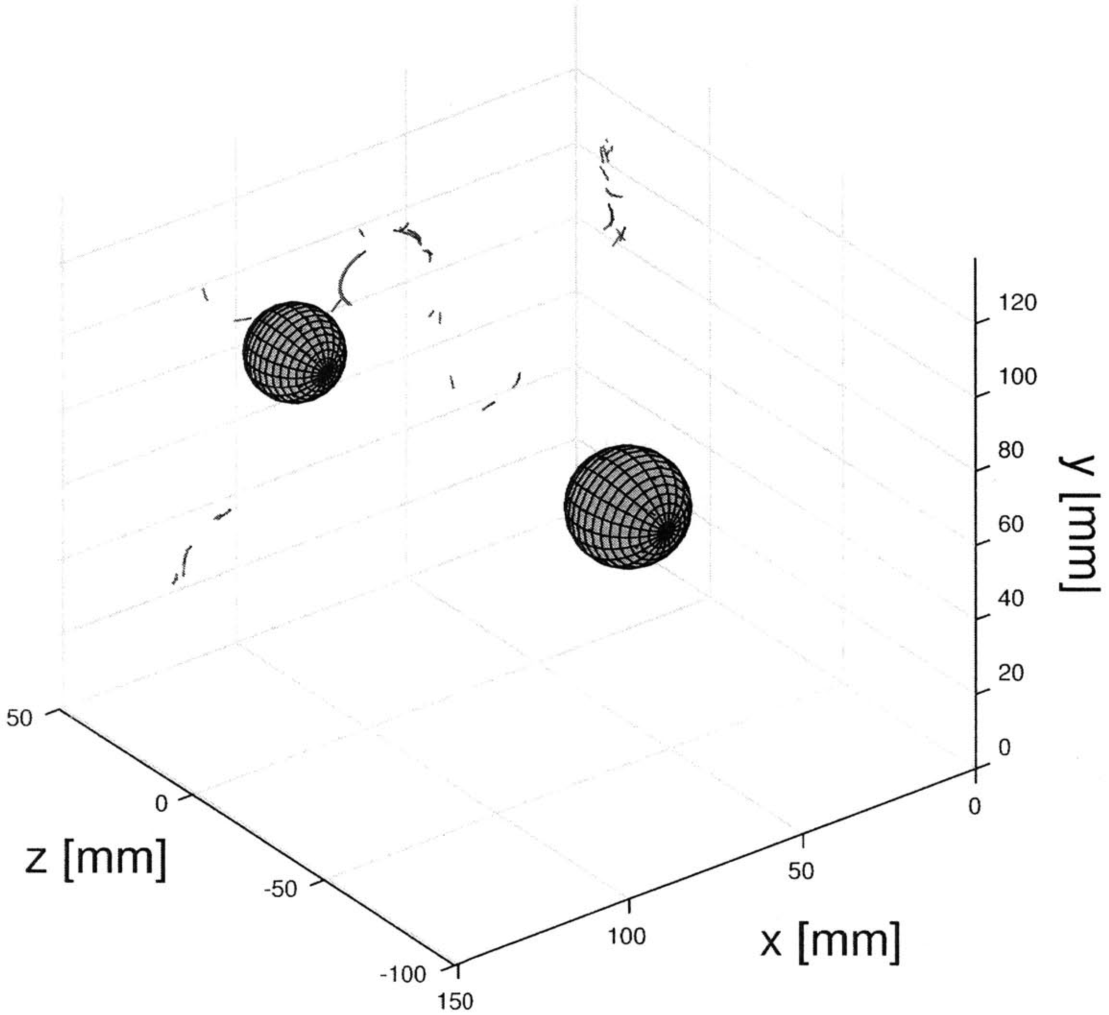

Figure 2-32: Three-dimensional reconstruction of bubbly flow. The two spheres correspond to two of the circular borders of the bubbles shown at the time step corresponding to Figure 2-30. The blue curves indicate spline fits to the trajectories of all of the tracked bubbles over time. The red arrows are velocity vectors calculated as time derivatives of these spline curves. Gravity is acting downward (in the -Y direction).

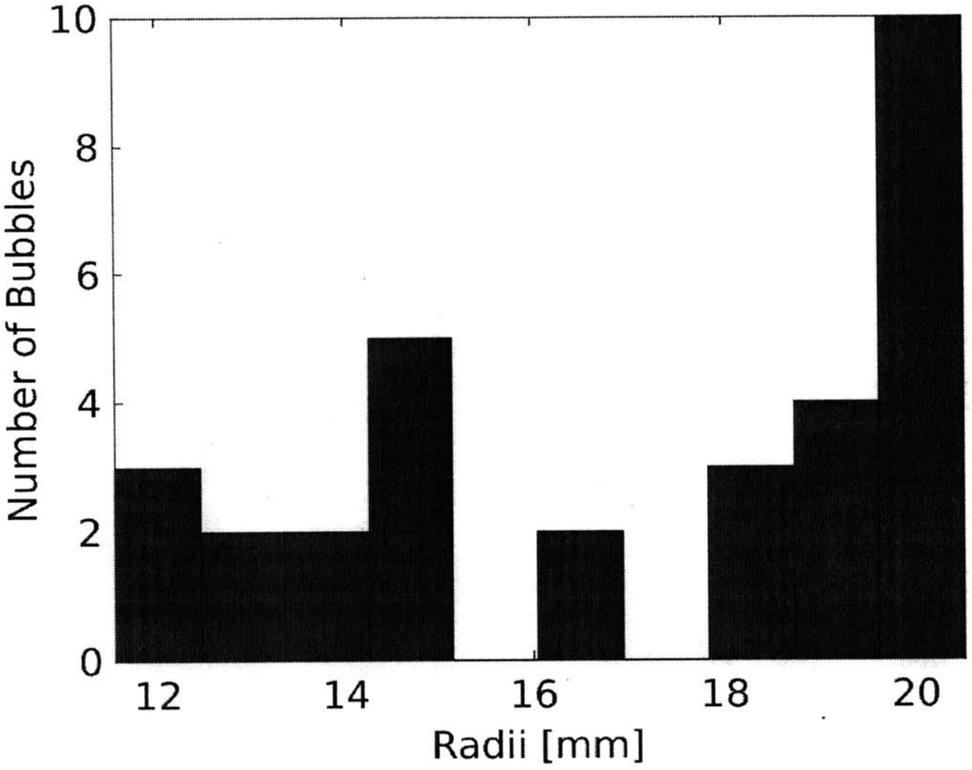

Figure 2-33: Histogram of the mean radii of each of the 31 unique detected bubbles over time. The overall mean radius is 17.00 mm with a standard deviation of 3.09 mm.

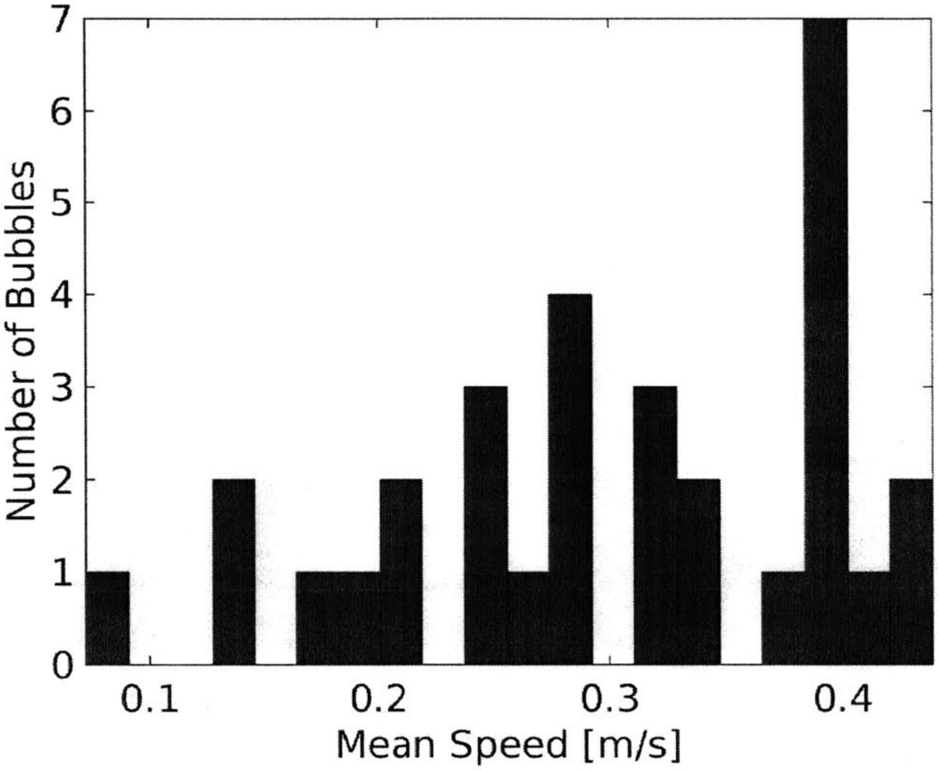

Figure 2-34: Histogram of the mean speed of each of the 31 unique detected bubbles over time. The overall mean speed is 0.30 m/s with a standard deviation of 0.10 m/s.

of spheres of varying radii at the world origin. Radius percent error measurements were generally lower for the circular camera configuration, possibly due to the more natural blur pattern produced by this arrangement during refocusing. Six light field imaging simulations were performed with an increasing number of spheres in a fixed volume. The spheres were generated at random locations and with random radii in the range of 1.5 to 4.0 mm. Good agreement between simulation and reconstruction is achieved, with maximum average errors in the X, Y, Z, and radius of 0.863, 0.817, 1.567, and 0.230 mm, respectively. The maximum average radius percent error was 9.495%. Average error in sphere localization and radius measurement generally increased with the occupied volume fraction. This is likely due to the difficulty in distinguishing individual spheres in the presence of greater optical density in the scene. At the highest occupied volume fractions investigated, the percentage of spheres that were missing from the reconstruction increased from 0 to 2.5% and, finally, 5% of the total number of spheres simulated in each trial. Additionally, experimental results on a soap bubble flow in air using SAFE show that reconstructed centroids and radii results agree with values measured in the individual raw camera videos.

The generality of this method allows it to be applied to other types of multiphase flows as well. In Chapter 4, the SAFE technique is applied to the study of human sneezes using an array of high speed cameras, as well as an extra camera to track the head motion. These highly three-dimensional, unsteady, optically dense spray flows involve the motion of high-speed, irregularly shaped droplet and ligament features with varying sizes that deform, fragment, and sometimes coalesce over time. Chapter 3 demonstrates the variety in the nature of the types of flow features observed in sneezes using cameras that record the scene from side and top views.

2.7 Acknowledgments

Abhishek Bajpayee and Leah Mendelson at the MIT Experimental Hydrodynamics Laboratory are acknowledged for their assistance with software development and the insights that they offered.

Chapter 3

Visualization of sneeze ejecta: steps of fluid fragmentation leading to respiratory droplets

This chapter by B. E. Scharfman, A. H. Techet, J. W. M. Bush, and L. Bourouiba has been submitted to the journal *Experiments in Fluids.*

3.1 Abstract

Coughs and sneezes feature turbulent, multiphase flows that may contain pathogen-bearing droplets of mucosalivary fluid. As such, they can contribute in spreading numerous infectious diseases, including influenza, SARS, and possibly Ebola. The range of contamination of the droplets is largely determined by their size. Uncertainty in the drop size distribution arising from violent expirations thus limit our mechanistic understanding of disease transmission. We here report direct observation of the physical mechanisms involved in droplet formation during sneezing. Specifically, we use high-speed imaging to visualize the dynamics of fluid fragmentation arising at the exit of the mouth. This is the first time that a rich variety of fragmentation phases are identified in the context of sneeze ejecta. Sheets and bags are observed to break into ligaments, which then separate into droplets in a sequence of events analogous to those reported in industrial applications. Insight into the dynamics shaping the final size distribution of droplets generated by sneezes and coughs is gained by analyzing

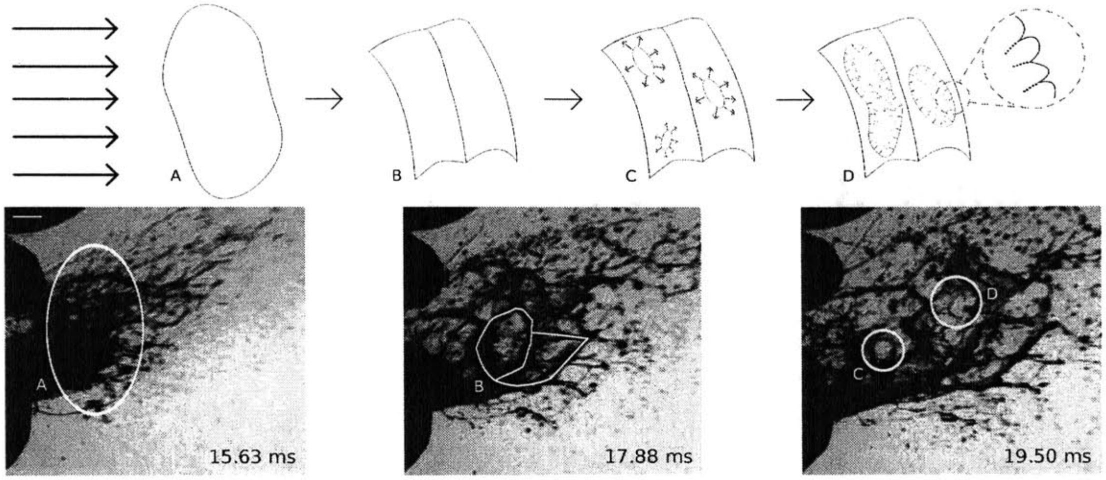

Figure 3-1: Schematic of the atomization process of a liquid volume in response to applied aerodynamic drag with sample experimental photographs recorded shortly after the first appearance of sneeze ejecta. The initial liquid volume (A) is flattened into a sheet (B), followed by hole formation (C) and subsequent destabilization into ligaments and, finally, droplets (D). Scale bar is 1 cm.

these fragmentation phases.

3.2 Introduction

A better physical understanding of the processes governing pathogen transport could help reduce the spread of deadly influenza strains such as H5N1, H7N9, or Ebola [17, 13]. Infected patients can produce virus-bearing droplets by sneezing, coughing, or even breathing [e.g. 63]. The size of such droplets spans the micrometer and millimeter scales, but no consensus on the drop size distribution can be found in the literature. Observations indicate that coughs and sneezes produce ejecta that are well described as a multiphase, turbulent cloud comprising buoyant, hot, moist air and suspended droplets [14, 15]. Momentum dominates the cloud's initial dynamics, while buoyancy may take over at a later stage, depending on the ambient conditions. A theoretical model describing the evolution of the cloud was developed by Bourouiba et al. [15] and validated against experiments. The turbulent gas-phase dynamics were shown to be critical in enhancing the range of the smaller suspended droplets by delaying their exit from the cloud. This model can be used to assess contamination ranges indoors under various physical conditions of the environment and patient. Inputs for this model include the volume fraction of liquid to gaseous phases and the droplet size distribution.

The techniques for measuring expiratory droplet size distributions have included microscopic enumeration on glass slides [21], optical counting [48], aerodynamic droplet sizing [35], interferometric Mie imaging [43], scanning mobility droplet sizing [75], and laser diffraction [76]. Despite these efforts, discrepancies persist between the reported size spectra. The variability in the composition and physical properties of the ejected salivary mucus is a major source of uncertainty for all estimations relying on calibrated optical characteristics and evaporation rates.

Hydrodynamic instabilities of fluid films at or near the exit of the respiratory tract play a critical role in setting the size distribution of the ejecta. Such fluid fragmentation phenomena are also found in nature and many industrial applications [71]. While the precise form of fluid fragmentation depends on the details of the source conditions, it generally involves a cascade to smaller scales, from a fluid volume to sheets, ligaments and, finally, droplets [23]. Here, we use high-speed imaging to observe the ejecta resulting from sneezes and coughs directly at the exit of the mouth. In §3.3 we discuss the possible physical mechanisms involved in the fluid fragmentation accompanying such violent expirations. The experimental setup and the results of our visualization of real human sneezes are presented in §3.4. In §3.5, we describe the anatomy of sneeze ejecta in more detail, with a focus on the type of fragmentation processes leading to droplets.

3.3 Physical picture and fluid fragmentation

The majority of the studies of drop size measurement [e.g. 76, 75, 43] focus on coughing, talking, or respiration. Turner et al. [68] used single flash photographs to record sneezes using a dark field imaging setup. Duguid [21] also studied sneezing; however, the sneeze dynamics examined were presumably altered by the subjects' ingestion of

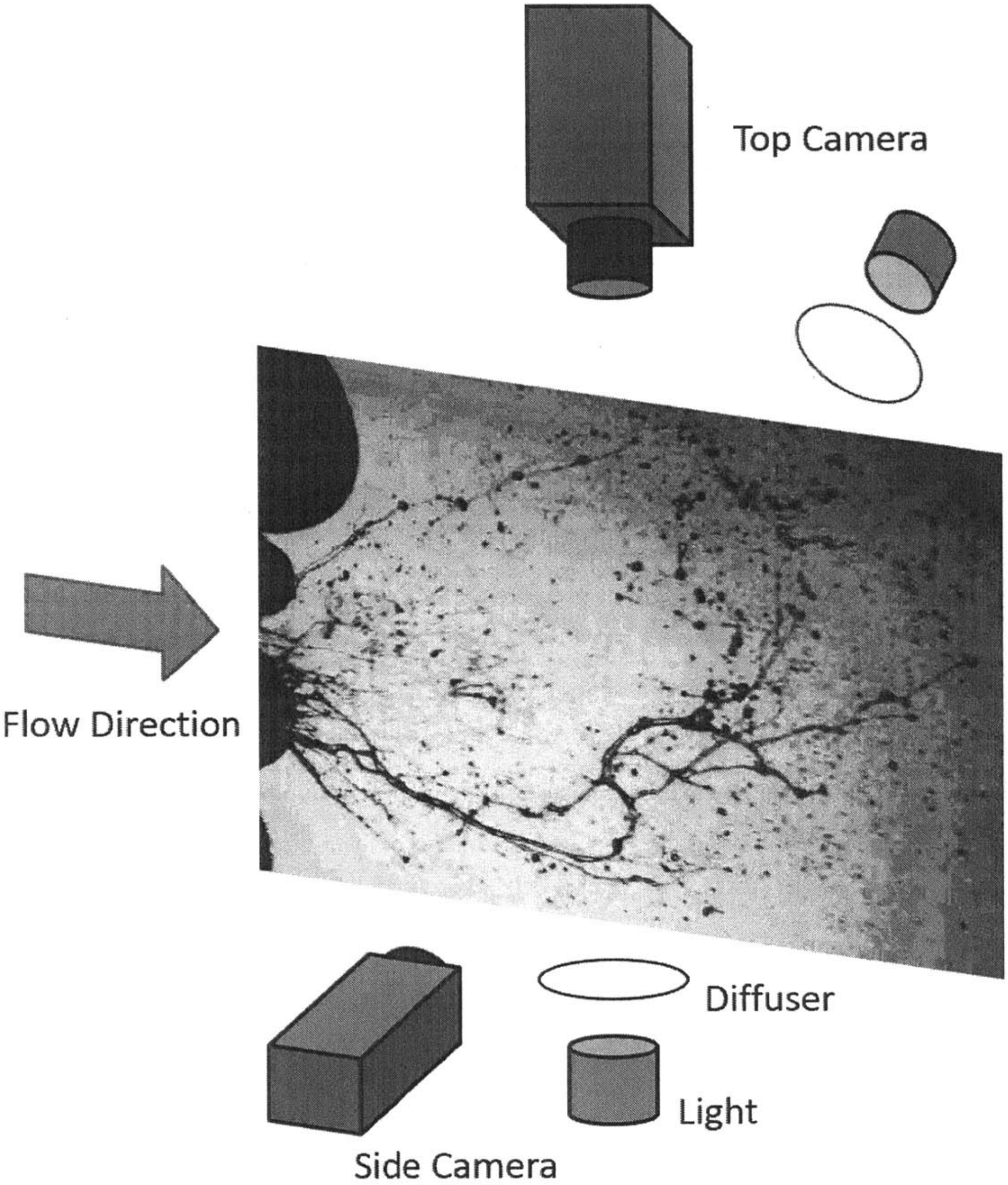

Figure 3-2: Schematic of the experimental setup used to image sneezes from both top and side views.

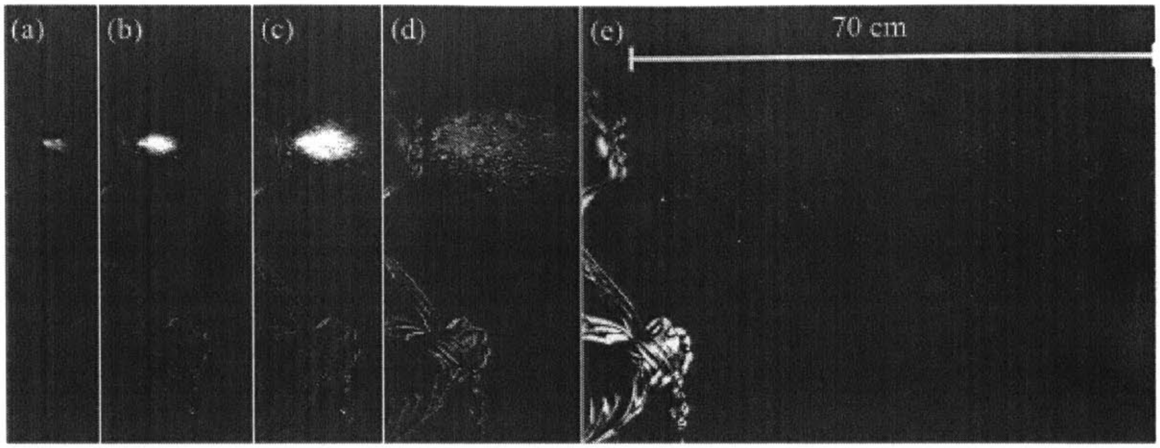

Figure 3-3: Cough recorded with high speed imaging at 1000 fps and displayed at (a) 0.005 s (b) 0.008 s (c) 0.015 s (d) 0.032 s and (e) 0.15 s from onset.

a dyed solution used for flow visualization in that study. Sneezing and coughing are often caused by an irritation of the nose and then trachea, respectively; this leads to nerve stimulation and the resulting reflex action [34]. It has been reported that the respiratory changes in a sneeze are analogous to those of a cough, except for the timing of the different phases [73]. In particular, both a sneeze and a cough consist of an initial irritation, a closure of the glottis, and a rapid increase in intrathoracic pressure. Following the re-opening of the glottis, air is expelled at high flow rates [5]. For the sneeze, the pharynx also seems to be constricted [73]; however, the subsequent dynamics remain poorly understood relative to those of the cough.

Within the airway system, sneezes and coughs consist of fast airflows interacting with relatively slow moving, thin fluid layers. It is thought that prior to ejection, droplets are generated within the respiratory tract, which is essentially a hierarchical network of branching airway tubes with radii varying from 0.9 cm in the trachea to approximately 150 μm in the alveoli [27]. A combination of Kelvin-Helmholtz and Rayleigh-Taylor instabilities can result in the destabilization of these layers into sheets and ligaments. These ligaments may then in turn destabilize into droplets via some combination of Rayleigh-Taylor or Rayleigh-Plateau instabilities [23]. These instabilities involve surface tension, viscous, and aerodynamic forces, the relative magnitudes

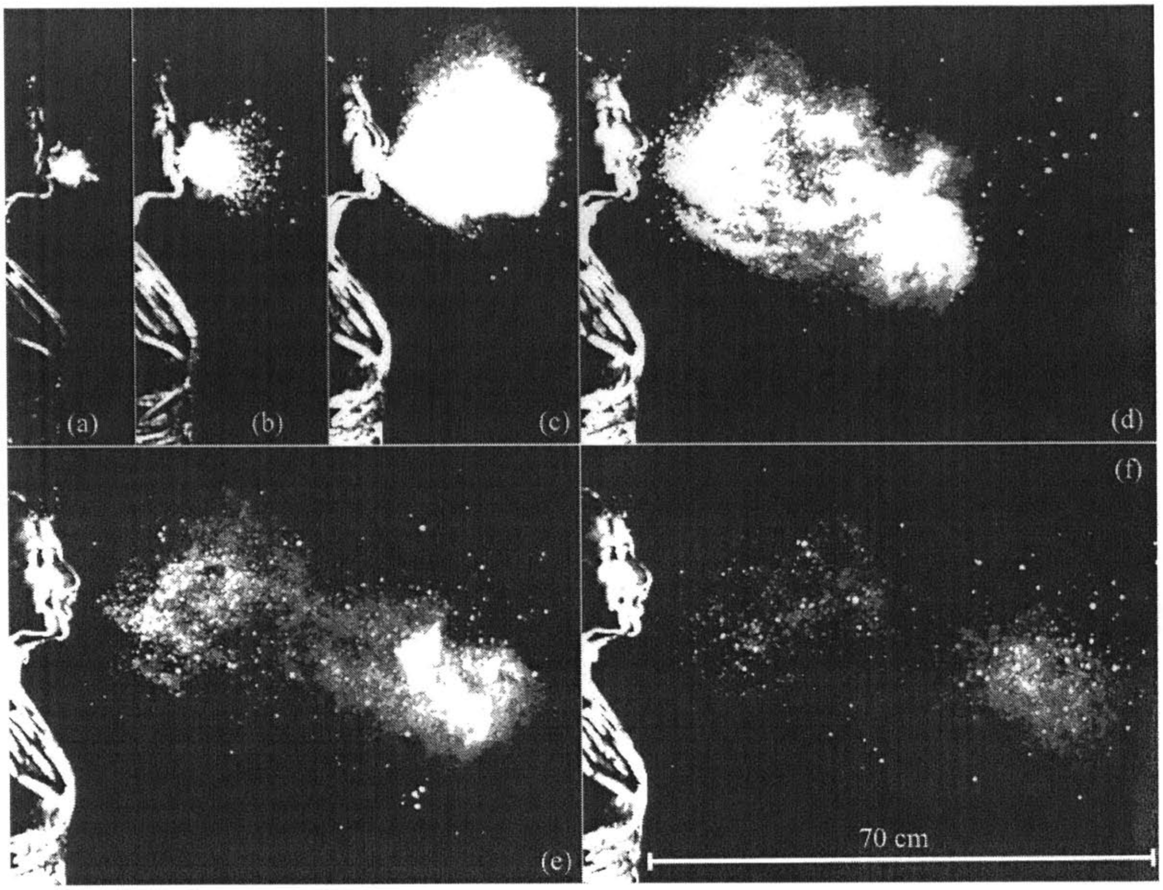

Figure 3-4: High-speed images recorded at 1000 fps for a sneeze at times (a) 0.007 s (b) 0.03 s (c) 0.107 s (d) 0.162 s (e) 0.251 s, and (f) 0.34 s. The multiphase sneeze cloud grows by turbulent entrainment as it advances.

of which determine the final size of the resulting pathogen-bearing droplets. Surface tension and fluid viscosity generally favor larger droplets, while higher air speeds tend to result in smaller droplets.

The liquid phase of origin is a mixture of saliva and mucus, the relative fraction of which is a function of the location within the respiratory tract. Reported physical properties of saliva are close to those of water with density $\rho = 1000$ kg/m ^{3} , dynamic viscosity $\mu = 1$ mPas and surface tension of $\sigma = 60$ mNm $^{-1}$ [62, 65]. These fluids are mostly composed of water (97%) and contain other agents such as salts, proteins, and fatty acids [6]. They are viscoelastic because of the dissolved large

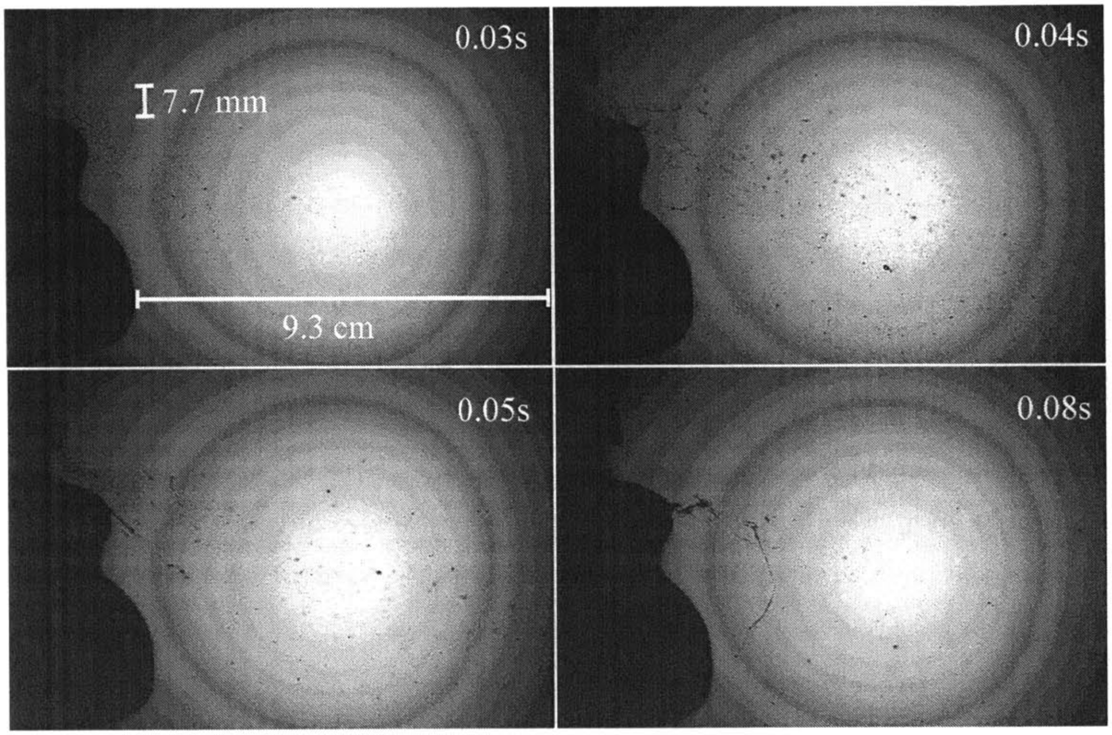

Figure 3-5: Stages of sneeze ejecta at (a) 0.03 s (b) 0.04 s (c) 0.05 s (d) 0.08 s after the onset of a sneeze. The sequence is recorded at 2000 fps using diffused backlighting.

glycoprotein mucins or biopolymers they contain. The mucins are macromolecules, such as MUC5B, MUC7, MUC4, etc, [20]. MUC5B is the dominant biopolymer, giving rise to relaxation times $2.24 \text{ ms} \leq \lambda \leq 76.2 \text{ ms}$ [30, 36, 7]. However, major discrepancies continue to persist in the values of relaxation time reported. When filaments of mucosalivary fluid are stretched, the polymers initially do not play an important role. They remain coiled and the solvent solution dominates the dynamics; hence, the thinning is dominated by viscous effects. In the subsequent phase, when the polymers become sufficiently stretched, they resist the surface tension-driven breakup that would occur via the Rayleigh-Plateau instability in a Newtonian fluid. Instead, filament stretching leads to the formation of previously reported beads-on-a-string when a balance of inertial, capillary, viscous, and elastic forces is achieved [11]. Beads-on-a-string are an indication of the influence of viscoelasticity, and play a role in selecting final sizes of the droplets. The Deborah number De quantifies the effect of viscoelasticity by prescribing the relative magnitude of the polymer relaxation time λ and timescale of fragmentation τ, $De = \lambda/\tau$. We observed typical mucosalivary ligaments of diameter ranging from 0.409 to 0.952 mm. For such sizes, the capillary time ranges from $\tau = \sqrt{\rho d^3/\sigma} = 0.97$ to 3.40 ms, leading to $0.65 \leq De \leq 78.73$. Other values reported in the literature on saliva include $0.004 \leq De = \lambda/\tau \leq 0.5$ [11]. This large variation in De values illustrate the major discrepancy in relaxation times reported in the literature for mucosalivary fluid.

Fluid partial bubbles, also known as bags, are another means of fluid breakup that appear in a variety of liquid-gas flows. Villermaux and Bossa [72] and Reyssat et al. [53] provide a detailed analysis of the physics of the birth and death of bags. Typically, a volume of liquid subjected to a net air flow in a particular direction is deformed by differential aerodynamic pressure that tends to flatten the volume into a sheet that expands as it is swept downstream (Fig. 3-1). The fluid is then transformed by the aerodynamic pressure into a bag structure that expands and thins until it becomes unstable and ruptures. The resulting holes expand at the Taylor-Culick speed [66, 19]. As the holes grow and the liquid shell destabilizes, ligaments form perpendicular to the bag rim surface due to the Rayleigh-Taylor instability of the rim and are stretched [38, 56]. These ligaments then eventually break into droplets via Rayleigh-Plateau-type instabilities (see Fig. 3-1).

In this study, we use direct visualization of sneezes via high-speed imaging to determine what modes of fragmentation are present at the exit of the mouth during violent exhalation events. These observations provide insight into the fragmentation dynamics that shape respiratory pathogen transport.

3.4 Experimental visualizations

3.4.1 Experimental setup

High-speed videos of sneezes and coughs were recorded using frame rates ranging from 1000 to 8000 fps (Fig. 3-2). Two monochrome cameras and various lighting configurations were used. First, the head of the subject was positioned in front of a black felt backdrop in order to create a dark field effect [68]. This approach allows for the droplets to scatter the light toward the cameras (Figures 3-3 and 3-4), which enhances their contrast. The light sources surrounded the observation area, but were never directly oriented toward the cameras. This setup was found to be optimal for the visualization of the far-field dynamics of sneezes, including sneeze cloud dynamics. By contrast, droplets at close range could best be visualized by using backlighting through a white diffuser. The fragmentation was recorded using one or two cameras simultaneously. In the latter case, single cameras were positioned above and on the side of the desired imaging area, respectively.

3.4.2 Coughs and sneezes

The set of images in Fig. 3-3 shows the evolution of cough ejecta from 0.005 to 0.15 s after initiation of the cough. The airflow expulsion lasted approximately 300 ms. A typical sneeze cloud from our visualizations is displayed in Fig. 3-4. The use of high-speed videography with at least 1000 fps was necessary in order to adequately resolve the dynamics. The set of images in Fig. 3-4 shows the evolution of the sneeze cloud from 7 ms to 0.34 s after the sneeze began. The airflow expulsion lasted approximately 200 ms. Using the flow speeds from our recordings in Figs. 3-3 and 3-4, we can estimate the Reynolds number $Re = Q/(d\nu)$, where d is the mouth diameter, Q the flow rate, and ν the viscosity of the multiphase cloud. We find Re to be roughly 10^4 and 4×10^4 for coughing and sneezing, respectively. The flow rate was determined by tracking the volume exhaled by unit of time from a combination of imaging and quantification of lung air volume capacity.

Our visualizations show that distinct cough droplets are already present at the exit of the mouth (see Fig. 3-3c-d for example), while such is not clearly the case for sneeze ejecta (Fig. 3-4). Fig. 3-4 shows a relatively dense sneeze cloud, with a broader spectrum of droplet or fluid fragment sizes, as remains visible further away from the source (Fig. 3-4f). The comparison of the two figures (Figs 3-3 and 3-4) suggests caution when generalizing the features of coughs to sneezes as is often done in the literature. As sneezes are the least well studied, we now focus on their ejecta.

3.5 Anatomy of sneeze ejecta

Figure 3-5 shows a sequence of close-up snapshots of sneeze ejecta recorded at 2000 fps. The duration of the sneeze is 150 ms. In addition to the expected droplet ejecta, we observe ligaments of various sizes. Here, the largest ligaments are 3 cm in length and are ejected at speeds of up to 35 m/s. The droplet sizes in this recording ranged from 160 μm to one millimeter, with a maximum observed speed of 14 m/s. The effects of viscoelasticity were also apparent in the ligaments, which exhibited the beads-on-a-string topology.

In order to characterize further the breakup of fluid following ejection from the mouth, we examine Fig. 3-6 in more detail. There, a dense field of sneeze ejecta is imaged both from the top and side. The side and top views were recorded at 8000 and 2000 fps with synchronized start-times, respectively. The total duration of the sneeze was roughly 134.5 ms with an estimated Reynolds number for the gas cloud of $Re_G = 10^5$. We observed a large number of droplet and ligament fragments. The longest ligaments were found to be at least as wide as the field of view, approximately

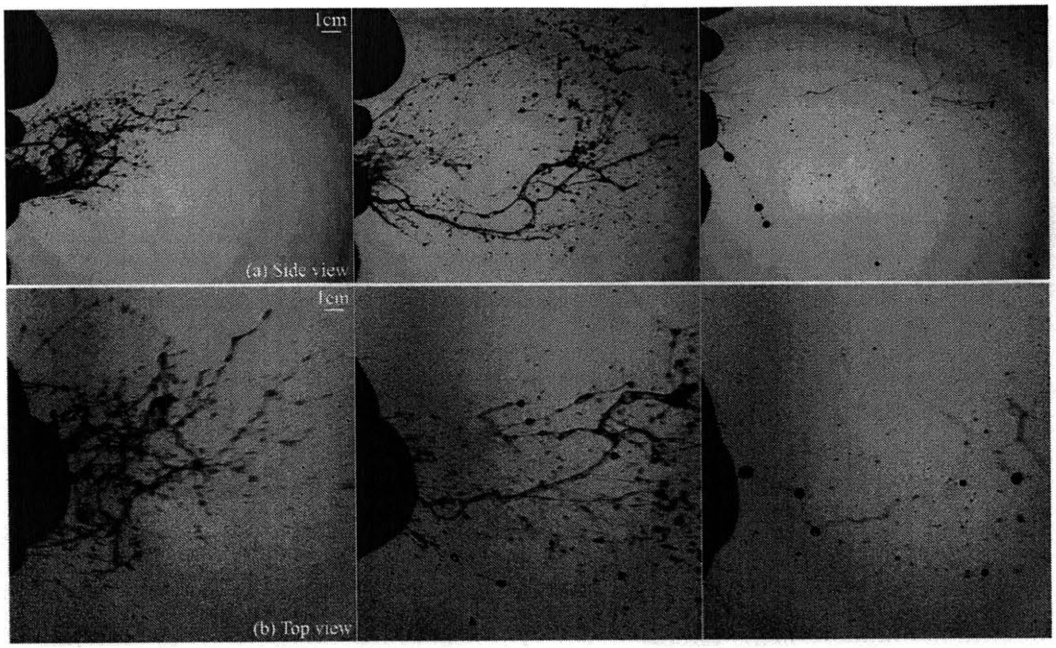

Figure 3-6: Stages of sneeze ejecta imaged from (a) the side and (b) the top, respectively. The first column features the initial sheet and bag bursting after 8 ms. The second column shows the ligament formation, elongation, and pearl formation at 21 ms, and the third column depicts the final stage of fragmentation into droplets at 117 ms. The side view was recorded at 8000 fps, while the top view was recorded at 2000 fps. Scale bars are 1 cm.

12 cm. The continuous breakup of the ligaments into droplets was apparent, as were other fluid fragmentation effects.

The first column of Fig. 3-6 illustrates fluid sheet expansion, the bursting of a bag-like fluid structure, and the transition from sheets to ligaments (Sec 3.5.1). The second column features the stretching of the residual ligaments and the associated droplet formation (Sec 3.5.2). The third column presents the final stage of the fragmentation process, the pinch-off of the ligaments into droplets. These three phases of fragmentation were observed systematically in the dozens of recordings captured.

3.5.1 Sheet extension and bag burst

In sneezes, we observe the formation of multiple bags of mucosaliva (e.g. Figs 3-7-3-9). The resolution of the raw images in Figs 3-7-3-9 has been increased using a

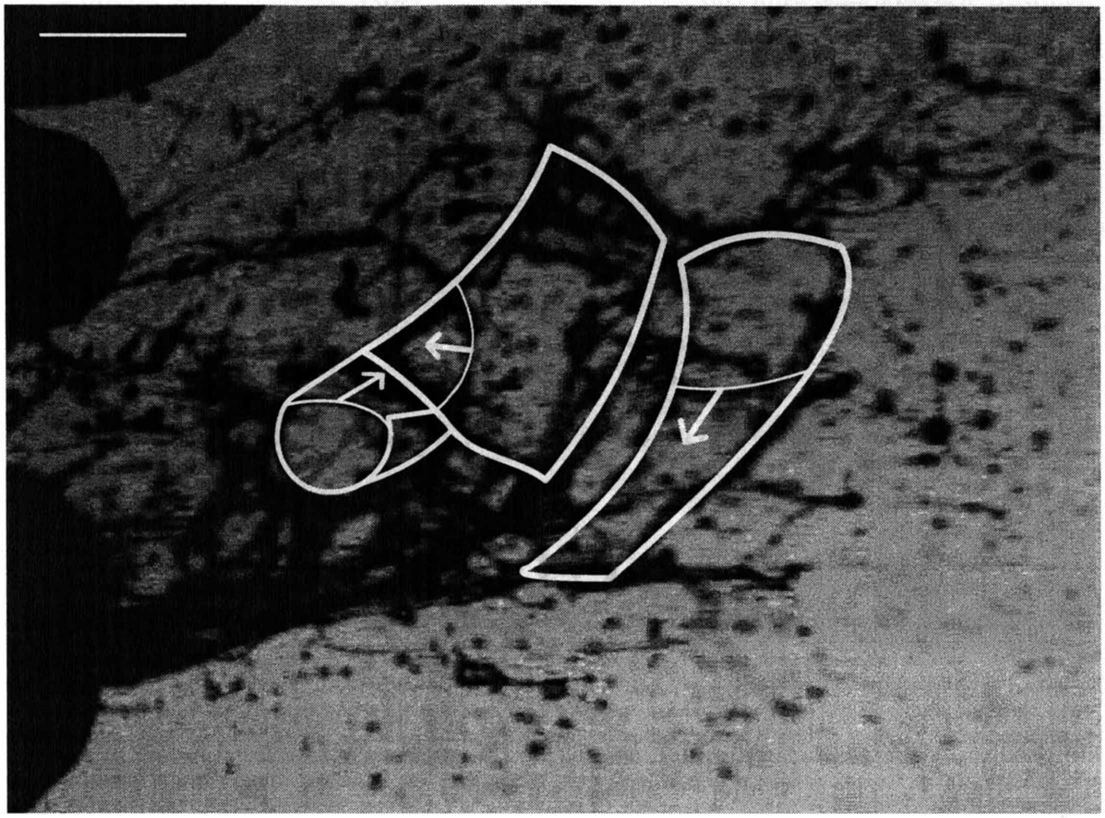

Figure 3-7: An example of multiple sneeze-induced expanding sheets after rupture. The image is shown at 22 ms after the sneeze began. Scale bar is 1 cm.

least-squares approximation for display purposes [44]. Fig. 3-7 shows an example of multiple expanding sheets after rupture. The white outlines show the bag edges, which are retracting in the directions indicated by the arrows. Residual ligaments from the piercing and retraction of the bags can be observed. In Fig. 3-8, an example of a bag located just downstream of the lower lip is reported. There, as the liquid exits the mouth, the fluid is flattened into a sheet and then transformed into a bag.

Figure 3-9 shows a bag that is in the flattened sheet phase of its growth. This particular bag is deflected downward and acquires little momentum in the downstream direction and it falls below the lower lip. Ligaments bounding the sides of this sheet radiate outward from it as the sheet expands and thins. Assuming a male lung capacity of 1.5 L, we infer a characteristic gas exhalation speed $U \approx 2.4$ m/s, corresponding to a gaseous Weber number $We_G = \rho_G U^2 d/\sigma \approx 2.2$, where $\rho_G = 0.9782$ kg/m ^{3} is the air density and $d = 3$ cm is the diameter of the mouth [50]. For individual Newtonian droplets, the critical We_G for transition to the bag regime is about 12 for Ohnesorge number $Oh_L = \mu/\sqrt{\rho d \sigma} < 0.1$ [51]. For a Newtonian liquid jet in crossflow, the transition from column to bag breakup occurs at a gaseous We_G of 4 [54, 55, 56].

3.5.2 Beads-on-a-string and merger

Figure 3-10 shows droplets, or beads, forming on the elongating ligaments of mucosalivary fluid ejected during the sneeze recording. The time sequence in Figure 3-10(b) shows two consecutive mergers of adjacent beads on the same ligament shown in Figure 3-10(a). This ligament of mucosalivary fluid is being stretched by the background air flow and has negligible viscous effects, since $Oh \approx 0.005$. The diameter of this ligament is approximately 0.2 mm, while the mean measured ligament diameter during the course of the sneeze is about 0.6 mm. In this low-viscosity regime, a Newtonian fluid ligament would be expected to fragment via a Rayleigh-Plateau instability on the capillary timescale $\tau_{RP} = \sqrt{\rho d^3/\sigma}$, where d is the initial diameter of the ligament. For example, the ligament observed in Fig. 3-10 would be expected to pinch off in approximately 330 μs; however, we see that the breakup is still in progress after more than 13 ms, owing to the retarding effects of viscoelasticity. That represent the extension of the filament lifetime by a factor of 39 when compared to that of an identical filament made of pure-water. With a Deborah number $0.65 \leq De \leq 78.73$ for the ligaments detected, the occurrence of beads and merger is expected to change the final drop size distribution relative to that expected for Newtonian fluids.

3.6 Discussion

Coughs and sneezes emit turbulent multiphase flows that can contain pathogen-bearing droplets of mucosalivary fluid. Despite recent efforts, no consensus on the size distributions of such droplets is reached in the literature. It is commonly assumed that the droplets are formed within the airway system with the process of their formation being unreported. In this study, we report direct visualization of cough and sneeze ejecta. We report that a rich set of fluid fragmentation processes are at play prior to the formation of the final sneeze droplet size distribution. In particular, sheet extension, puncture and retraction, lead to the formation of ligaments. Such ligaments stretch and form beads-on-string leading to mergers selecting for the final size of mucosalivary fluid residing in the air. These fragmentation mechanisms are clearly affected by the viscoelasticity of the mucosalivary fluid, with a typical delay in the breakup of the stretched ligaments formed. The droplets of relatively large size are generated during the breakup of the bags and filaments. Their size can range from a few hundreds of μm to 1.5 mm. However, there are also fluid fragments that exit the mouth in the form of smaller droplets. These are presumably created within the airway system and are typically smaller than those formed externally from ligament and sheet breakup. Such drops are much smaller than the 100μm detected herein. In a sample sneeze, the background exhaled air velocity was estimated to be 0.78 ± 0.52 m/s based on the velocity magnitude measurements of the 30 smallest droplets detected during the course of a sneeze that produced more than 100,000 small droplets over approximately 250 ms. A theoretical framework for understanding the effect of viscoelasticity on the fragmentation leading to the final sneeze drop size distribution is currently under development. Moreover, a more detailed analysis of the effect of each fragmentation process identified herein on the droplet size distribution is being investigated to further refine our assessment of pathogen transmission between hosts.

LB and JB acknowledge the financial support of the NSF (Grant DMS-1022356). The authors thank J. Bales, S. J. Lipnoski and the MIT Edgerton Center for access to their equipment. LB thanks the Reed and Edgerton Funds for financial support of studies in the fragmentation of mucosalivary fluids.

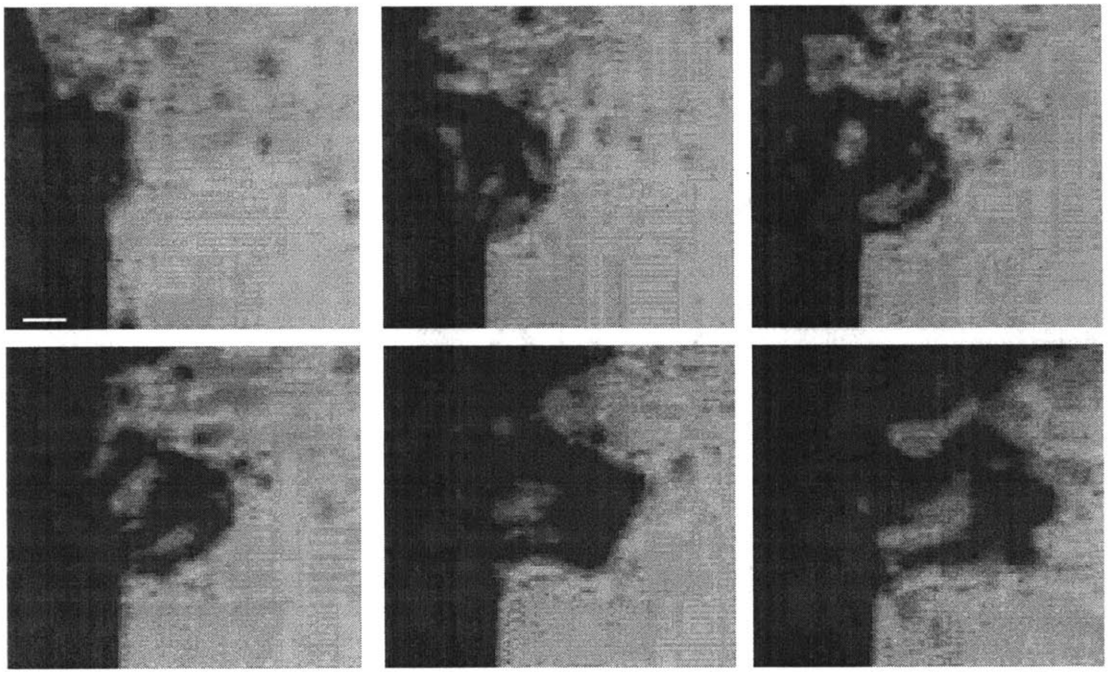

Figure 3-8: Development of the bag instability at the edge of the lip. The bag first grows into a mucus bubble then deforms prior to finally bursting. The snapshots are shown at intervals of 0.5 ms. The bag was originally roughly spherical in shape. This sequence was recorded at 8000 fps. Scale bar is 2 mm.

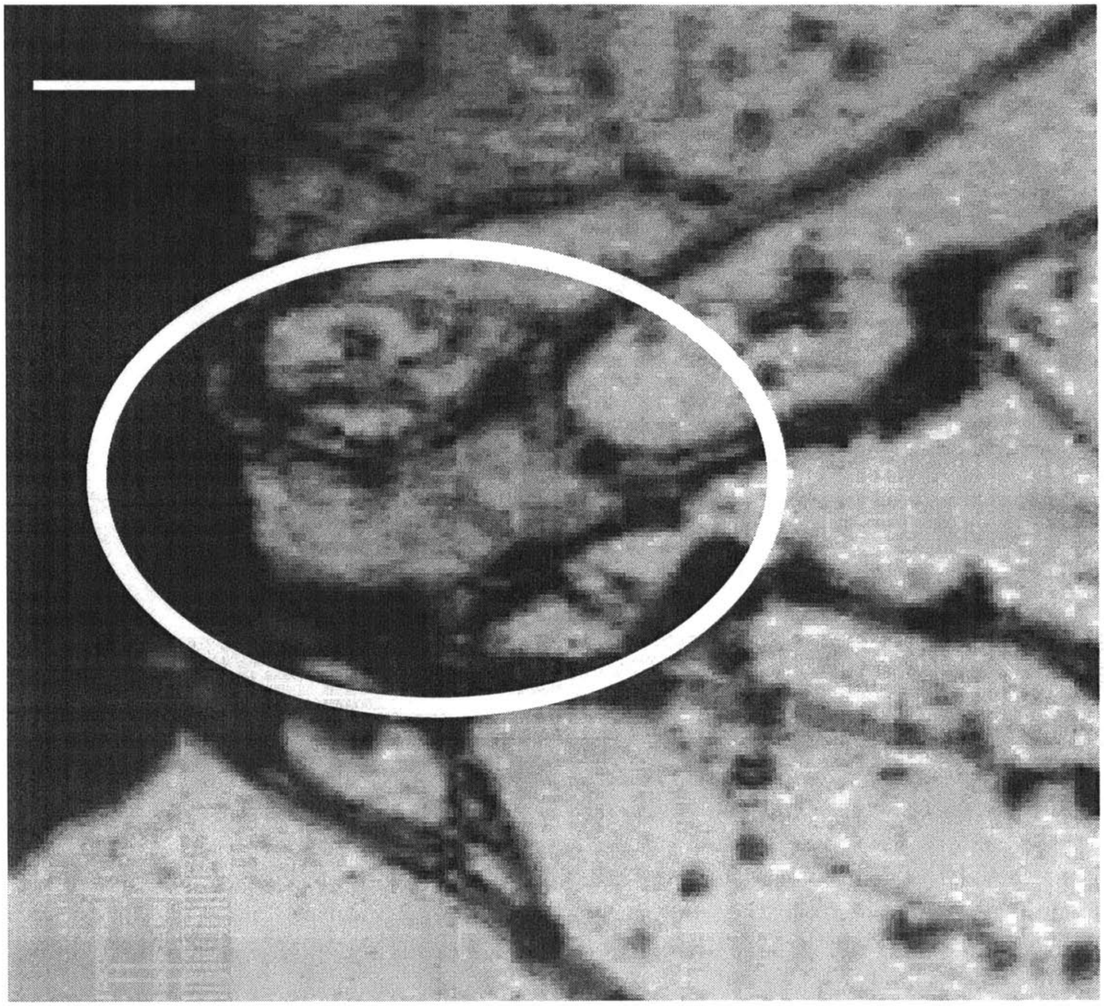

Figure 3-9: The bag shown here (enclosed in the oval) originates from the mouth near the lower lip. It is in the form of a flattened sheet of horizontal extent of approximately 16 mm. This image was captured at 40 ms from the onset of a sneeze. Scale bar is 5 mm.

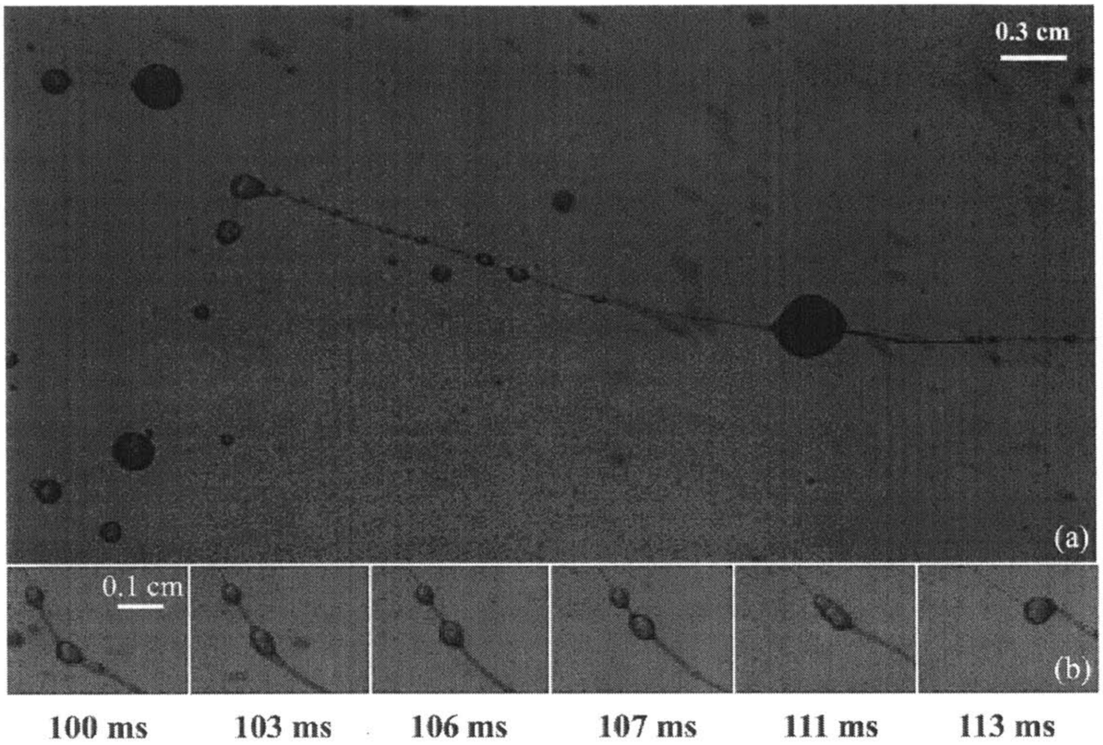

Figure 3-10: Beads on a string (a) Multi-scale droplets or "pearls" form on stretching ligaments owing to the influence of non-Newtonian effects. This snapshot is taken 130 ms after the onset of the sneeze and is viewed from above. (b) Time sequence showing two consecutive mergers of adjacent pearls. This particular sequence is observed on the largest ligament shown in (a), which has a width of about 0.2 mm.

Chapter 4

Three-Dimensional Imaging of Sneeze Ejecta

4.1 Introduction

The full three-dimensional (3D) time resolved measurement of sneeze spray droplets is necessary for understanding the potential disease transmission of a sneeze. Two-dimensional (2D) high speed imaging of sneezes, as described in Chapter 3, offers excellent insight into the fluid phenomena observed in sneezes, yet clearly illustrates the 3D nature of a sneeze spray. The 3D reconstruction of the flow field is necessary to understand the complete dynamics of these non-Newtonian, turbulent, unsteady multiphase sprays. In this chapter, we employ a nine camera high-speed rectangular light field imaging (LFI) array to image the mucosalivary fluid ejected during sneezing by a healthy human male, about 15 cm downstream of the mouth. An additional high-speed camera is used to track the sneezer's head motion and the ejecta that are present at the mouth exit. Droplet size, position, and velocity distributions are calculated over 3D space and time (3D+T) for the duration of the sneeze. In addition, the motion of the sneezer's head is tracked in order to understand the impact on the resulting spray downstream. As in Chapter 3, fluid bags, ligaments, and beads-on-a-string phenomena are also observed in this 3D study.

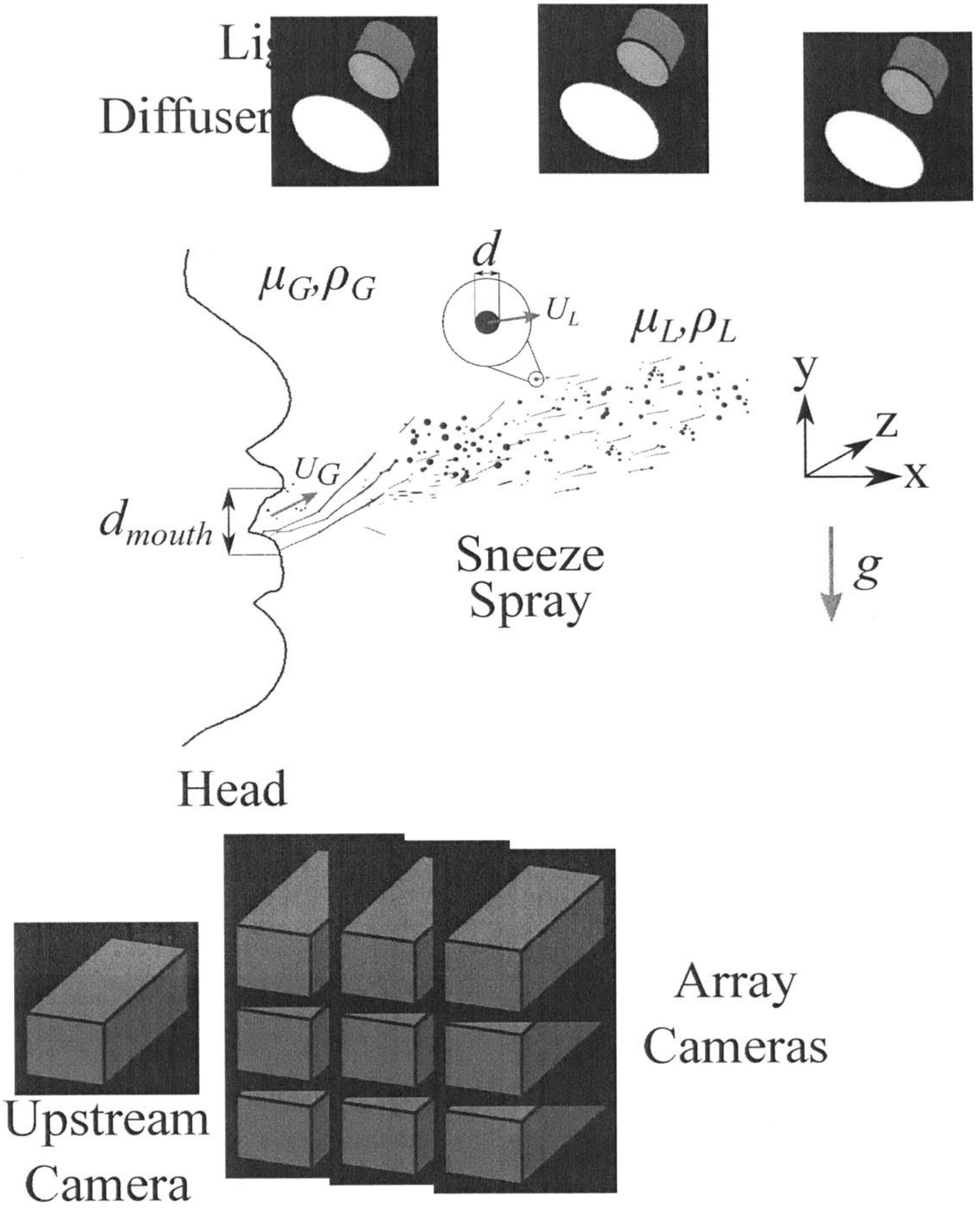

Figure 4-1: Three-dimensional sneeze imaging experimental setup schematic. The nine array cameras image the spray downstream of the mouth, while the additional camera simultaneously records the face.

Trial Index	DOF_{arr}	$FOV_{hor,arr}$	$FOV_{vert,arr}$	$FOV_{hor,face}$	$FOV_{vert,face}$
1	65.47	30.61	42.33	28.19	15.86
2	62.81	36.44	46.88	28.69	16.14
3	62.81	36.44	46.88	28.64	16.11
4	62.81	36.44	46.88	28.42	15.99
5	63.04	35.54	46.88	27.07	15.23
6	70.21	36.63	45.99	26.83	15.09
7	70.21	36.63	45.99	26.79	15.07
8	75.17	39.70	46.75	28.43	15.99
9	75.17	39.70	46.75	28.27	15.90

Table 4.1: The depth of field (DOF) is in the z direction, while the horizontal and vertical field of view (FOV) are in the x and y directions, respectively. The subscripts arr and $face$ refer to the array and upstream face tracking camera, respectively. The array camera values correspond to the extreme DOF and FOV calculated based on calibration of the corner array cameras. These bounds are plotted for Trial 2 in Figure 4-4. All quantities are reported in cm.

4.2 Experiments

4.2.1 Setup

The Synthetic Aperture Feature Extraction (SAFE) light field 3D measurement experimental setup is similar to that described in Chapter 2. Nine high-speed cameras are arranged in a rectangular grid pattern (see Figures 4-1, 4-2, and 4-5). A single high-speed camera located upstream of the array records the head of the sneezer and the ejection of fluid from the mouth from a side view. All of the array cameras are Phantom Miro M310 cameras fitted with 50 mm lenses, and the additional camera is a Phantom v341 with a 28 mm lens (see Figure 4-2). Videos are recorded by all cameras with a frame rate of 3187 fps and resolution of 1280 by 720 pix at F-stop of 16. Three pulsed LED light banks, manufactured by Integrated Device Technology, Inc., are synced with all of the cameras to provide back illumination of the scene behind a white diffuser. A Berkeley Nucleonics Corporation pulse/delay generator model 505 is used to sync the lights and cameras. Pulsed lighting is required to avoid streaking due to the high speeds of the sneeze droplets. Multiple lights are used in an attempt to uniformly illuminate the array cameras and to provide enough light, given the relatively small lens apertures and high camera frame rates.

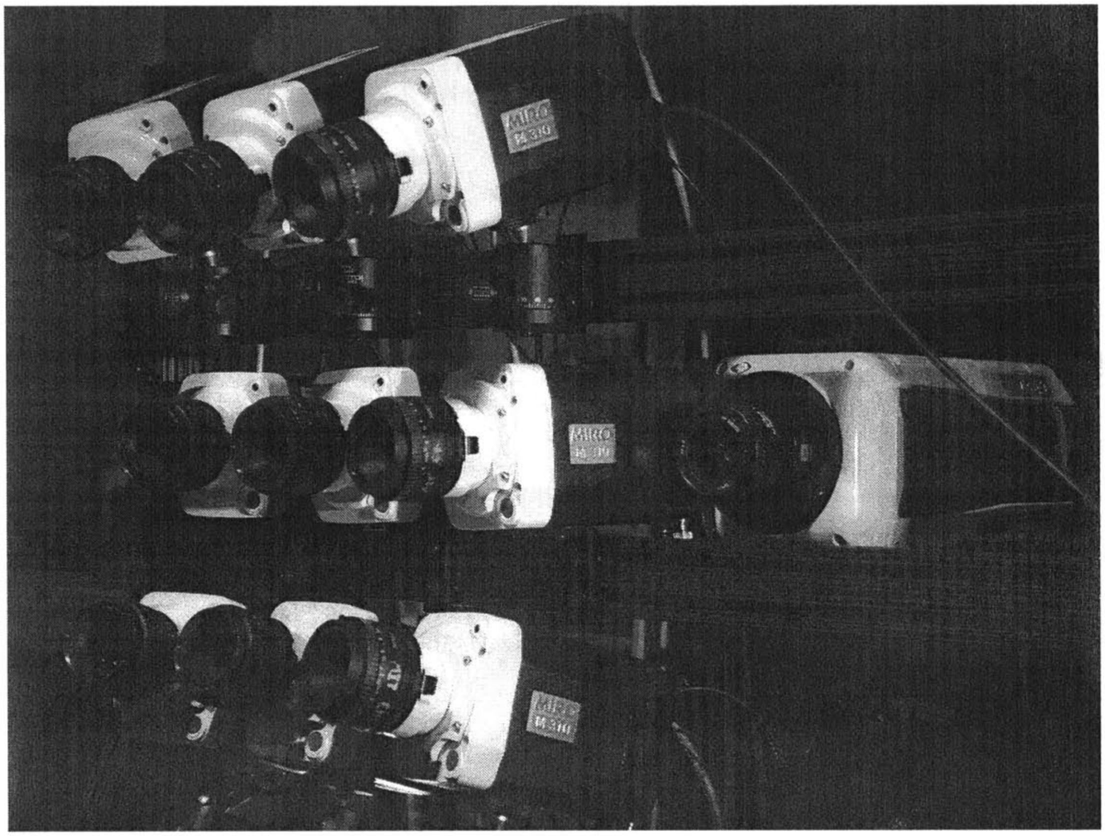

Figure 4-2: Photograph of nine array cameras (left) and additional side camera (right). All cameras are high-speed Phantom models manufactured by Vision Research, Inc. Photo credit: Antonio Pulsone.

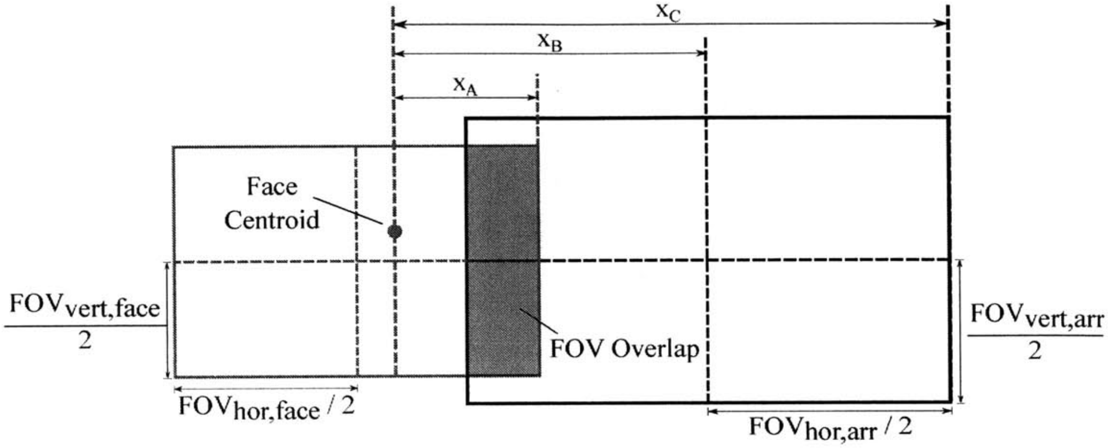

Trial Index	x_A	x_B	x_C
1	5.06	12.29	27.60
2	6.28	12.99	31.21
3	7.71	14.44	32.66
4	13.13	20.08	38.30
5	9.47	17.94	35.71
6	8.79	17.14	35.46
7	8.56	16.86	35.18
8	10.06	16.36	36.21
9	11.56	24.35	44.20

Figure 4-3: 3D sneeze experiments field of view (FOV) and sneeze extent dimensions for all trials (reported in cm). $FOV_{hor,arr}$ and $FOV_{vert,arr}$ are the horizontal and vertical field of view, respectively, of the array cameras, while $FOV_{hor,face}$ and $FOV_{vert,face}$ are the corresponding fields of view for the upstream face tracking camera. FOV values are provided in Table 4.1. The 2D centroid of the face at the release time (the last instant when liquid exits the mouth) is indicated by a red dot. x_A is the distance from the mouth at the release time to the right end of $FOV_{hor,face}$. x_B is the distance from the mouth to the center of $FOV_{hor,arr}$. x_C is the distance from the mouth to the downstream end of $FOV_{hor,arr}$. The FOV of the array camera and the additional camera overlap in these experiments.

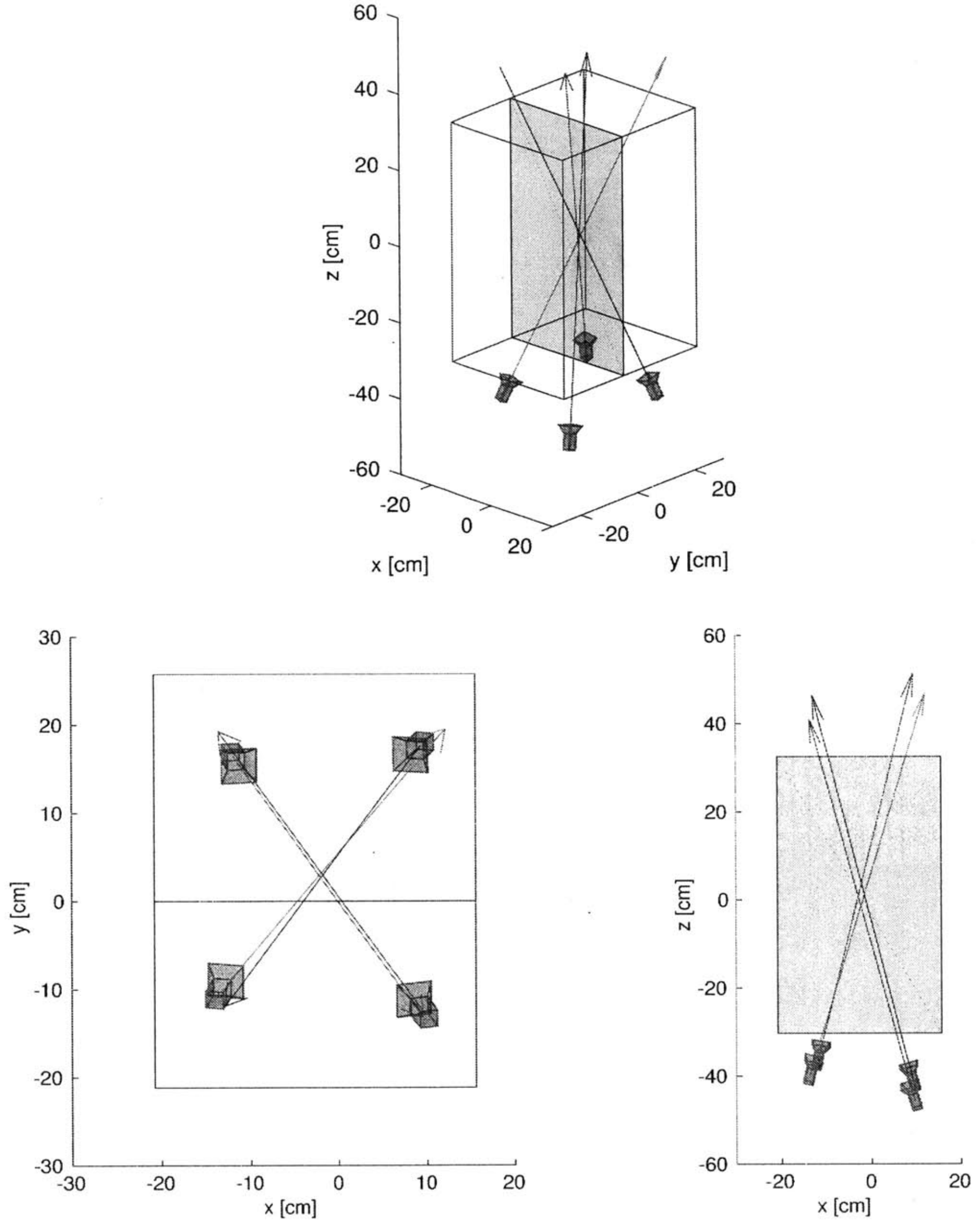

Figure 4-4: $x - y$ field of view and z depth of field, defined by the corner array cameras for one of the trials. The blue box defines the x, y, and z physical bounds of the refocused image stack. A plane is drawn at $y = 0$, where the intersections of camera rays define the focal bounds. (Top) Isometric view of the horizontal and vertical field of view and depth of field, along with the corner array cameras. (Bottom-Left) $x-y$ view, showing the field of view. (Bottom-Right) Corresponding $x-z$ view, showing the horizontal field of view and the depth of field.

The sneezer sits perpendicular to the image plane of the of the additional side camera and within its field of view. After sneezing is induced, the subject sneezes into the field of view of the array cameras. As in Chapter 3, the head is not constrained so as to simulate natural sneeze conditions. All sneezes are generated by one healthy male test subject. A target is placed in front of the sneezer to help orient the test subject so that the sneeze is directed straight ahead in the $+x$ direction. Protective glasses are worn to shield the sneezer's eyes from the bright LED lights. All nine trials are performed at room temperature. Trials 1 through 4 take place during a span of one day, and the remaining trials are recorded the following day.

The cameras are triggered with a BNC hardware trigger. The nine array cameras are calibrated using a checkerboard calibration grid, as described in Chapter 2. As discussed in Chapter 2 in §2.3.3, the extreme focal bounds in the x, y, and z dimensions can be calculated based on camera calibration. The field of view (FOV) and depth of field (DOF) for Trial 2 are illustrated in Figure 4-4. The focal bounds for all trials are listed in Table 4.1. The intersection of the rays emanating from the four corner cameras with the planes $x = 0$ and $y = 0$, respectively, are used to calculate the focal extent in all three spatial dimensions. The DOF is important for refocusing because processing depth slices outside of the DOF can lead to incorrect reconstructions and an unnecessary increase in computational costs. A yard stick positioned to span the fields of view of the array cameras and the additional camera is recorded simultaneously by all cameras in order to determine the relative position of the face camera and the array. Figure 4-3 presents the overlapping FOV dimensions of the upstream face tracking camera and the effective FOV of the nine array cameras. The 2D $x - y$ face centroid at the release time (the last instant when liquid is observed to exit the mouth) is indicated by a red dot, and the distances x_A, x_B, and x_C are measured from this point. $FOV_{hor,arr}$ and $FOV_{vert,arr}$ are the horizontal and vertical field of view, respectively, of the array cameras, while $FOV_{hor,face}$ and $FOV_{vert,face}$ are the corresponding fields of view for the upstream face tracking camera. x_A is the distance from the mouth to the right end of $FOV_{hor,face}$. x_B is the distance from the mouth to the center of $FOV_{hor,arr}$. x_C is the distance from the mouth to the

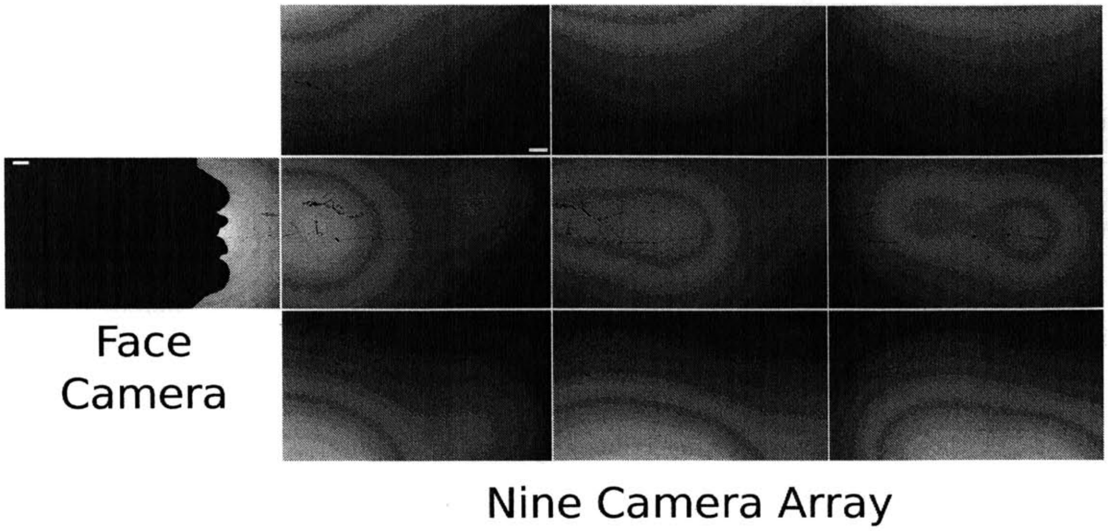

Figure 4-5: Montage of sneeze photographs recorded by each of the nine cameras in the array (nine images on right) and the additional upstream camera (shown on left). The layout of the images in this figure indicates their relative locations in the camera array when looking into the cameras. These images from Trial 2 were recorded 141.20 msec after the start of the sneeze. The scale bar in the left-most image corresponds to the upstream camera calibration, while the scale bar in the top-left array camera image corresponds to the array cameras calibration. Both scale bars are 2 cm. Note here the field of view overlap between the camera tracking the face and several of the array cameras (see Figure 4-3).

downstream end of $FOV_{hor,arr}$ and is the total observable extent of the sneeze. Here, the near field sneeze spray is analyzed, and the maximum value of x_C is 44.20 cm in Trial 9. Bourouiba et al. [15] image the sneeze cloud up to 70 cm from the mouth.

4.2.2 Parameter regime

The fluid properties of the mucosaliva, which are summarized in Table 4.2, are the same as those described in Chapter 3 section 3.3. The average exhalation gas speed, U_G, is estimated as

$$U_G = \frac{V_{lung}}{t_s(\pi d_{mouth}^2/4)}, \tag{4.1}$$

where V_{lung} is lung capacity (assuming a male lung capacity of 1.5 L as in Chapter 3), t_s is the sneeze duration, and d_{mouth} is the mouth diameter at the release time. The values of t_s and d_{mouth} for each trial are found in Table 4.3. Mean liquid velocity

Parameter	Symbol	Range
Air density	ρ_G	0.98 kg m^{-3}
Air dynamic viscosity	μ_G	1.84E-5 Pa s
Exhalation gas speed	U_G	9.99 - 45.67 m s^{-1}
Liquid density	ρ_L	1000 kg m^{-3}
Liquid dynamic viscosity	μ_L	1 mPa s
Liquid droplet average speed	U_L	2.43 - 3.53 m s^{-1}
Surface tension	σ	60 mN m^{-1}
Mouth diameter	d_{mouth}	1.32 - 2.26 cm
Average droplet diameter	d	0.25 - 2.0 mm

Dimensionless Group	Definition	Range
We_G	$\rho_G U_G^2 d_{mouth}/\sigma$	21.47 - 768.66
M	$\rho_G U_G^2/\rho_L U_L^2$	7.8E-3 - 0.35
Oh	$\mu_L/\sqrt{\rho_L \sigma d}$	2.9E-3 - 8.2E-3
Re_G	$\rho_G U_G d_{mouth}/\mu_G$	7.0E3 - 5.48E4
Re_L	$\rho_L U_L d/\mu_L$	608 - 7060

Table 4.2: The parameter regime explored in the present 3D experimental study of sneezes.

(U_L) data and statistics are shown in Table 4.4. Average sneeze droplet diameter, d, statistics are displayed in Figure 4-19.

Table 4.2 also shows the relevant dimensionless parameters for analysis of the sneeze. The gaseous Weber number, $We_G = \rho_G U_G^2 d_{mouth}/\sigma$, is the ratio of inertial to surface tension forces. $M = \rho_G U_G^2/\rho_L U_L^2$ is the gas-to-liquid momentum flux ratio. $Oh = \mu_L/\sqrt{\rho_L \sigma d}$ is the Ohnesorge number, which is the ratio of the viscous force to the square root of inertial and surface forces. $Re_G = \rho_G U_G d_{mouth}/\mu_G$ and $Re_L = \rho_L U_L d/\mu_L$ are the Reynolds numbers for the gaseous and liquid phases, respectively, which are ratios of inertial to viscous forces. Since $Oh \ll 1$, $Re_G \gg 1$, and $Re_L \gg 1$, viscous forces are negligible compared to inertial and surface tension forces. $We_G \gg 1$ indicates that the inertia of gas exhaled from the mouth dominates surface tension, leading to liquid deformation and atomization. According to Hopfinger's coaxial gas stream liquid jet atomization regime map with dimensions of Re_L, We_G, and M, the parameter space in the present study would be within the shear breakup regime [37]. However, the sneeze is a more complex flow because the entire volume of mucosaliva liquid is exposed to gas exhalation, rather than gas simply flowing around the border of a liquid jet. Liquid also does not exit the mouth as a jet; rather, atomization begins further upstream. Chapter 3 discusses the instabilities that are observed in a sneeze. Bag instabilities are observed near the mouth as the liquid volume deforms into a flattened sheet, which then atomizes further into ligaments with beads-on-a-string (a non-Newtonian fluid phenomenon) and, ultimately, individual daughter droplets. Although all of these instabilities are visible in the recorded videos in the present study as well, only individual beads found on ligaments and free droplets are ultimately reconstructed and tracked in 3D over time. The SAFE technique employed here produces the most accurate results when imaging objects that are close to spherical in shape, as discussed in Chapter 2 §2.3.5.

4.2.3 Head Tracking

In the analysis of sprays, the nozzle geometry and motion, if any, can have a large impact on the resulting downstream flow. Therefore, it is important to track the motion of the head and diameter of the mouth during sneezing. The position of the head relative to the array cameras can also affect the number and size of droplets and other fluid features observed in the 3D reconstruction. The single high-speed camera located upstream of the nine array cameras is used to track the motion of the sneezer's head. The face appears as a silhouette due to the back-lighting setup (as seen in Figures 4-5 and 4-6).

Figure 4-6 presents an example of face contour extraction at a single time instant. The raw image from the upstream camera is first thresholded. The sharp contrast between the almost completely black silhouette and the bright background allows the sneeze spray to be removed with a low threshold relative to the maximum intensity (in this example, the threshold is 2 out of a possible 255). Then edge detection is performed using the Sobel method. Since the head faces right in all images, the right-most contour is retained after edge detection. As can be seen in Figure 4-6d, keeping only the right-most edge pixels eliminates the edge of the glare on the test subject's protective glasses, which can be seen in the prior processing steps. However, the right-most contour may still contain gaps, which are then connected via horizontal

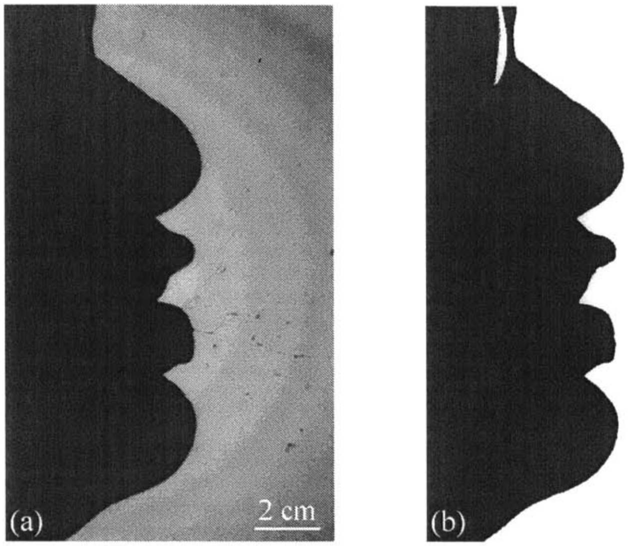

Raw Thresholded, T = 2

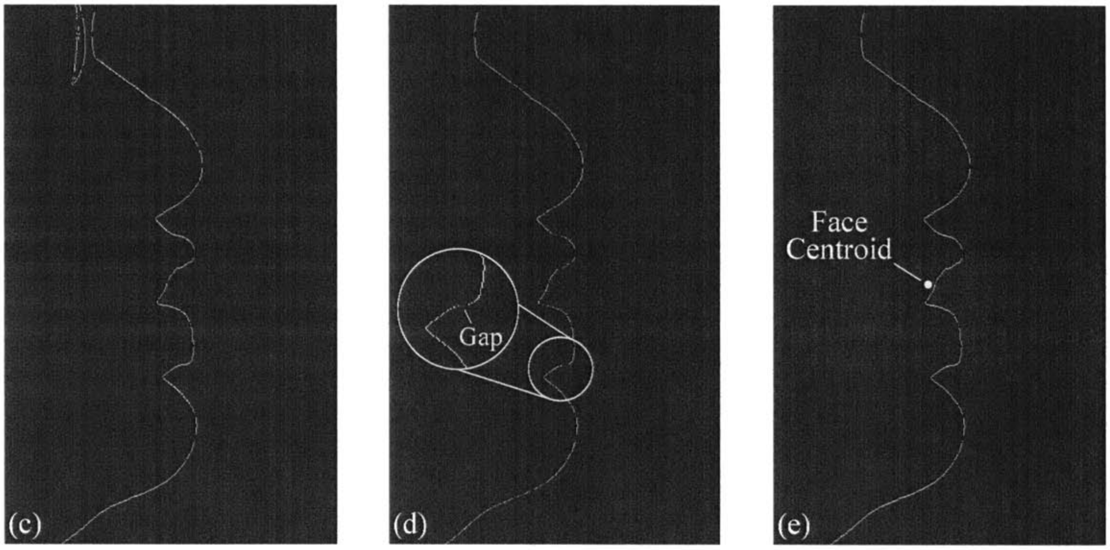

Edges Detected Right-most Contour Final Connected Contour

Figure 4-6: Face tracking example from Trial 1, 118 msec after the start of the sneeze. (a) Raw images of the face are captured throughout the duration of the sneeze. (b) Images are converted to binary using a low threshold value to retain only the pixels that correspond to the face. (c) Edges are detected using the Sobel method to obtain the face contour. (d) The right-most nonzero pixels in each row are extracted to eliminate artifacts due to the protective glasses and duplicate pixel detections. However, there may be gaps present in some of the rows. (e) These gaps are connected by filling in pixels horizontally. After this, the 2D facial centroid can be calculated for each frame and tracked over time.. All images in (a)-(e) have been cropped from the left side, where no additional facial features can be observed.

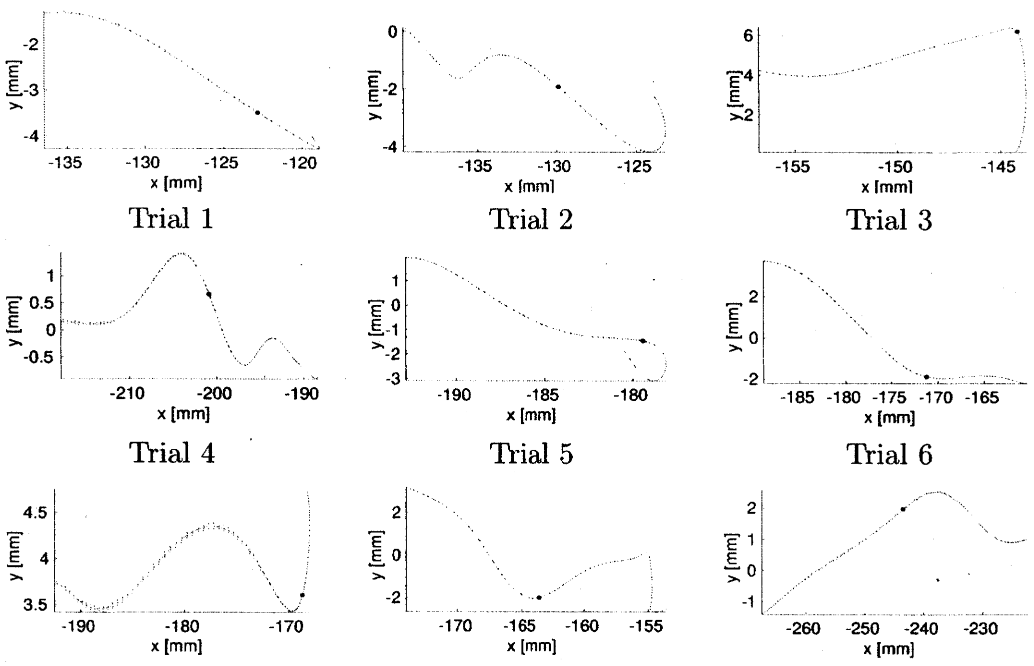

Trial 1

Trial 2

Trial 3

Trial 4

Trial 5

Trial 6

Trial 7

Trial 8

Trial 9

Figure 4-7: 2D face centroid tracking runs for all trials. A velocity vector corresponding to every tenth frame (magnitude in m/s) is shown, and the vector scale factor is 2.5. The black dots correspond to the centroid head positions at the release time in each trial. x and y distances are relative to the center of the world coordinates, at which the array cameras are aimed.

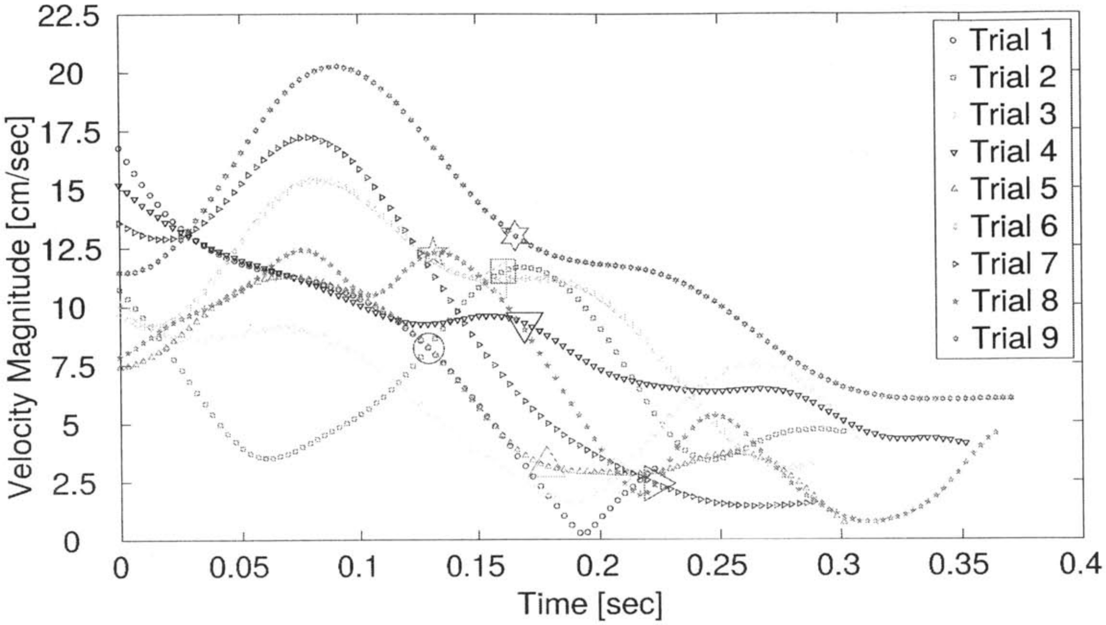

Figure 4-8: Two-dimensional face centroid velocity magnitude over time. Speed at every tenth time step is plotted. The enlarged symbols correspond to the head speed at the release time.

lines, resulting in the final contour shown in Figure 4-6e. Then, the 2D face geometric centroid is calculated from the $x - y$ contour coordinates. The centroid of the contour is tracked in the x and y directions to calculate the velocity of the head during the course of the sneeze. However, the head actually moves in the z dimension as well and in general may rotate about any axis in 3D.

Figure 4-7 presents velocity vectors at the $x - y$ centroids of the face during the sneeze. Coordinates are relative to the center of the world frame, at which at the array cameras are aimed. The first vector shown at the left in each plot corresponds to the start of the sneeze, when liquid is first observed to exit the mouth. The black dot in each plot represents the head's location at the release time. Figure 4-8 shows the velocity magnitude of the head as a function of time. The release times are marked by enlarged symbols. The mean head speeds are an order of magnitude less than those of the average sneeze droplets (see Table 4.4).

The diameter of the mouth in the face tracking camera image plane is measured

Figure 4-9: Refocusing an image volume at different depths using digital light field photography (reproduced from [45]).

from the face contour (see Figure 4-1). This diameter is observed to increase over time during each sneeze as fluid is forced out of the mouth. At the release time, the mean mouth diameter, d_{mouth}, is 1.77 ± 0.33 cm (Table 4.3), corresponding to open mouth areas of 2.53 ± 0.95 cm^2. For experiments on coughing, Gupta et al. [28] reported mouth areas of 4 ± 0.95 cm^2 for males and 3.37 ± 1.4 cm^2 for females, respectively. Bourouiba et al. [14] estimated the mouth area to be 3.4 cm^2 during a cough.

4.3 3D Spray Image Analysis

4.3.1 Light Field Imaging

In order to record the downstream sneeze spray in 3D, an array of cameras is used in a light field imaging setup. Light field imaging and synthetic aperture refocusing techniques have been combined in an emerging method to resolve 3D flow fields over time [8]. This technique is well suited for analysis of multiphase spray flows like sneezing because it enables "seeing through" partial occlusions. LFI involves a large number of light rays from a scene being collected and subsequently reparameterized based on calibration to produce a 3D image [33]. In practice, one method used by researchers in the imaging community for sampling a large number of rays is to use a camera array [69, 70] or, more recently, a single imaging sensor and a small array of lenslets (lenslet array) in a plenoptic camera [40]. Figure 4-9 presents an example of the application of LFI. After the complete image volume is recorded, different depth slices can be extracted from the resulting focal stack. In each of these slices, only the features that are actually located at that depth appear in focus, while everything else appears blurred.

The starting point for volume reconstruction is the implementation of the synthetic aperture algorithm to generate refocused images on planes throughout the volume. Thereafter, the actual particle field must be extracted from the refocused images and organized into a volume with quantifiable locations. First, mapping functions must be established between the camera image planes and world coordinates

$$\mathbf{u}^i{}_j = F(\mathbf{X}_j; p^i), \tag{4.2}$$

where u_j is the 2x1 vector of the j^{th} image point coordinates, $[u_j, v_j]^T$, X_j is the 3x1 vector of the j^{th} world point coordinates, $[X_j, Y_j, Z_j]^T$, p^i is a set of parameters defining the model of the i^{th} camera, and F defines the form of the model. This model allows each image from each of the N cameras in the array to be projected onto k focal planes. I_{FPki} denotes the image from camera i aligned on the k^{th} focal plane. The resulting, refocused SA image, I_{SAk}, may be generated by averaging each of these images over the number of cameras in the array

$$I_{SAk} = \frac{1}{N} \sum I_{FPki}, \tag{4.3}$$

where I_{SAk} is the image from camera i aligned on the k^{th} focal plane [8]. Combining images using this averaging technique is known as additive refocusing. A variant of the additive SA algorithm that can enhance the signal-to-noise ratio for well calibrated images is given by the multiplicative refocusing algorithm

$$I_{SAk} = \prod_{i=1}^{n} [(I_{FPki})^n], \tag{4.4}$$

where n is an exponent between 0 and 1. This allows for enhancement of the signal-to-noise ratio without letting any camera with an occluded view of an object prevent that object from being refocused. This is because a small number raised to an exponent between 0 and 1 is non-zero. For ordinary light field SA refocusing, it has been determined that n in the range of $\frac{1}{5} \leq n \leq \frac{1}{3}$ works best.

4.3.2 Synthetic Aperture Feature Extraction

The SA output focal stack images can be filtered to physically locate features that are small relative to the field of view. However, this task becomes more difficult for features that are large relative to the field of view. Here, the Synthetic Aperture Feature Extraction (SAFE) technique has been applied to measure 3D features. First, raw images from each of the array cameras are preprocessed. Blobs are detected and converted to white pixels, while the rest of the image is converted to black. These binary images are then refocused. For blobs that can be approximated as spheres, 3D centroids and radii can then be extracted after post-processing the focal image stack. This process can be repeated over time while tracking particle motion. As a result, 3D spatial, size, and velocity data distributions can be calculated as functions of time to better understand the flow dynamics and characteristics. The SAFE technique has been verified using both simulations and experimentally using a flow of spherical soap bubbles in air, as described in Chapter 2.

4.3.3 Raw Image Preprocessing

During the preprocessing step, the goal is to perform as many reliable droplet detections as possible. To achieve this, the robust maximally stable extremal regions (MSER) blob detection algorithm is used [41]. Figure 4-10 (reproduced from [47]) presents an overview of this method. Essentially, connected components are found in an image as regions whose size remains relatively constant during threshold variation. Detected features do not need to be spherical, which is advantageous in spray analysis because most droplets are asymmetric in shape, even if their radii are small. The target blob minimum and maximum areas can be specified as inputs to the algorithm. Setting a minimum area allows pixels that constitute noise to be filtered, while an upper size bound eliminates undesirable larger features, such as ligaments or background

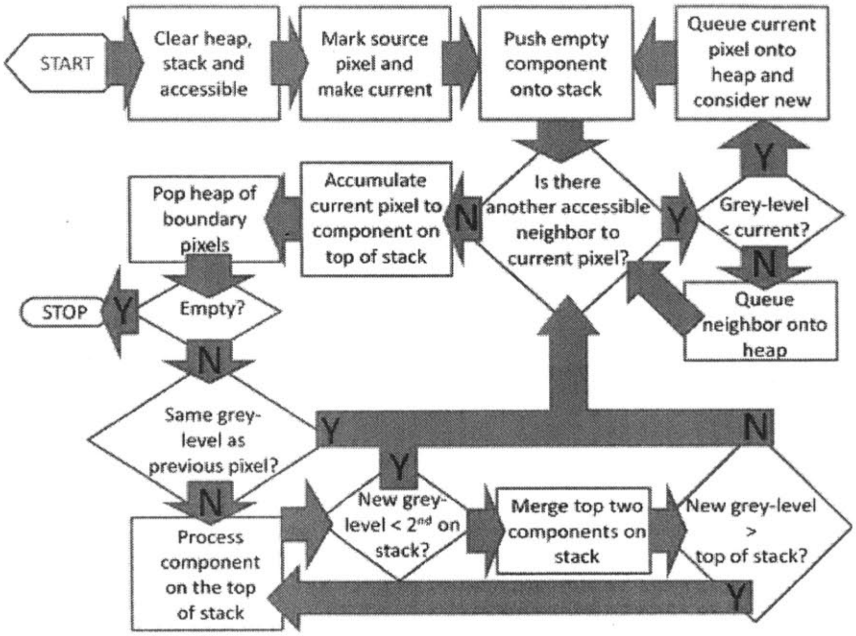

Figure 4-10: Maximally Stable Extremal Regions (MSER) algorithm state graph (reproduced from [47]).

shadows that are large relative to the field of view. Removing regions with estimated eccentricities (by approximating them as ellipses) above a desired threshold can also help eliminate ligaments from the detected blob list. In practice, these bounds are set by manually examining images. All of the pixels belonging to an MSER are then converted to white while the rest of the image is made black.

Figure 4-5 is an example of the nine array camera images recorded by each of the cameras at a single time step (the additional upstream camera image is also shown at the left). The layout of the images corresponds to their relative locations in the camera array when looking into the cameras. In Figure 4-11, MSER features have been detected in each of the array raw images. Both ligaments with beads-on-a-string (see Chapter 3) and free droplets are observable in these photographs. However, by filtering the images, only the individual beads or droplets will be analyzed, ignoring the elongated ligament strands. The images are then binarized by converting all pixels that are not members of any MSERs to black. Only the borders of MSER regions are retained and converted to white pixels. Eliminating interior pixels simplifies cluster

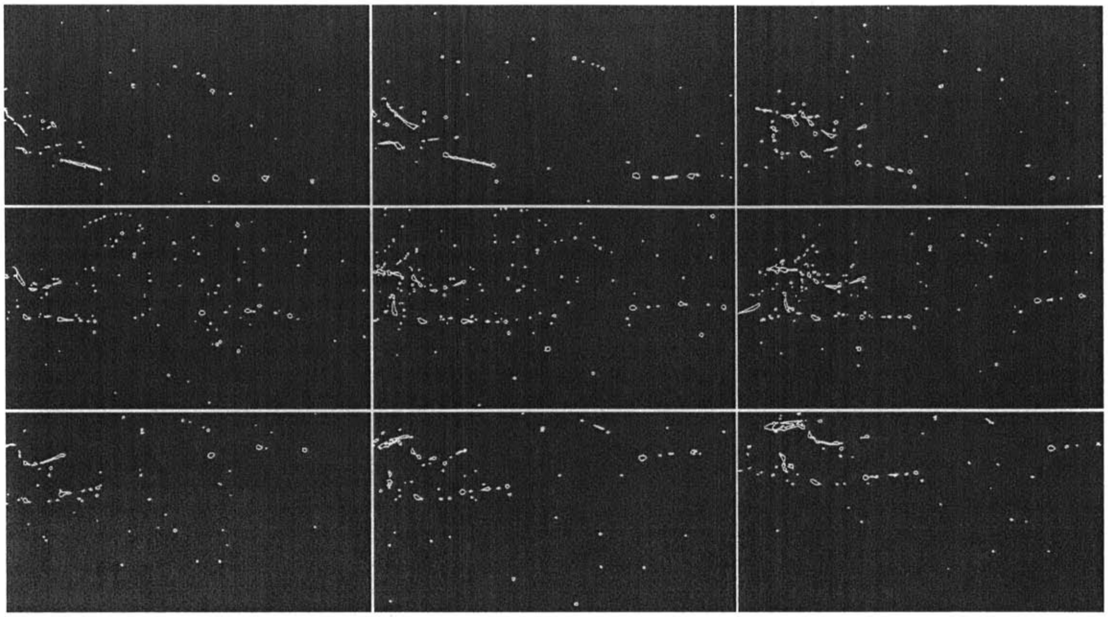

Figure 4-11: Binarized images recorded by each of the nine cameras in the array at the time step corresponding to the array images shown on the right in Figure 4-5.

extraction after refocusing by reducing the potential for feature blur artifact overlap.

4.3.4 Raw Image Refocusing

After preprocessing, each of the array camera images must be transformed and combined at each time step to refocus the volume. Either multiplicative (Eq. 4.4) or additive (Eq. 4.3) refocusing may be employed to combine the images. If the same features are detectable in all of the camera images, then multiplicative refocusing is effective since only the corresponding white pixels (binary value of 1) in each of the preprocessed images will be preserved, while all other pixels will be converted to black (binary value of 0). This is because binary preprocessed images are being multiplied together. The refocused stack can be thresholded to estimate the true location and size of particles in 3D. Multiplicative refocusing of the preprocessed binarized images can lead to the elimination of objects detected in at least one but not all photographs. Thus, a more reliable approach is to use additive refocusing with thresholding to catch all of the possible features from the preprocessed images. While

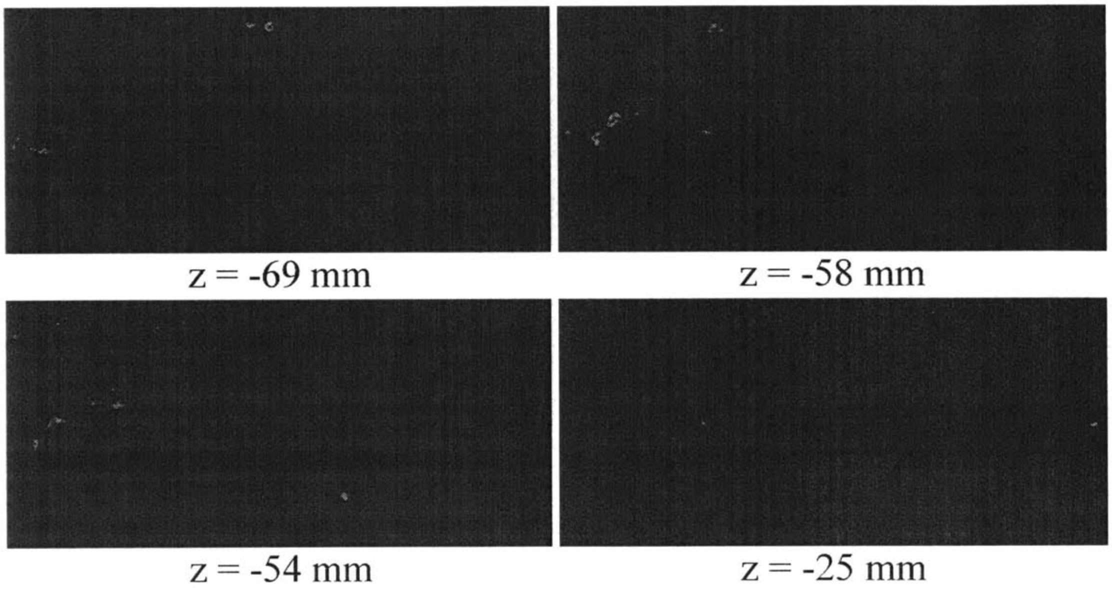
z = -69 mm
z = -58 mm
z = -54 mm
z = -25 mm

Figure 4-12: Refocused depth slices corresponding to the array images shown in Figures 4-5 and 4-11. Here, the additive refocusing method is used (Eq. 4.3) to construct the focal stack. Then, a threshold of 100 (out of a maximum possible value of 255) is applied in order to retain only the particles that are actually located at each depth.

additive refocusing could result in more erroneous detections than the multiplicative approach, the proper thresholding can yield highly reliable particle localizations.

Figure 4-12 presents four depth slices from the focal stack obtained by refocusing the binarized images in Figure 4-11. Additive refocusing is used with a threshold of 100 out of a maximum possible value of 255. Negative z depth values correspond to points in between the reference plane at z=0 and the camera array, while $+z$ depths are behind the reference plane. The reference plane depth is set during calibration and is arbitrary. Using the SAFE method, only features actually located at each depth plane remain in the focal stack. Blur artifacts are eliminated. Refocusing is performed in the z direction, without any rotation or translation.

4.3.5 3D Cluster Extraction

After refocusing, clusters must be extracted from the focal stack. Cluster size lower and upper thresholds can be set to filter noise or processing artifacts (e.g. blur artifacts that have erroneously merged into a single, larger cluster). Figure 4-13 presents the raw voxels from the focal stack; clockwise from the top: isometric, $x - z$, and $x - y$ views, respectively, are shown. The clusters are elongated and extend in different directions due to the blur pattern from the cameras, as expected. The deformation is a function of the focal length and distance of the particle from the z-axis. The geometric centroids of these clusters are the estimated true centroids of the droplets. Droplet radii are estimated from the $x - y$ planar area of the depth slice at the z centroid by assuming that this area corresponds to that of a circle. Figures 4-14 and 4-15 present the isometric and planar views, respectively, of the reconstructed scene corresponding to the raw clusters shown in Figure 4-13. This cluster extraction process is then repeated for each frame. Droplets are then tracked in 3D+T using MATLAB software developed by Blair and Dufresne [12]. Lagrangian velocities and accelerations are calculated for each particle by differentiating polynomial fits to centroids over time.

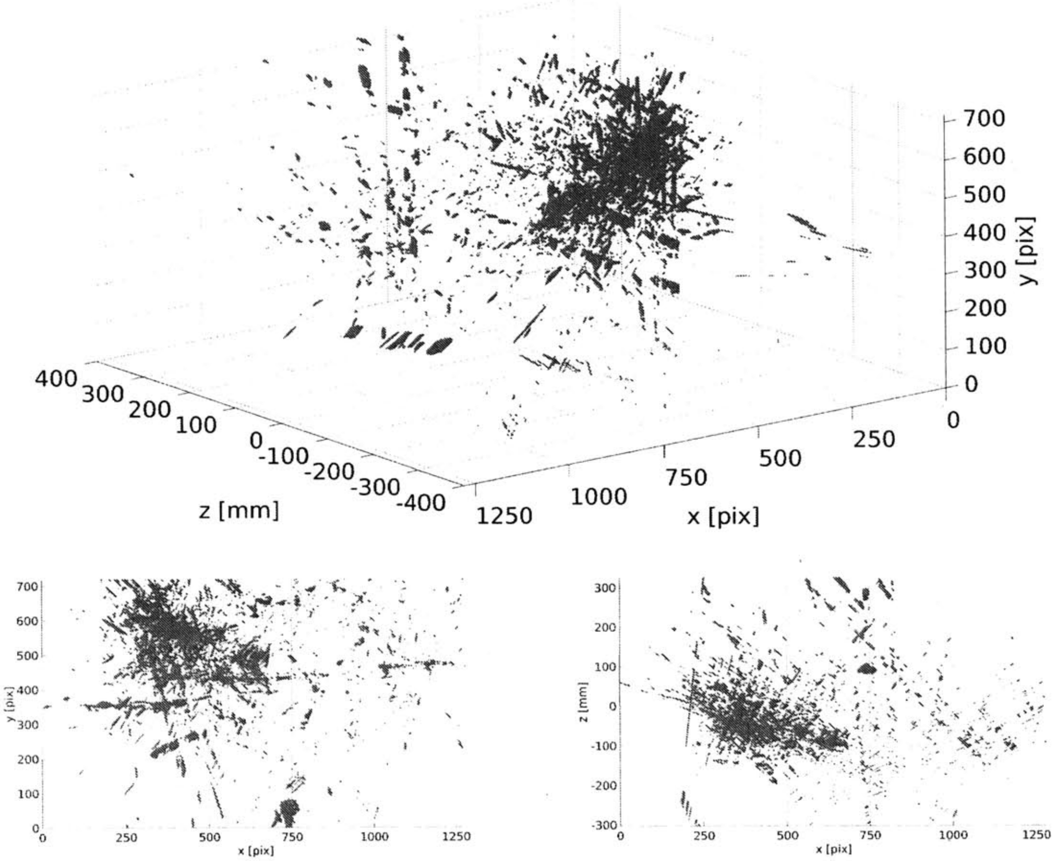

Figure 4-13: Raw SAFE method focal stack processing corresponding to the images recorded at the instant shown in 4-5. x and y dimensions are reported in pixels, and z includes the depth slices in mm. Clockwise from top: isometric, $x - z$, and $x - y$ views.

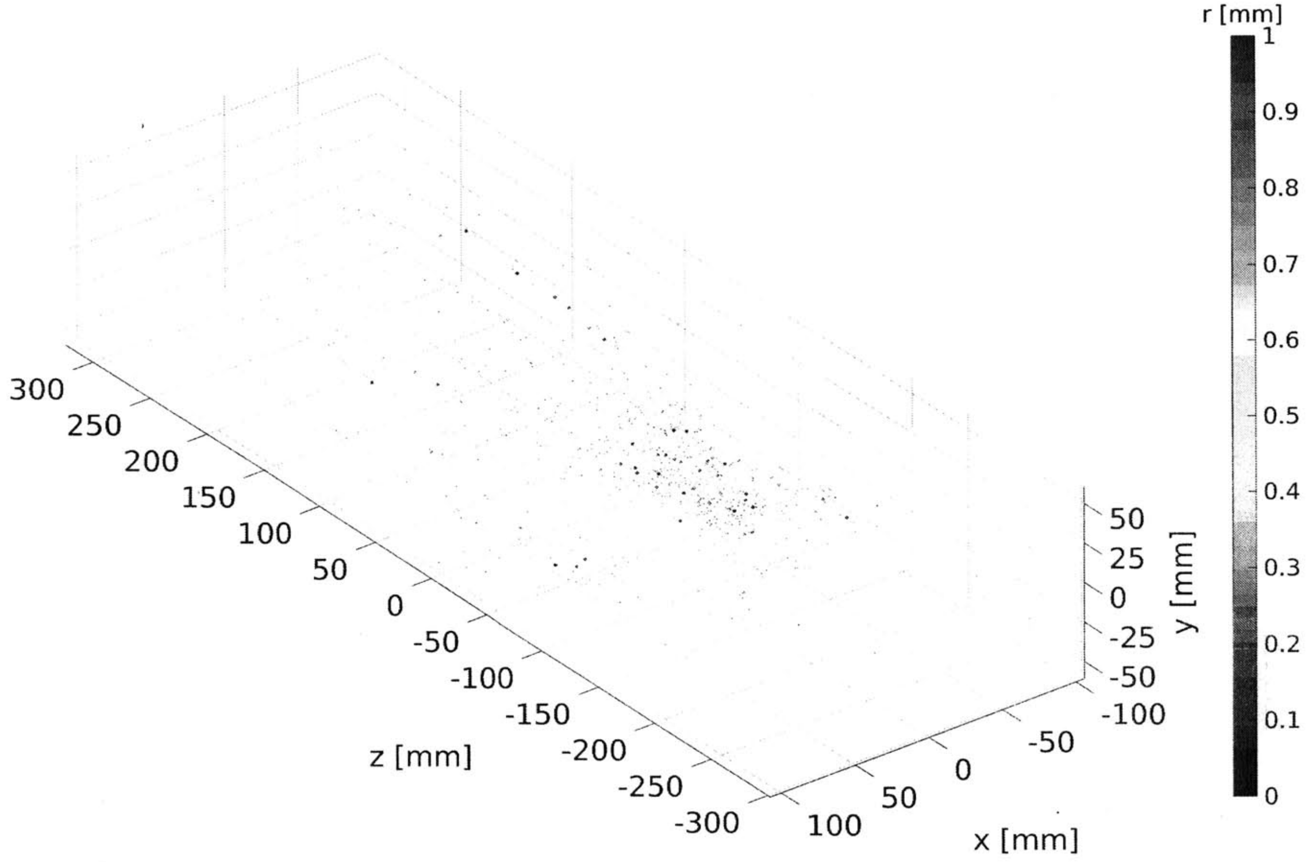

Figure 4-14: Isometric view of reconstructed scene produced by post-processing the raw clusters shown in Figure 4-13. Sphere centroids are calculated as the geometric centers of the raw clusters. Radii are estimated from the $x - y$ plane area (assuming a circular shape) of the raw clusters at the z centroid depth slice of each one.

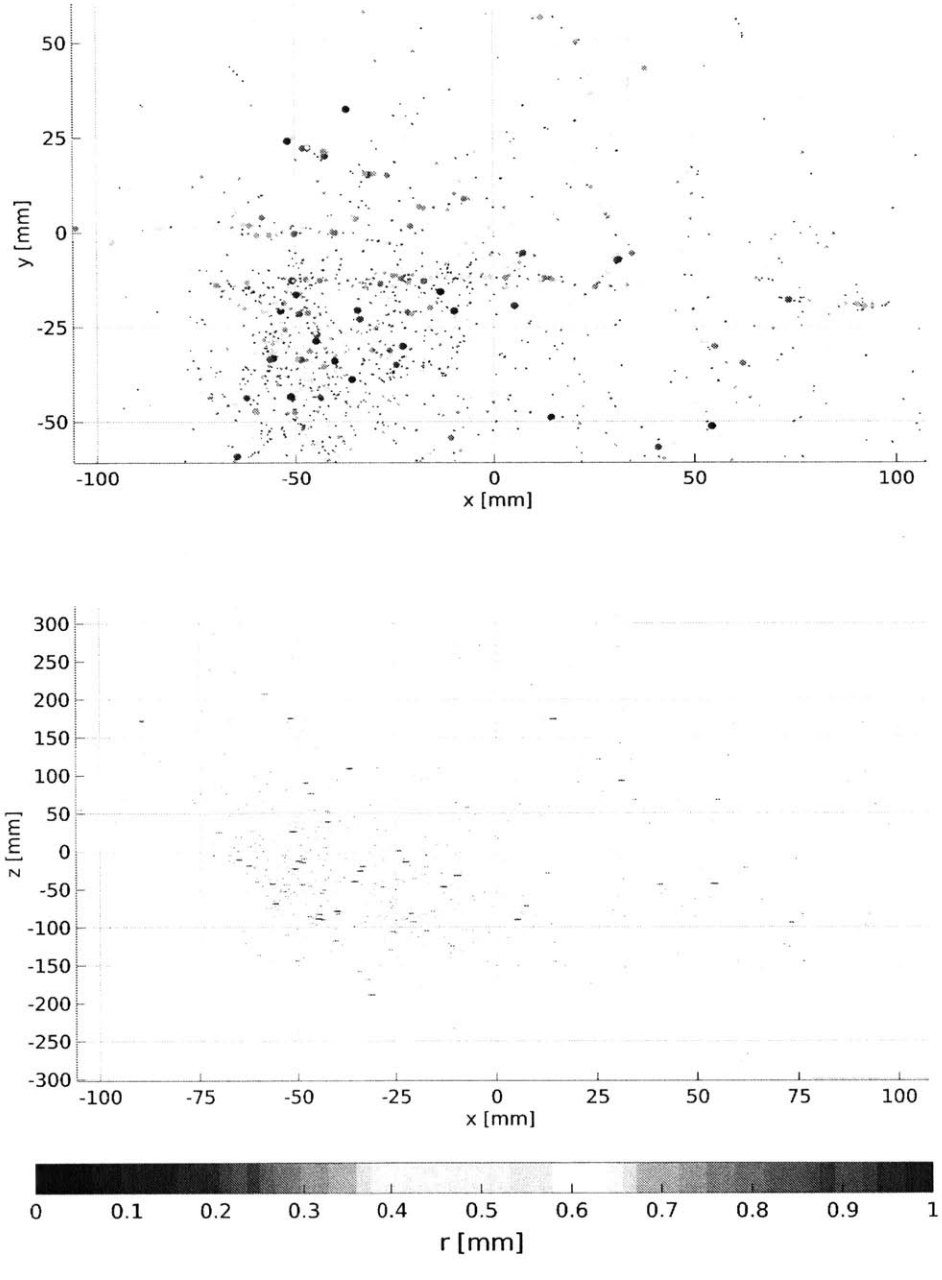

Figure 4-15: $x - y$ (top) and $x - z$ (bottom) views of the reconstructed scene, corresponding to the isometric view presented in Figure 4-14. (In the $x - z$ view, the droplets appear stretched in the x direction because the aspect ratio has been adjusted so that the droplets can be seen more easily. However, all blobs shown are actually spheres, as seen in the $x - y$ view.)

Trial Index	N_d	V_{tot} [mL]	t_s [msec]	t_R [msec]	d_{mouth} [cm]
1	37163	7.769	239.410	128.961	1.32
2	85259	25.756	304.989	160.966	1.79
3	633	0.249	312.833	206.464	2.01
4	782	0.265	368.372	169.438	1.69
5	5143	1.928	336.680	178.224	1.65
6	216466	113.357	298.400	157.829	1.43
7	927	0.261	314.402	222.780	2.26
8	2175	1.205	384.060	131.158	1.55
9	1892	0.572	391.905	165.987	2.21

Table 4.3: Sneeze measurement results for each trial. N_d is the total number of unique droplets detected throughout the duration of the sneeze, t_s. The sneeze is considered to begin the instant that liquid is first observed exiting the mouth and lasts until most of the particles have moved beyond the field of view of the array cameras and the only ones remaining are settling. V_{tot} is the total volume of droplets detected. t_R is the release time, when the last bit of liquid is seen exiting the mouth. d_{mouth} is the diameter of the open mouth at t_R.

4.4 Results and Discussion

4.4.1 3D Sneeze Spray Reconstruction

Figures 4-16 through 4-18 present sample raw images from the center array camera as well as full 3D reconstructions of every droplet in the sneeze throughout the entire sneeze duration (in some plots, droplets from only a fraction of the total number of frames are displayed so that it is easier to see the overall structure of the spray). Figures 4-30 through 4-38 display the sneeze cloud isometric views in greater detail, and Figures 4-39 through 4-47 show $x-y$ and $x-z$ views of the same sneeze cloud. In all of these figures, the overall mean velocity vector direction is indicated by a gray arrow drawn at the geometric centroid of all droplets for the entire sneeze duration (the length of the arrow is arbitrary.).

There is large variation in the number of unique droplets detected, N_d, per trial (see Table 4.3). The total volume of liquid emitted, V_{tot}, is proportional to N_d. In the nine trials in this study, N_d is generally inversely proportional to the average distance of the head from the world origin, at which the array cameras are aimed (see the table in Figure 4-3). This distance is not precisely controlled because the

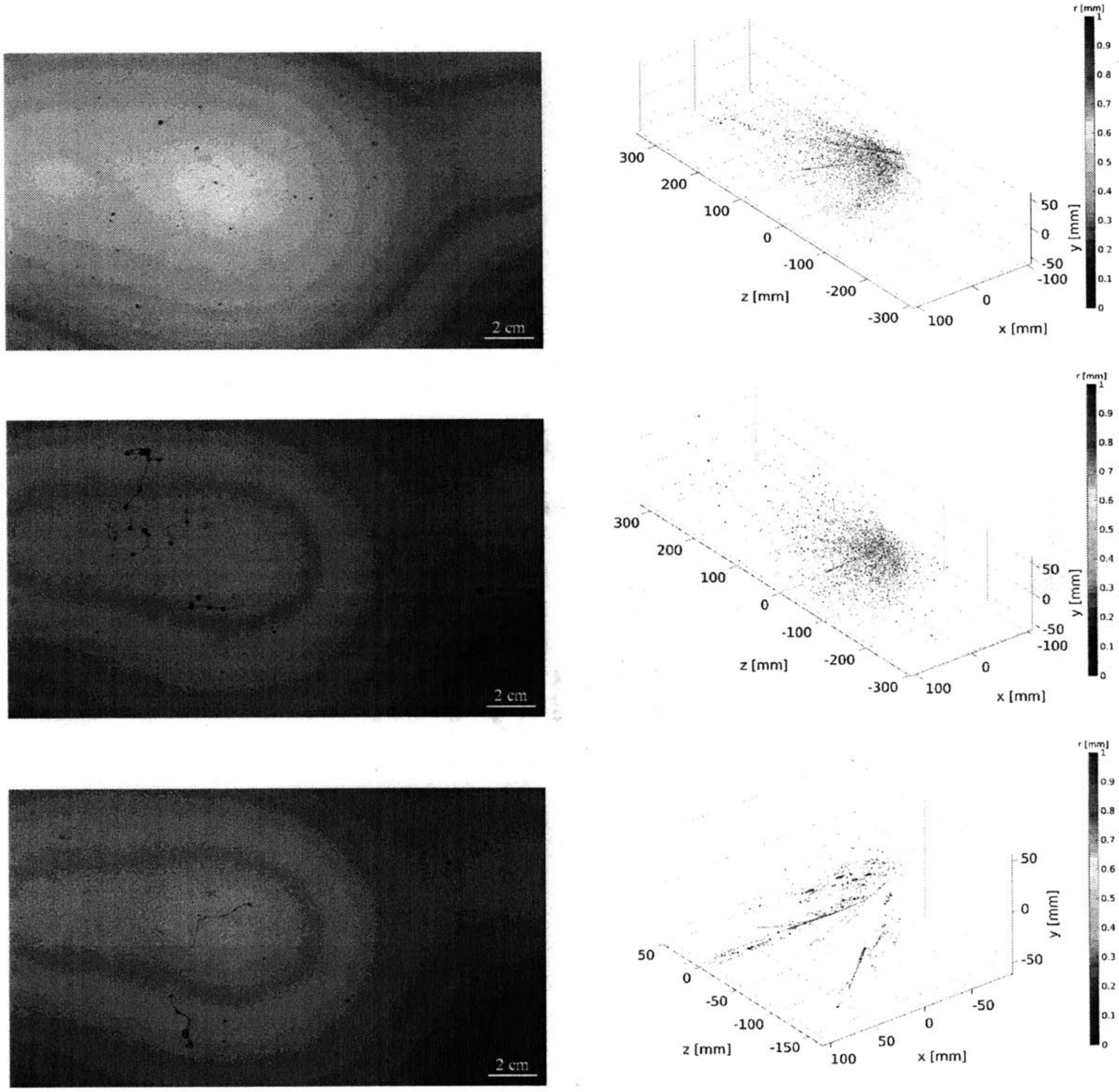

Figure 4-16: (Left Column) Raw example images of the sneeze recorded by the central array camera for Trials 1-3. (Right Column) Isometric views of 3D reconstructed sneeze clouds for the corresponding trials.

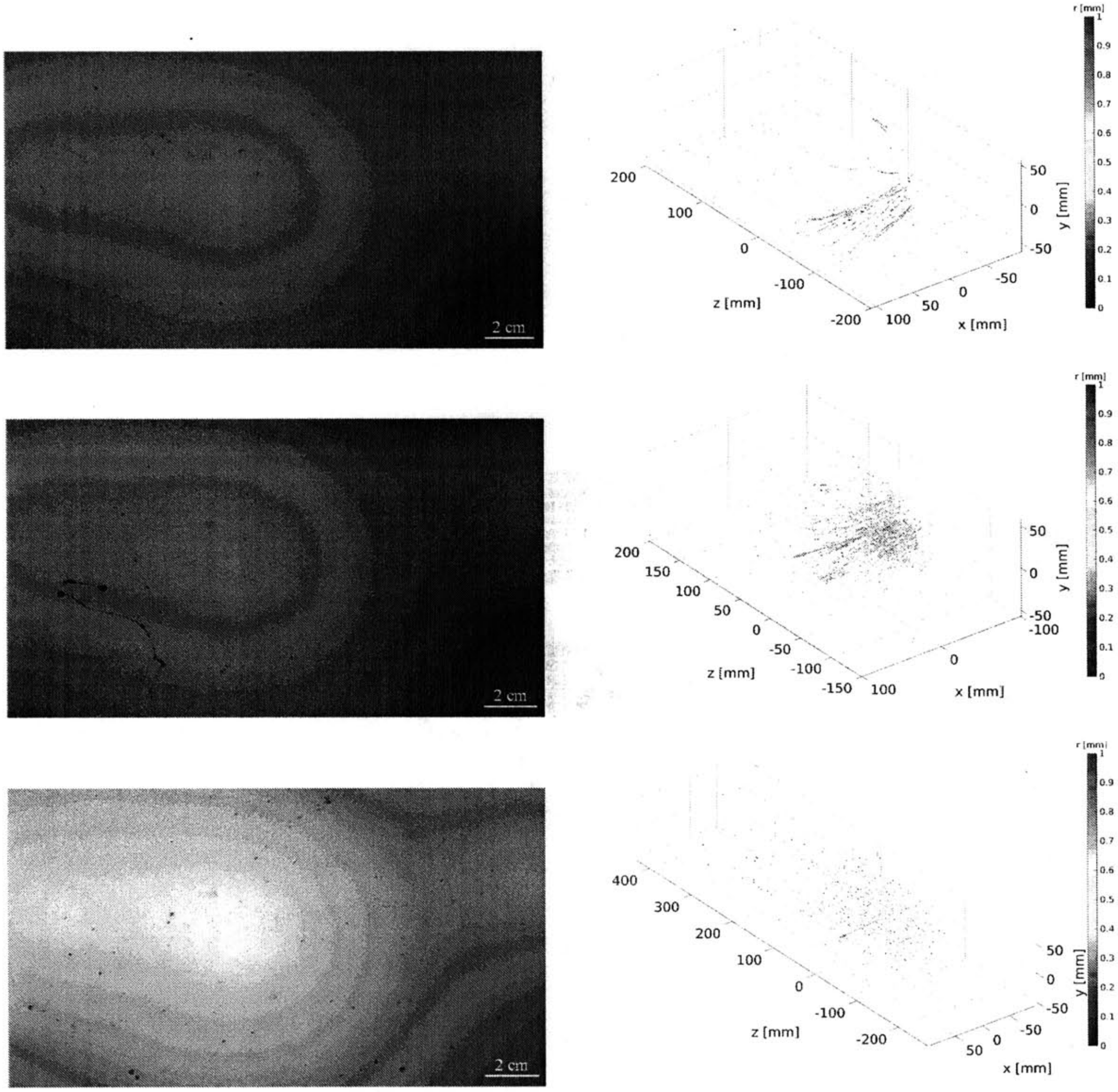

Figure 4-17: (Left Column) Raw example images of the sneeze recorded by the central array camera for Trials 4-6. (Right Column) Isometric views of 3D reconstructed sneeze clouds for the corresponding trials.

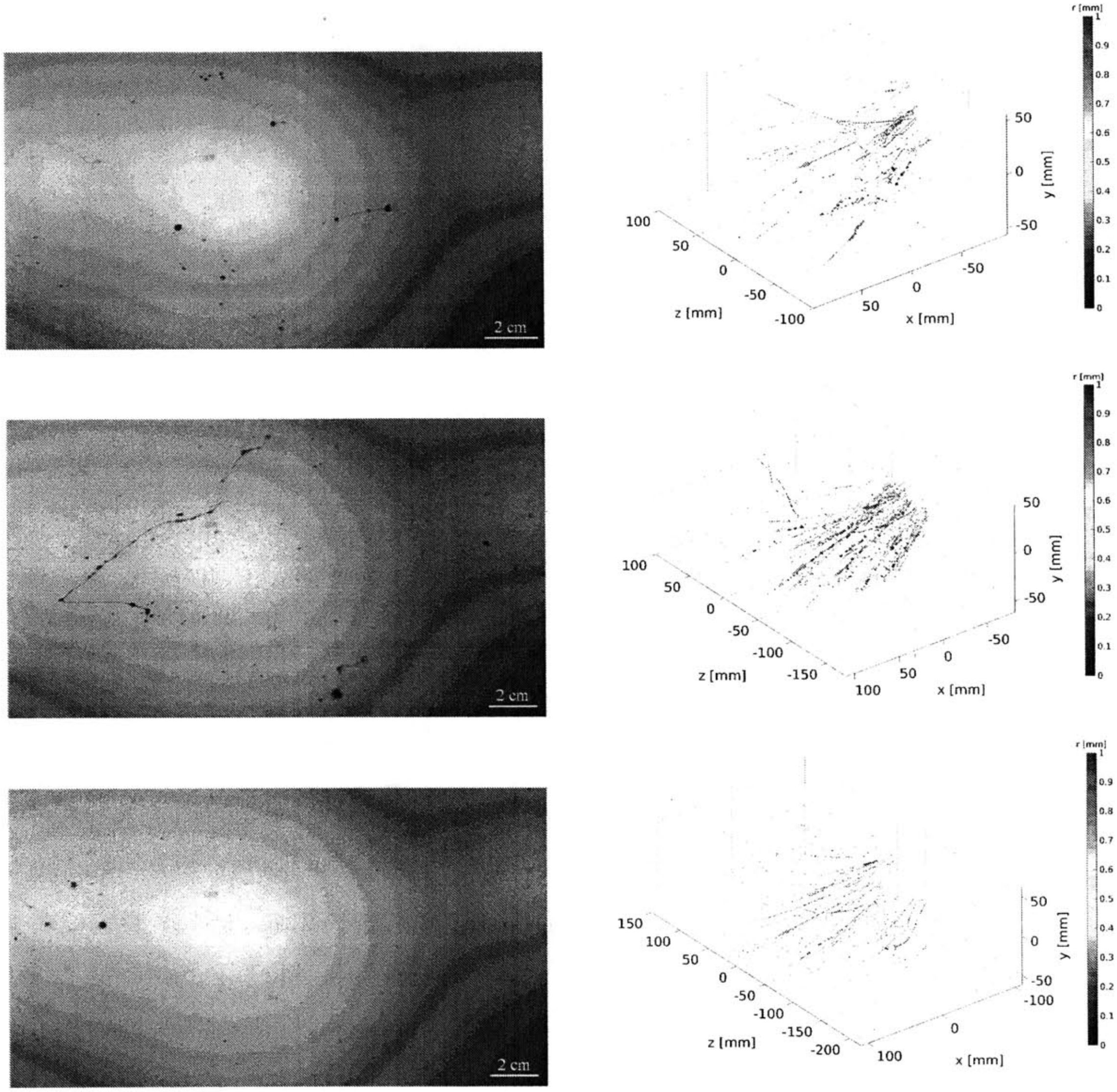

Figure 4-18: (Left Column) Raw example images of the sneeze recorded by the central array camera for Trials 7-9. (Right Column) Isometric views of 3D reconstructed sneeze clouds for the corresponding trials.

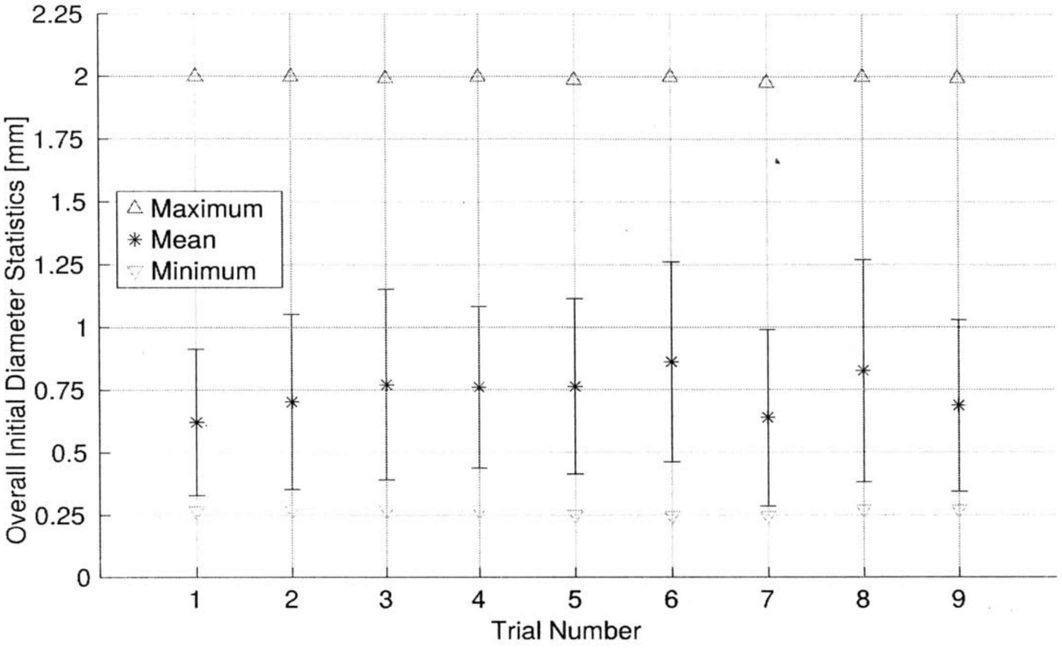

Figure 4-19: Overall minimum, mean, and maximum initial droplet diameter for each trial. The blue vertical line segments indicate one standard deviation above and below the mean. The smallest diameters (both 0.247 mm) are observed in Trials 6 and 7. Trial 6 featured droplets with the largest observed diameter of 1.999 mm, but the upper diameter limit for all trials is close to 2 mm.

head is not constrained in order to simulate natural sneeze conditions. Since these 3D reconstructions contain droplet tracks, they feature droplet motion from all stages of the sneeze, including droplets that settle, primarily falling downward slowly near the end of the sneeze. Changes in head position, angle, and mean liquid ejection angle as a function of time also influence the appearance of the overall 3D reconstruction.

Despite the variation in N_d, all of the trials feature an expanding droplet spray cloud due to entrainment, as is expected from turbulent jet theory [52]. The overlap of normalized distributions of droplet location, size, and velocity components presented in the following sections also demonstrate the universality of the sneeze across different trials.

4.4.2 Droplet Sizes

Figure 4-19 presents the minimum, mean, standard deviation, and maximum droplet diameters measured in each of the trials, based on the initial size of each measured droplet. Diameters are calculated as the projected area diameter, defined as

$$d = \left(\frac{4A}{\pi}\right)^{1/2}, \tag{4.5}$$

where A is the droplet's projected area [24]. Despite the wide variation in the number of droplets across trials (Table 4.3) the average measured diameters agree. In Figure 4-21, histograms of mean initial droplet diameters are shown at the left, while probability density functions (pdfs) are plotted on the right. These are the diameters of each droplet as measured in the first frame in which that droplet is detected during its trajectory. Sneeze droplet diameter counts from Duguid [21] are also shown in the plot on the left and are within the range of the present investigation's results. Figure 4-20 shows the full droplet diameter histogram from Duguid [21] for a single sneeze event. In Duguid's study, droplet diameters are measured from stain marks found on celluloid slides exposed a few inches in front of the mouth. In the current investigation, the droplet sizes that are measured are on the right tail of Duguid's distribution. It would be possible to image and reconstruct the smaller droplets with the current setup and the SAFE method by zooming in and refocusing the recorded image volume with a finer dz increment. However, the setup used in the present investigation features a larger field of view in order to reconstruct the sneeze over a greater spatial extent. The pdfs across the nine trials tend to match, with the greatest variance surrounding the peak normalized diameter. In Figure 4-22, all sorted initial droplet diameters from each trial are shown in the left plot; the right graph displays initial diameters divided by the mean initial diameter for each trial. Droplet indices are also divided by the total number of droplets detected in each trial, N_d (see Table 4.3). Normalized initial droplet diameters tend to match, except for the largest droplets at the right end of the normalized plot.

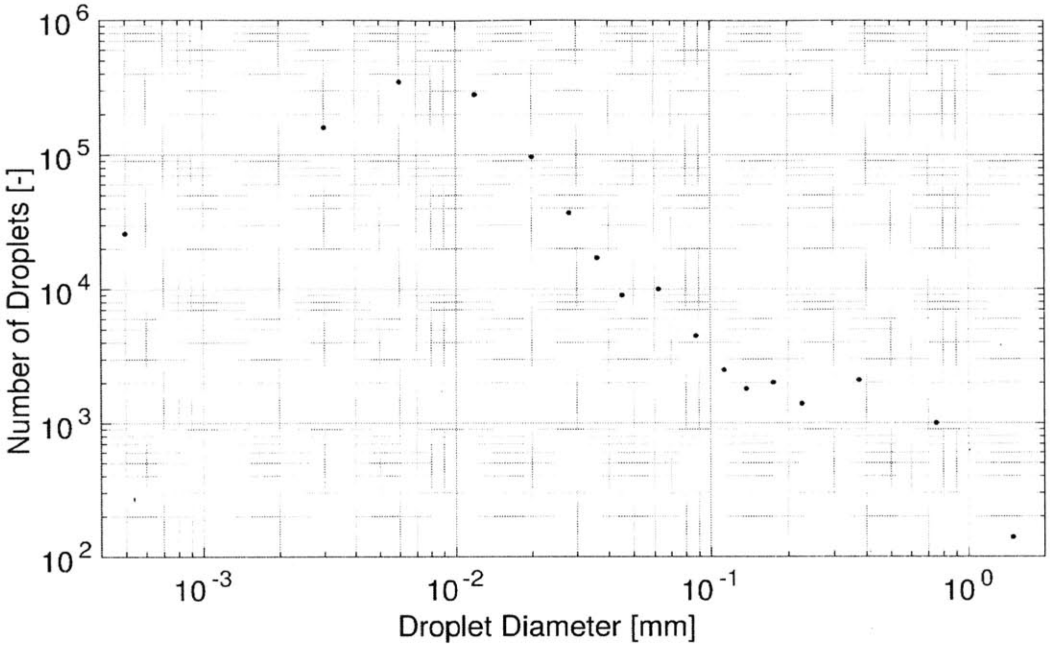

Figure 4-20: Sneeze droplet diameter histogram, produced from the data for a single sneeze provided by Duguid [21] in Table 3, column 1.

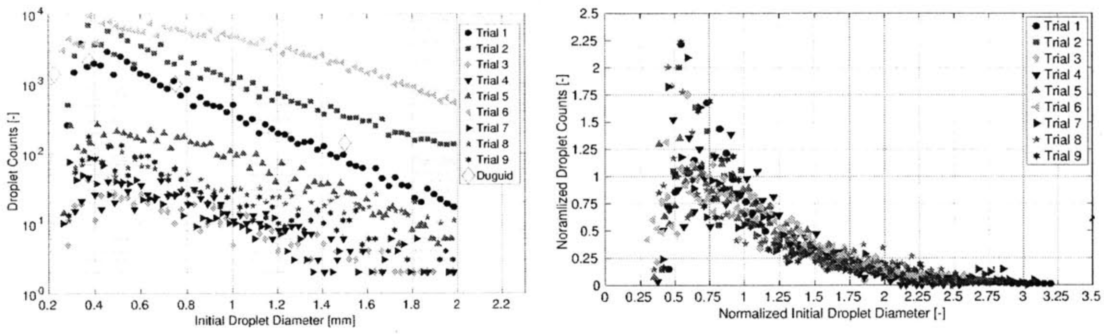

Figure 4-21: (Left) Overall initial droplet diameter histograms. The enlarged black diamonds refer to sneeze data from Duguid [21] (Figure 4-20). (Right) Overall initial droplet diameter probability density functions (pdfs).

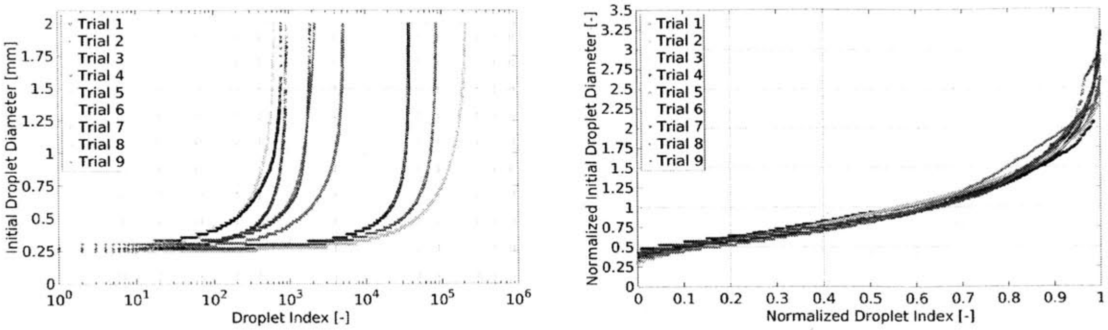

Figure 4-22: (Left) Initial diameter of every droplet in the first frame in which it is detected. The diameters are sorted in order of increasing value. (Right) Sorted initial droplet diameters divided by the mean initial diameter for each trial. The droplet indices are divided by the total number of unique droplets for each trial, N_d (see Table 4.3).

4.4.3 Droplet Locations

Figures 4-23 and 4-24 present probability density functions (pdf) of 3D droplet locations throughout the entire duration of the sneeze. Figure 4-23 shows the $x - y$ pdf averaged over the z dimension. These pdfs are very similar and relatively symmetric about the line y=0. The pdfs in the $x - z$ dimension (averaged over y) are presented in Figure 4-24 demonstrate significant variation. This is likely partially due to greater variation in the angle of the sneezer's head about the vertical y axis (yaw). In addition, based on the SAFE method simulations in Chapter 2, the error in z coordinate reconstruction is generally greater than that in x and y. Error in the z coordinate reconstruction would result in greater error in the z velocity component. §4.4.4 presents similar 3D histograms for the velocity magnitude of the sneeze throughout the entire duration, along with the overall mean velocity vector. Symmetry is generally observed in Figure 4-24 about the axis of the mean velocity vector. The maximum extent of the sneeze in the z direction is also generally greater than or equal to that in y. As expected from turbulent free shear jet theory [52], the sneeze cloud spreads due to entrainment in both the y and z dimensions as it progresses in the downstream direction. More droplets are also observed farther upstream.

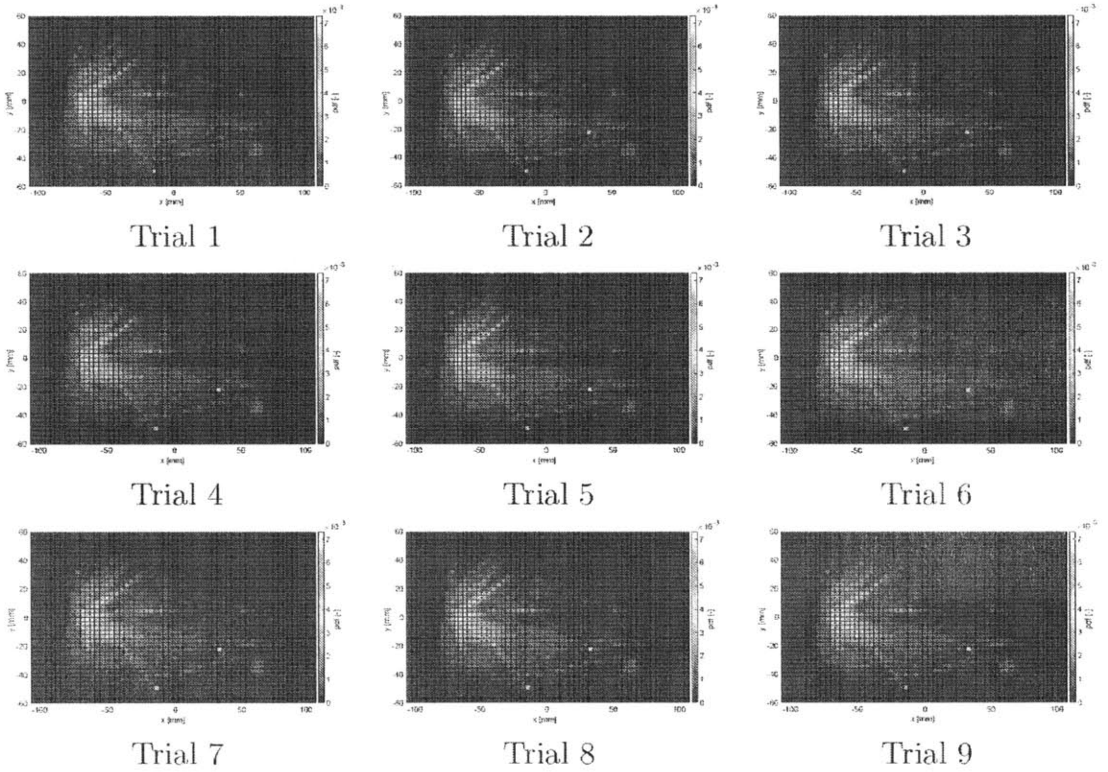

Trial 1 Trial 2 Trial 3

Trial 4 Trial 5 Trial 6

Trial 7 Trial 8 Trial 9

Figure 4-23: $x - y$ droplet 2D spatial probability density function averaged over the z dimension. All droplets present at every time step are counted.

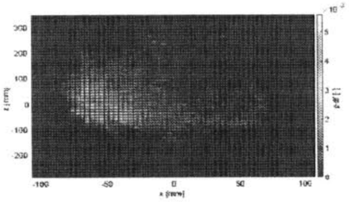

Trial 1

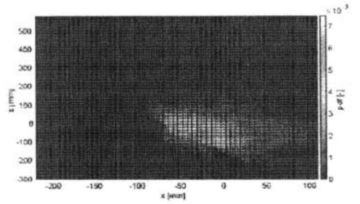

Trial 2

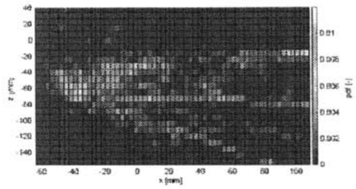

Trial 3

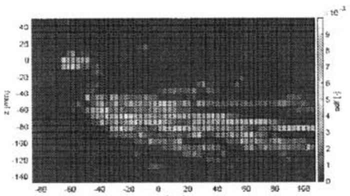

Trial 4

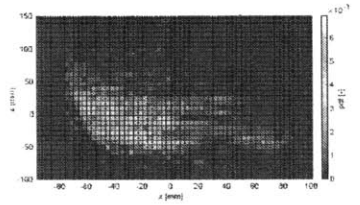

Trial 5

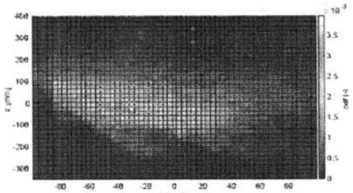

Trial 6

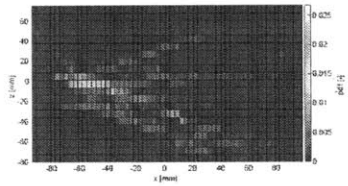

Trial 7

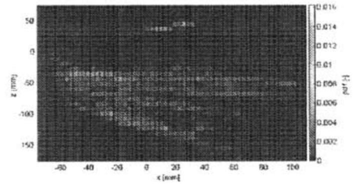

Trial 8

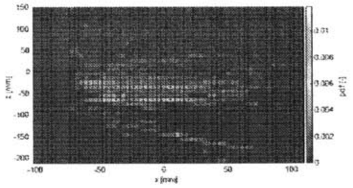

Trial 9

Figure 4-24: $x - z$ droplet 2D spatial probability density function averaged over the y dimension. All droplets present at every time step are counted.

Trial Index	$u_{L,mean}$	$v_{L,mean}$	$w_{L,mean}$	$\|\|U_{L,mean}\|\|$
1	1.21	-0.11	1.21	3.53
2	0.99	-0.12	0.40	3.09
3	1.37	-0.15	0.48	3.10
4	1.70	-0.03	0.37	2.79
5	1.41	0.02	0.26	2.85
6	1.17	-0.09	0.34	3.14
7	1.09	-0.06	0.07	2.43
8	1.51	-0.14	-0.72	3.08
9	1.64	-0.14	-0.07	3.28
Mean	1.34	-0.09	0.26	3.03
Standard Deviation	0.25	0.06	0.51	0.31

Table 4.4: Mean velocity components magnitudes and overall mean speed, reported in units of m/s.

4.4.4 Droplet Velocities

Table 4.4 lists the components and total magnitude of the mean velocity vector for the initial velocity of every unique droplet throughout the duration of the sneeze. The histograms for each velocity component are shown on the left in Figures 4-25 through 4-27. u_{mean}, v_{mean}, and w_{mean} are the x, y, and z mean velocity components, respectively, for all droplets in the spray for the duration of the sneeze. $||U_{L,mean}||$ is the magnitude of the mean overall velocity vector. Since the sneeze in each trial is aimed predominantly in the $+x$ direction, u_{mean} is positive and the distribution of x velocities is skewed toward positive values. Negative x velocities are observed due to recirculation within the sneeze cloud, as demonstrated by Bourouiba et al. [15]. v_{mean} and w_{mean} are symmetric and have peaks near zero. The mean y velocity is generally slightly negative due to the influence of gravity because the y axis is vertical. The sign of w_{mean} varies depending on the orientation of the head during sneezing. The differing orientation of the head angle about the y axis could explain the greater observed variance in the z velocity component.

The plots at the right in Figures 4-25 through 4-27 show the pdfs of each velocity component. There is generally agreement in normalized velocity component values. Again, the greater variation in z velocity component measurement could be due to the angle of the head during sneezing or possibly error in the droplet z centroid

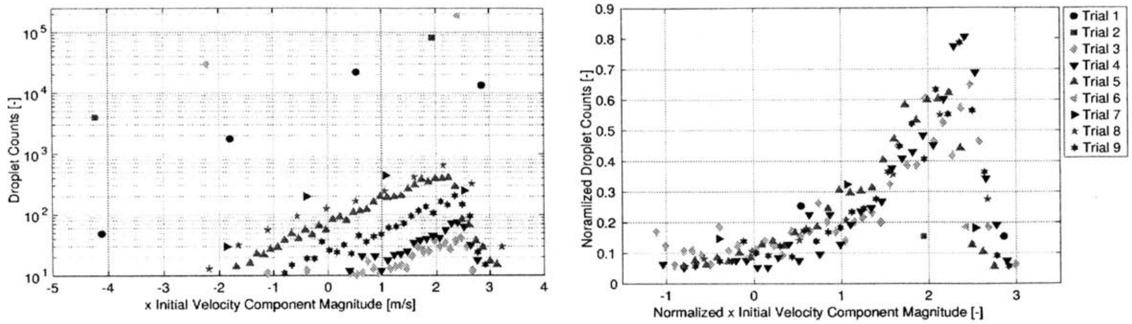

Figure 4-25: (Left) Initial x velocity magnitude histogram. (Right) Initial x velocity component probability density function.

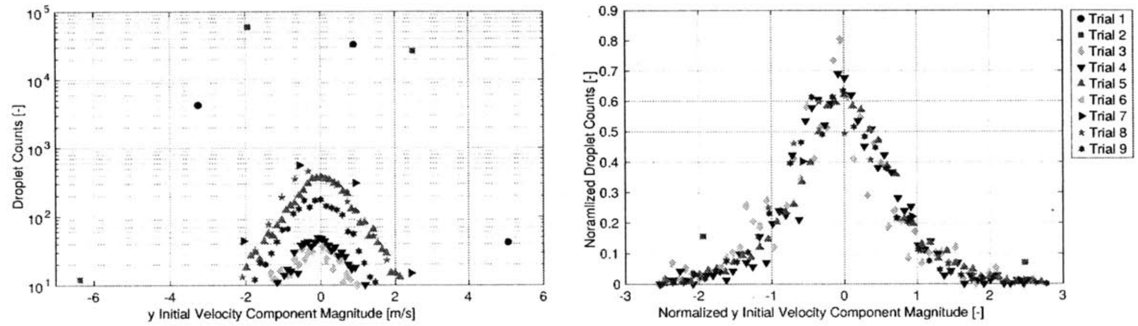

Figure 4-26: (Left) Initial y velocity magnitude histogram. (Right) Initial y velocity component probability density function.

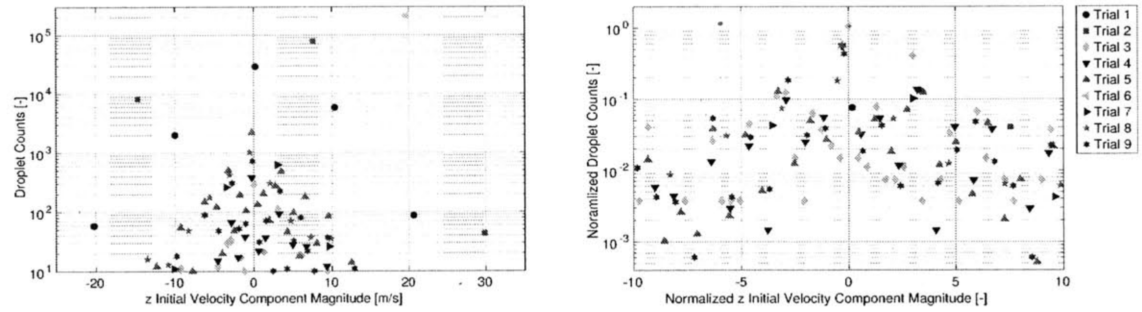

Figure 4-27: (Left) Initial z velocity magnitude histogram. (Right) Initial z velocity component probability density function.

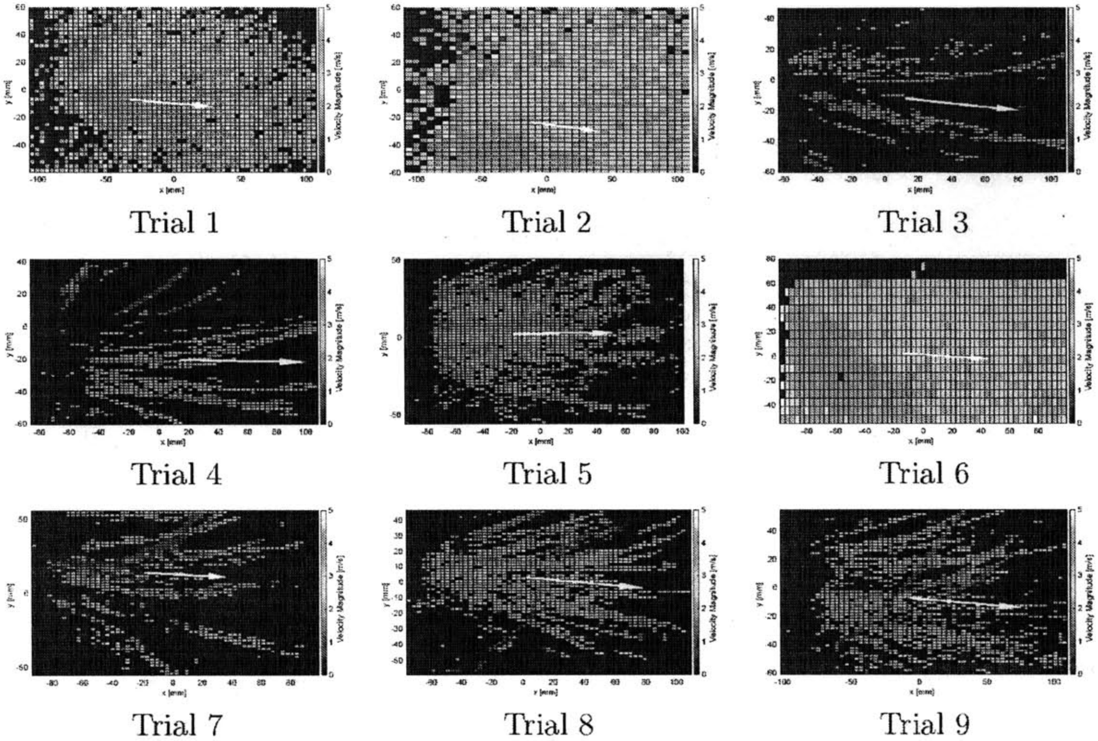

Trial 1 Trial 2 Trial 3

Trial 4 Trial 5 Trial 6

Trial 7 Trial 8 Trial 9

Figure 4-28: Droplet velocity magnitude over $x - y$ bins averaged over the z dimension. All droplets present at every time step are counted. The white arrow is drawn at the centroid of all droplets and points in the direction of the mean velocity vector.

coordinate. As discussed in Chapter 2 §2.4.3, the error in z localization is found to be greater than that in x and y. This may be due to the elongation of objects in z during refocusing, as discussed in §4.3.5.

Figures 4-28 and 4-29 present the 2D droplet velocity magnitude plots over $x - y$ and $x - z$ bins, respectively. The white arrow in each plot is drawn at the geometric centroid of all of the droplets detected during the duration of the sneeze and points in the direction of the mean velocity vector (see Table 4.4). Although droplet speeds higher than 5 m/s are observed in the sneezes, this is the maximum speed displayed in these plots because most of the detected droplets move slower than this speed. While the $x - y$ 2D location pdfs shown in Figure 4-23 are very similar and highly symmetric, significant variation is observed in the $x - y$ velocity plots in Figure 4-28. This is likely due in part to the varying distance of the head from the center of the world coordinates (Figure 4-3). The significantly higher N_d in Trials 1, 2, and 6

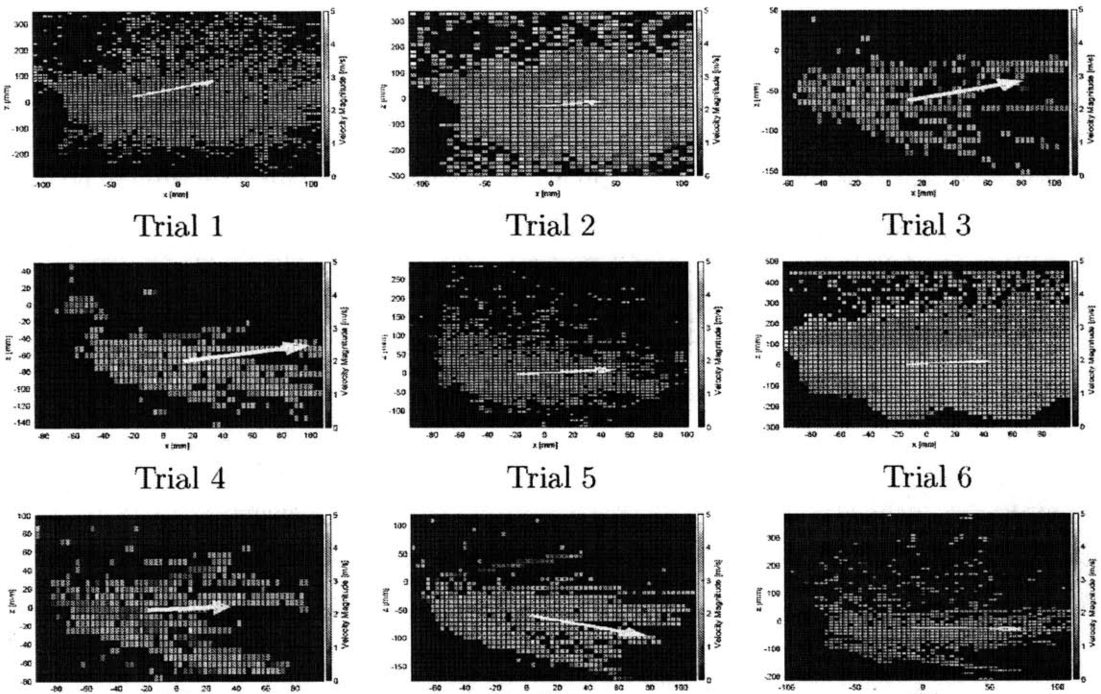

Trial 1 Trial 2 Trial 3

Trial 4 Trial 5 Trial 6

Trial 7 Trial 8 Trial 9

Figure 4-29: Droplet velocity magnitude over $x-z$ bins averaged over the y dimension. All droplets present at every time step are counted. The white arrow is drawn at the centroid of all droplets and points in the direction of the mean velocity vector.

compared to the others (see Table 4.3) tends to create nearly uniform $x - y$ average velocity magnitude fields during the duration of the sneeze. In the other trials, the expected expanding sneeze cloud shape in the $+x$ direction due to entrainment is observed. Similarly, the $x - z$ average velocity magnitude fields during the duration of the sneeze shown in Figure 4-29 are more nearly uniform for Trials 1, 2, and 6, but not for the other trials. The velocity mangitude patterns observed in this figure are similar to those seen in Figure 4-24 for the $x - z$ droplet location pdfs.

4.5 Summary and conclusion

This work presents the first fully three-dimensional experimental investigation of near-field sneeze ejecta close to the exit of the mouth. The novel Synthetic Aperture Feature Extraction (SAFE) method has been successfully applied to reconstruct sneeze flows using an array of high-speed cameras. Droplets are resolved in 3D+T, leading to full scene reconstruction with droplet positions, diameters, and velocities being reported for each droplet over its lifetime. An additional camera that records the motion of the head provides information regarding the head position relative to the array camera field of view and the mouth opening diameter during the course of the sneeze. While the number of detected droplets varies widely across trials, agreement is found in the droplet size and velocity component probability density functions. This is indicative of the universality of sneeze characteristics across trials.

4.6 Acknowledgements

Samantha Hartzell at MIT is acknowledged for her assistance with the experimental setup.

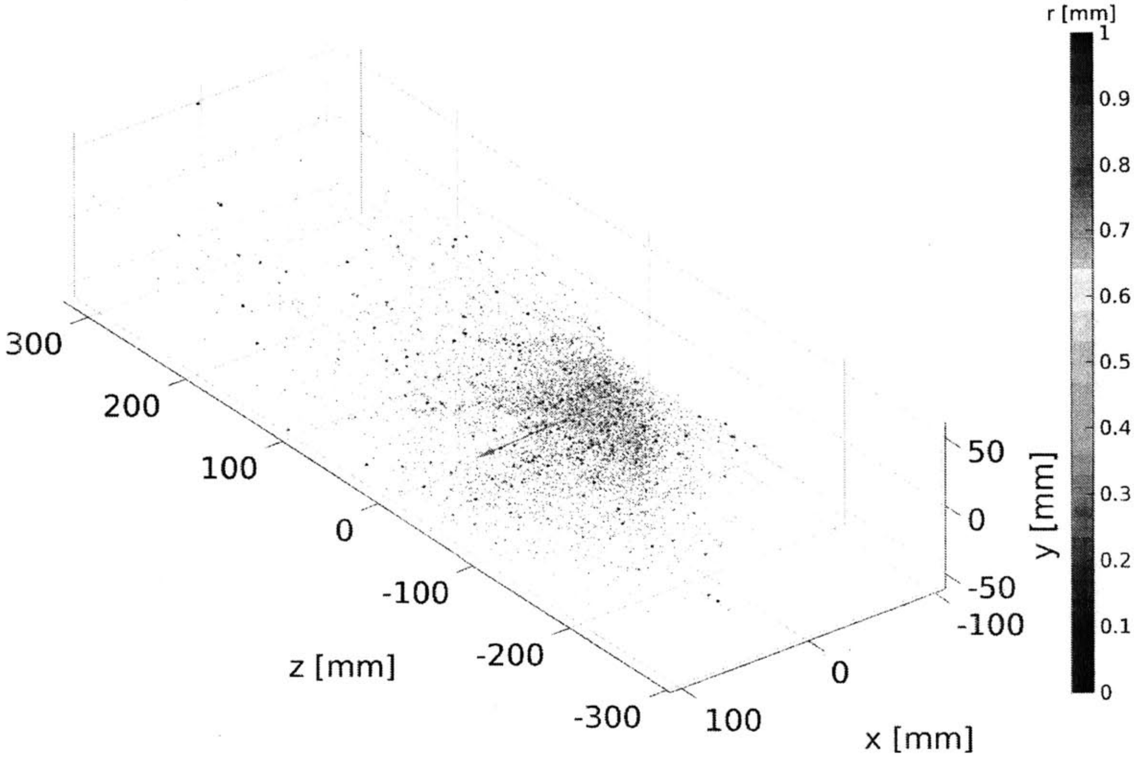

Figure 4-31: Isometric view of 3D sneeze cloud in Trial 2. All droplets detected at every twentieth time step are plotted (therefore droplets shown are not all unique). The gray arrow points in the direction of the overall mean velocity vector of all droplets.

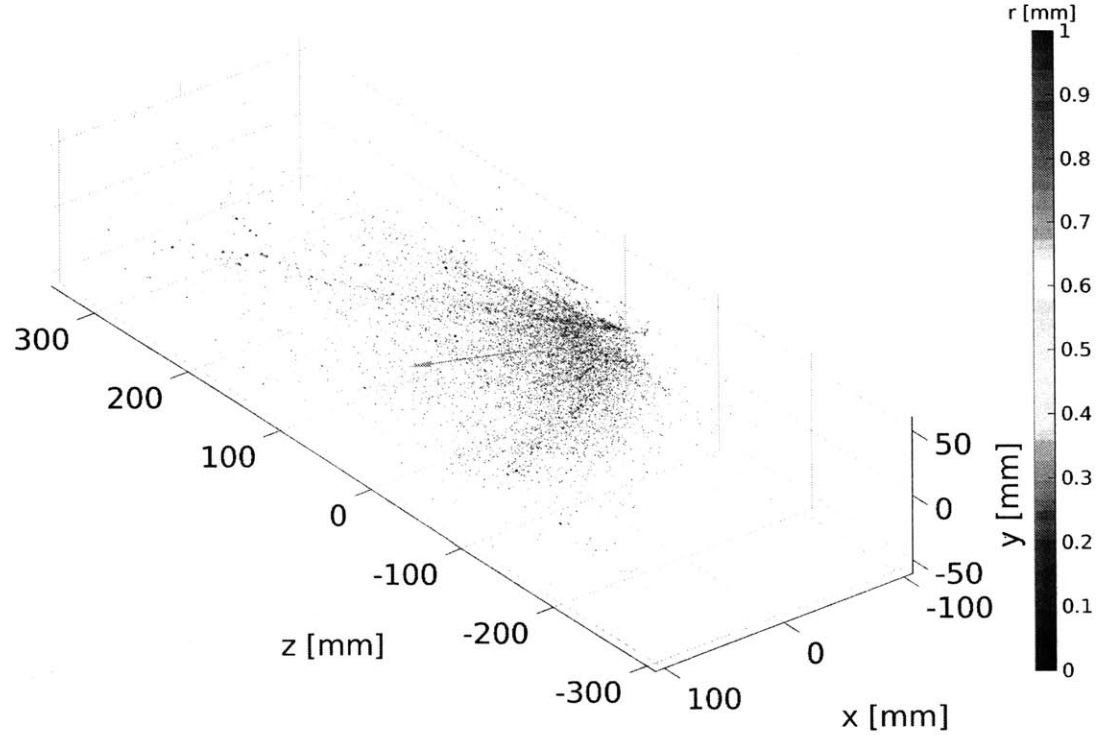

Figure 4-30: Isometric view of 3D sneeze cloud in Trial 1. All droplets detected at every fifth time step are plotted (therefore droplets shown are not all unique). The gray arrow points in the direction of the overall mean velocity vector of all droplets.

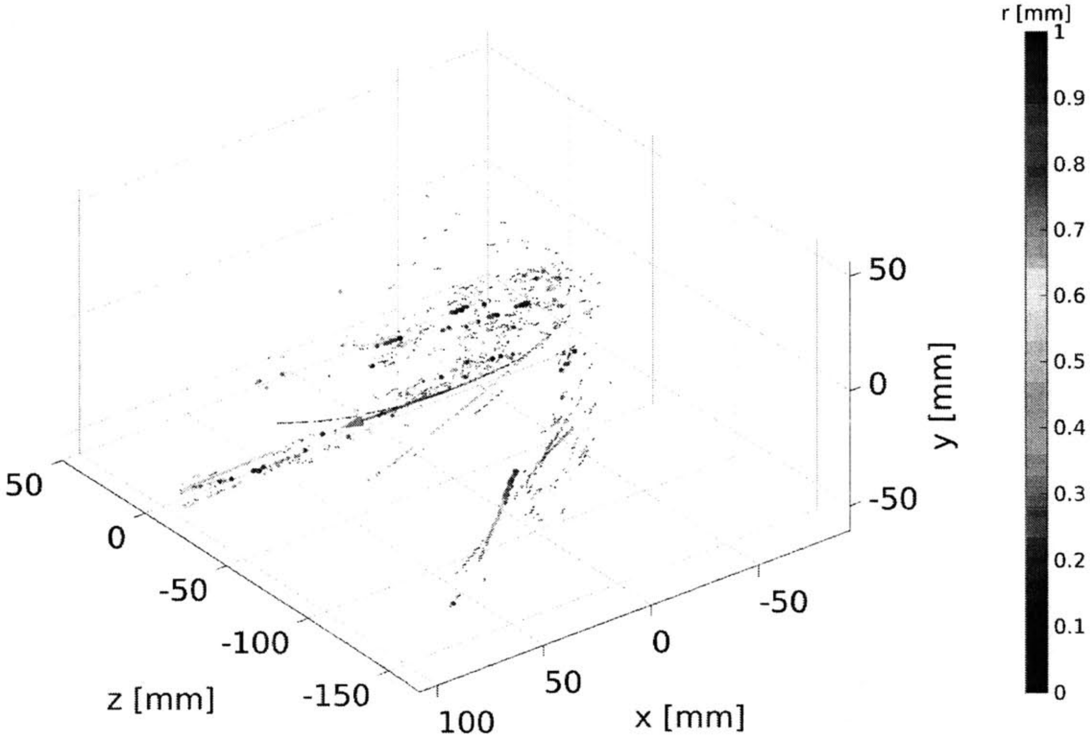

Figure 4-32: Isometric view of 3D sneeze cloud in Trial 3. All droplets detected at every time step are plotted (therefore droplets shown are not all unique). The gray arrow points in the direction of the overall mean velocity vector of all droplets.

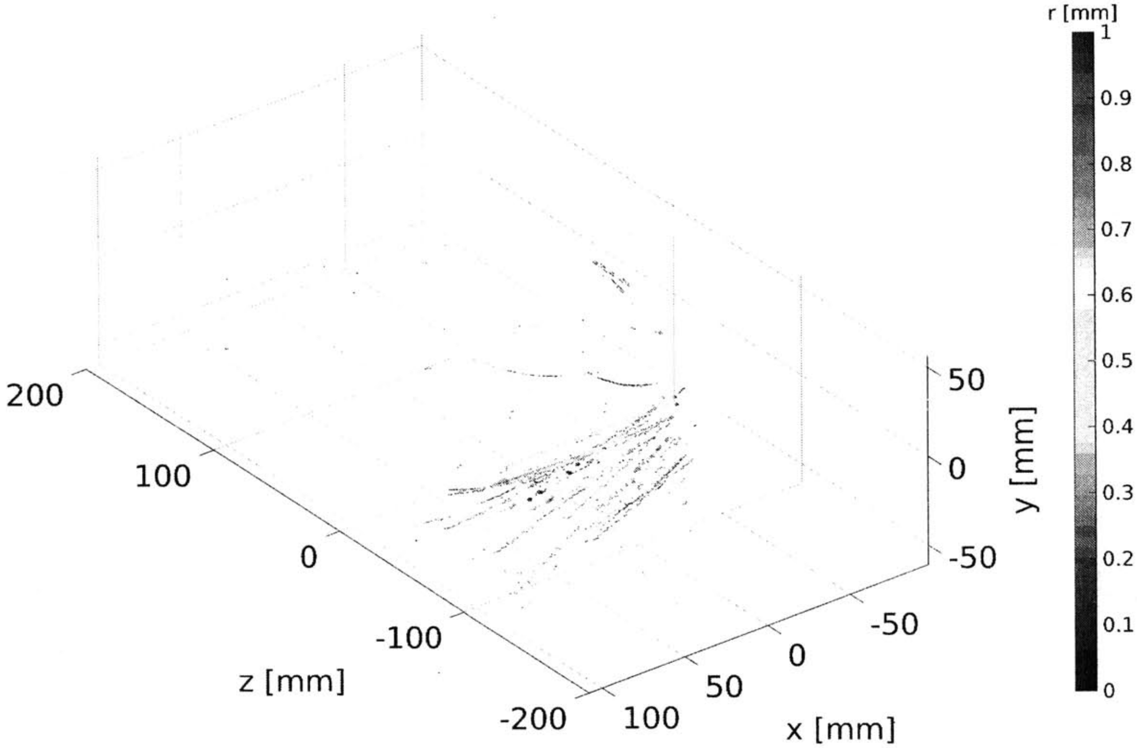

Figure 4-33: Isometric view of 3D sneeze cloud in Trial 4. All droplets detected at every time step are plotted (therefore droplets shown are not all unique). The gray arrow points in the direction of the overall mean velocity vector of all droplets.

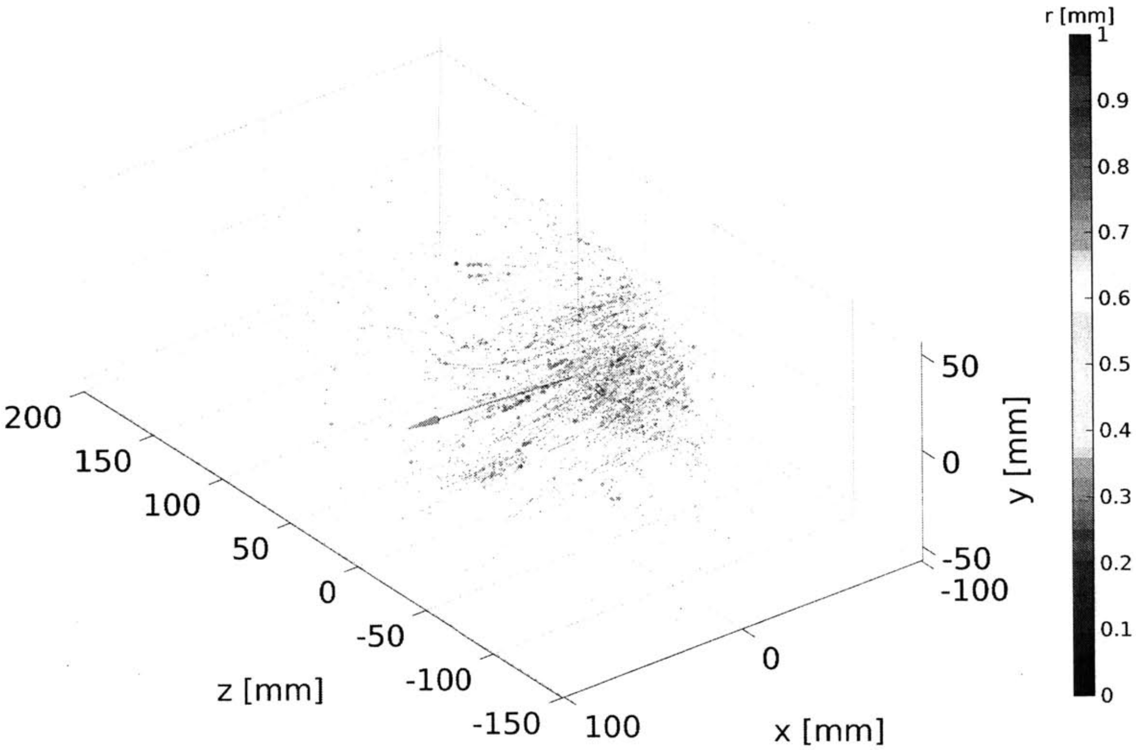

Figure 4-34: Isometric view of 3D sneeze cloud in Trial 5. All droplets detected at every time step are plotted (therefore droplets shown are not all unique). The gray arrow points in the direction of the overall mean velocity vector of all droplets.

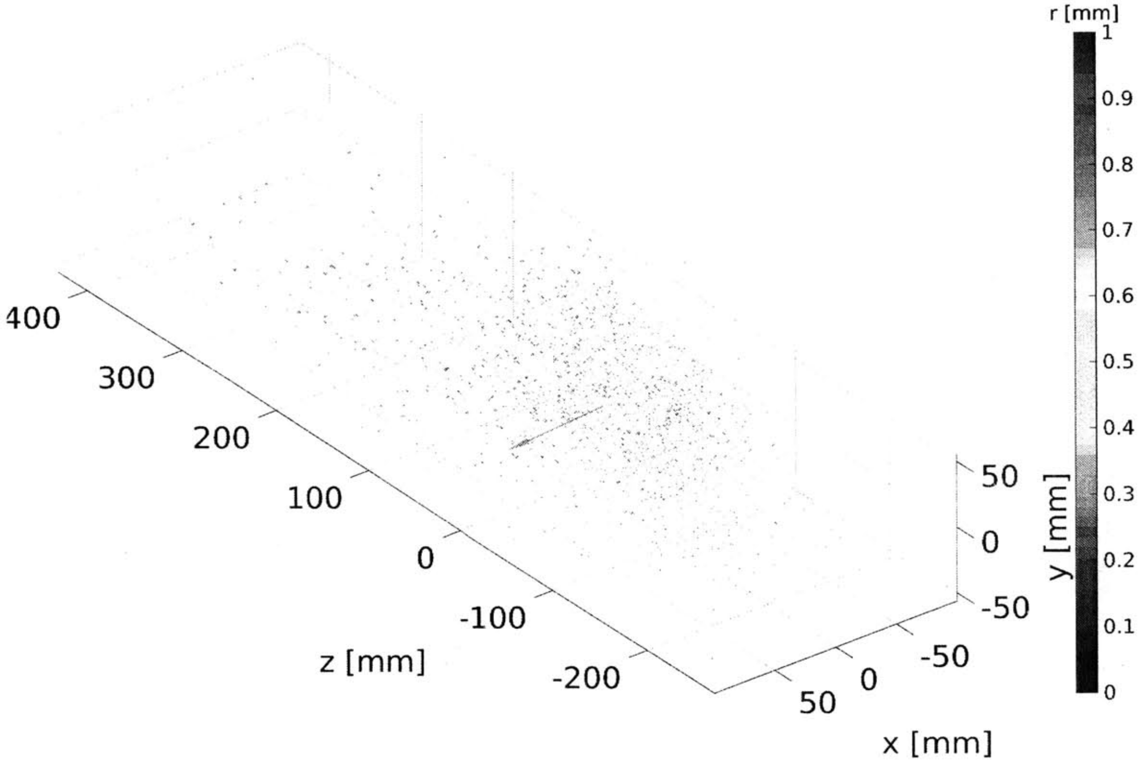

Figure 4-35: Isometric view of 3D sneeze cloud in Trial 6. All droplets detected at every time step are plotted (therefore droplets shown are not all unique). The gray arrow points in the direction of the overall mean velocity vector of all droplets.

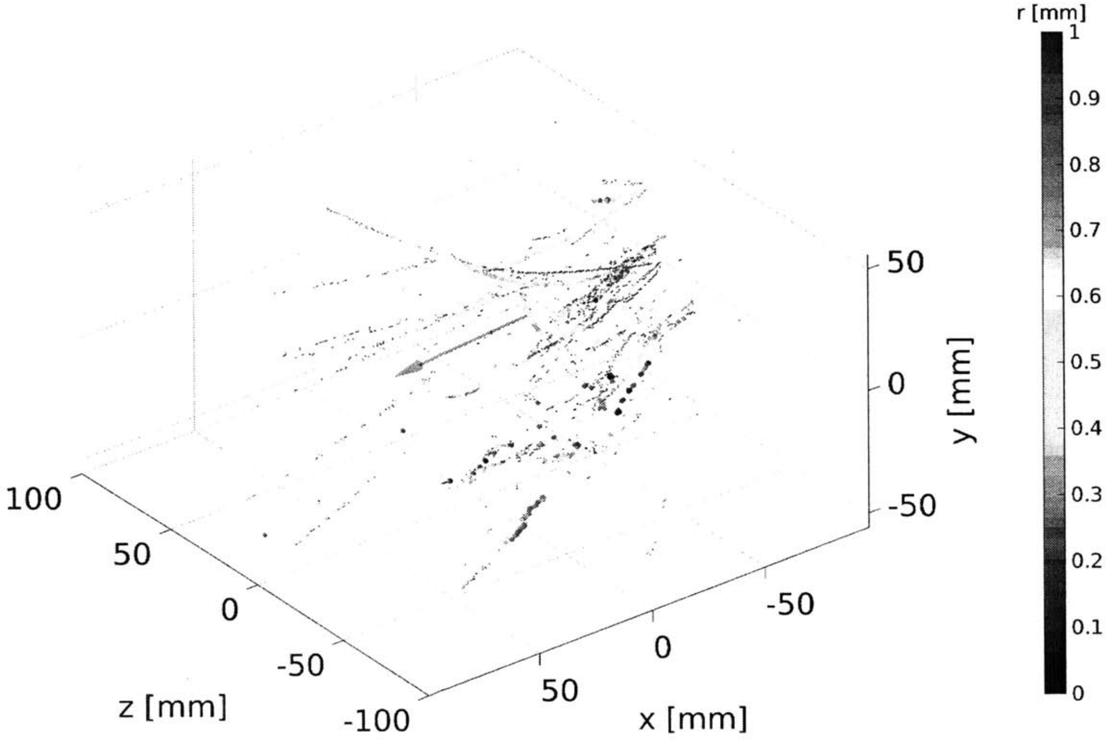

Figure 4-36: Isometric view of 3D sneeze cloud in Trial 7. All droplets detected at every time step are plotted (therefore droplets shown are not all unique). The gray arrow points in the direction of the overall mean velocity vector of all droplets.

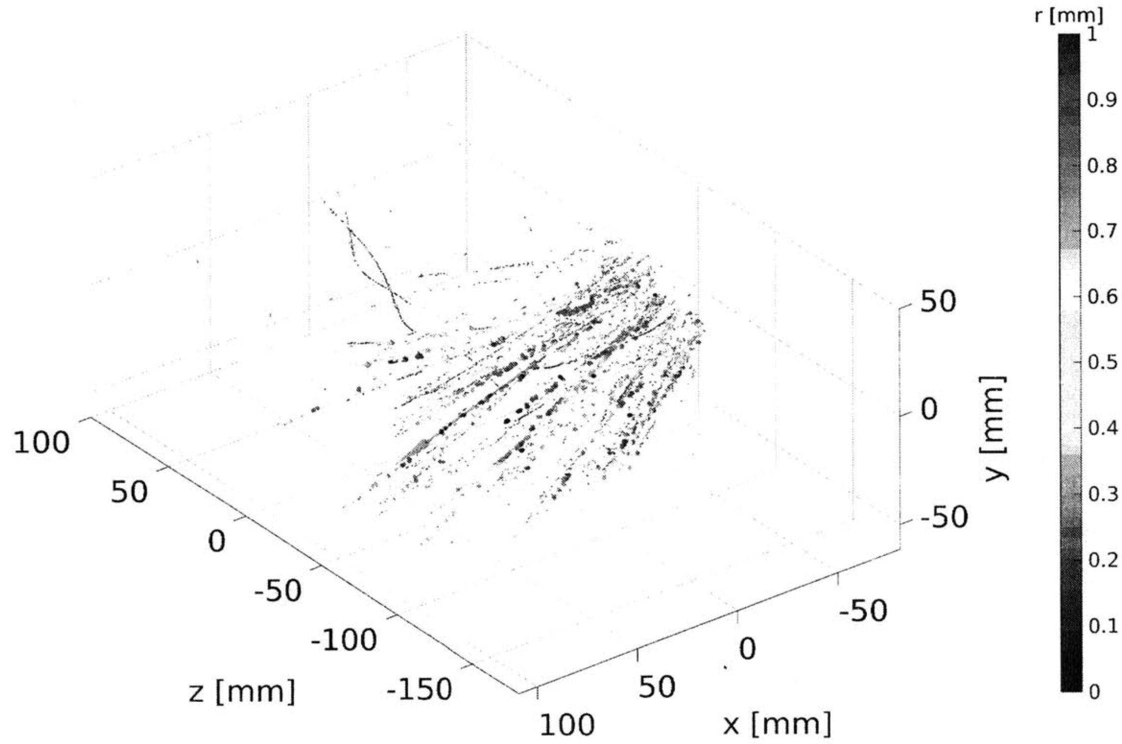

Figure 4-37: Isometric view of 3D sneeze cloud in Trial 8. All droplets detected at every time step are plotted (therefore droplets shown are not all unique). The gray arrow points in the direction of the overall mean velocity vector of all droplets.

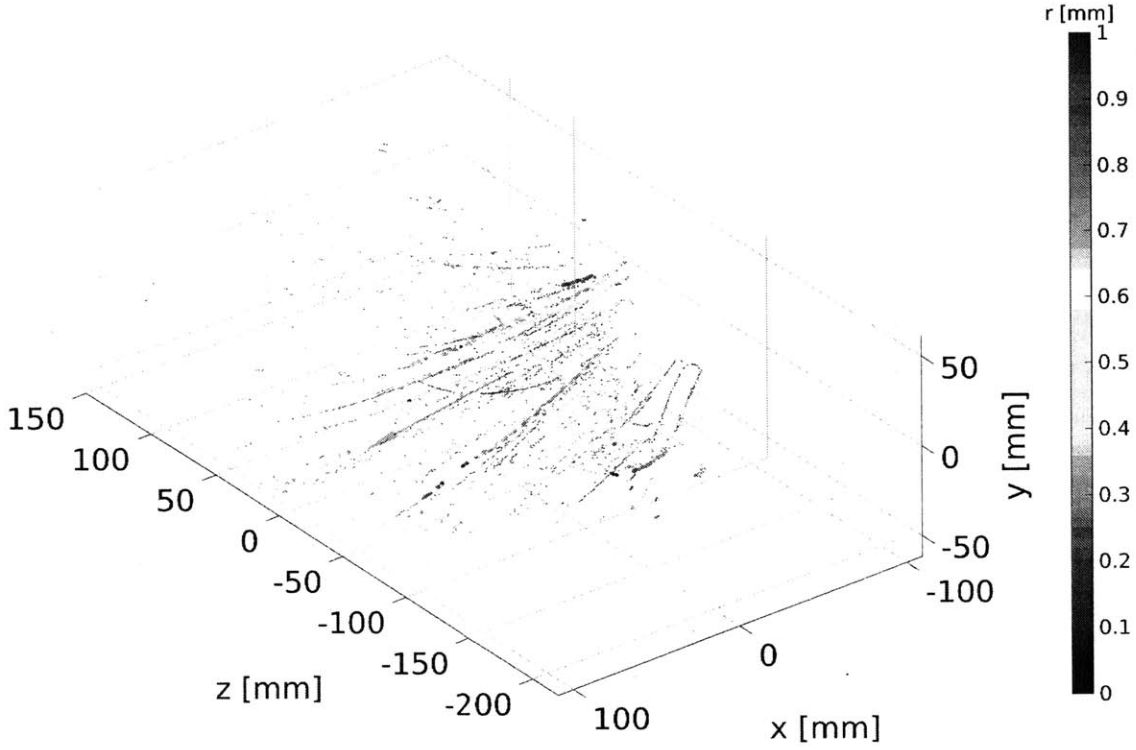

Figure 4-38: Isometric view of 3D sneeze cloud in Trial 9. All droplets detected at every time step are plotted (therefore droplets shown are not all unique). The gray arrow points in the direction of the overall mean velocity vector of all droplets.

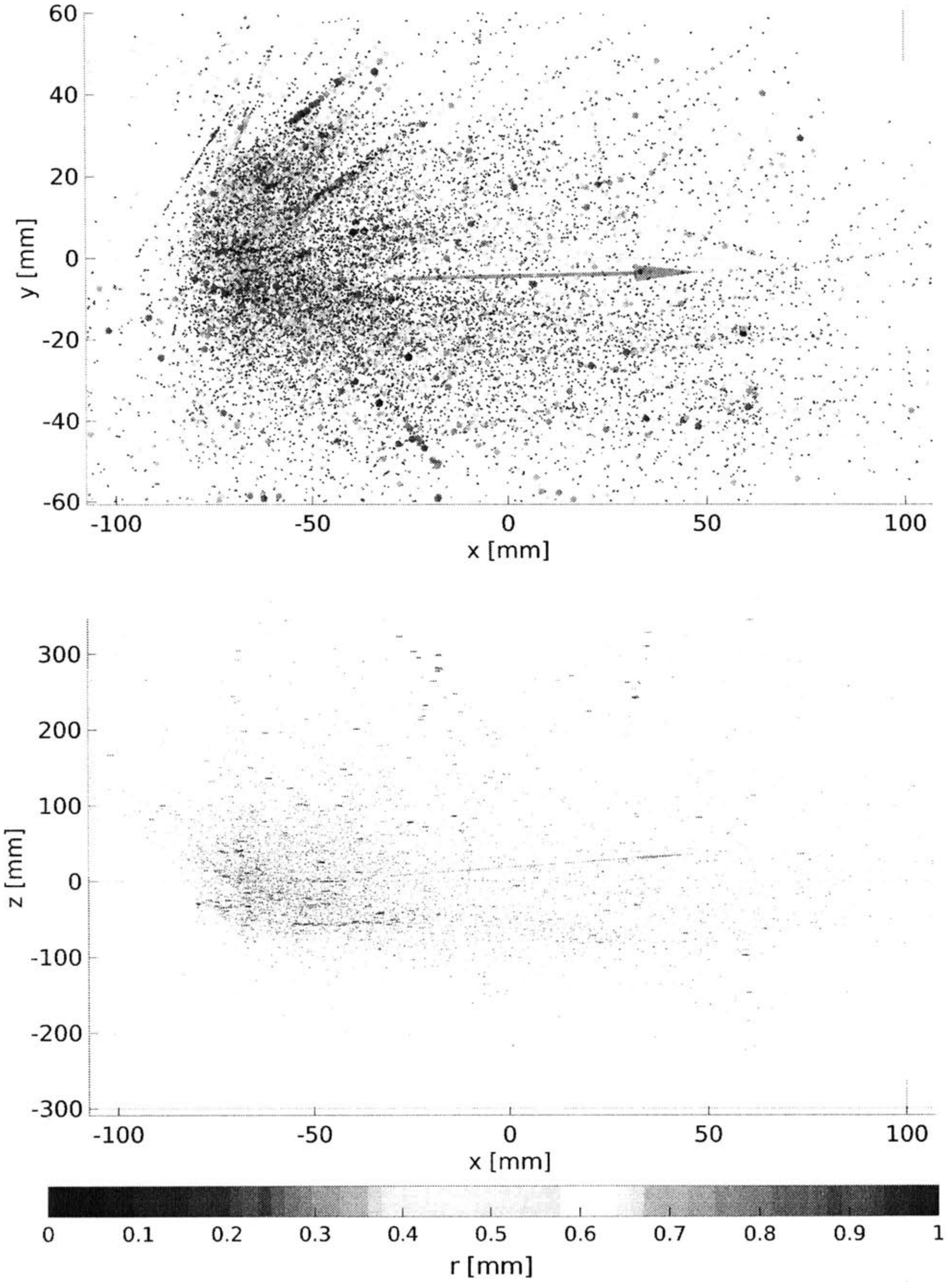

Figure 4-39: (Top) $x - y$ view of 3D sneeze cloud in Trial 1. (Bottom) $x - z$ view of 3D sneeze cloud. The gray arrow points in the direction of the overall mean velocity vector of all droplets.

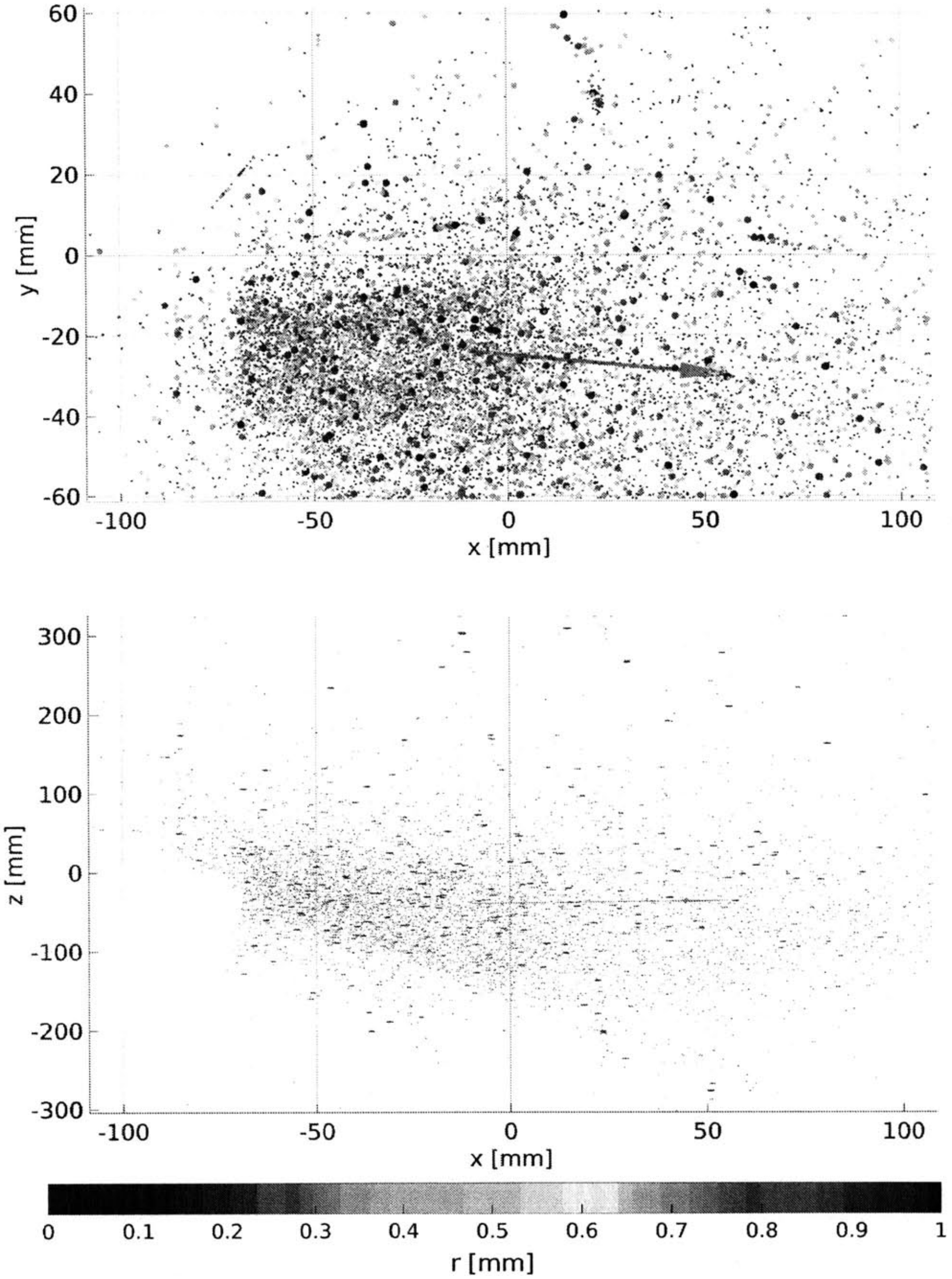

Figure 4-40: (Top) $x-y$ view of 3D sneeze cloud in Trial 2. (Bottom) $x-z$ view of 3D sneeze cloud. The gray arrow points in the direction of the overall mean velocity vector of all droplets.

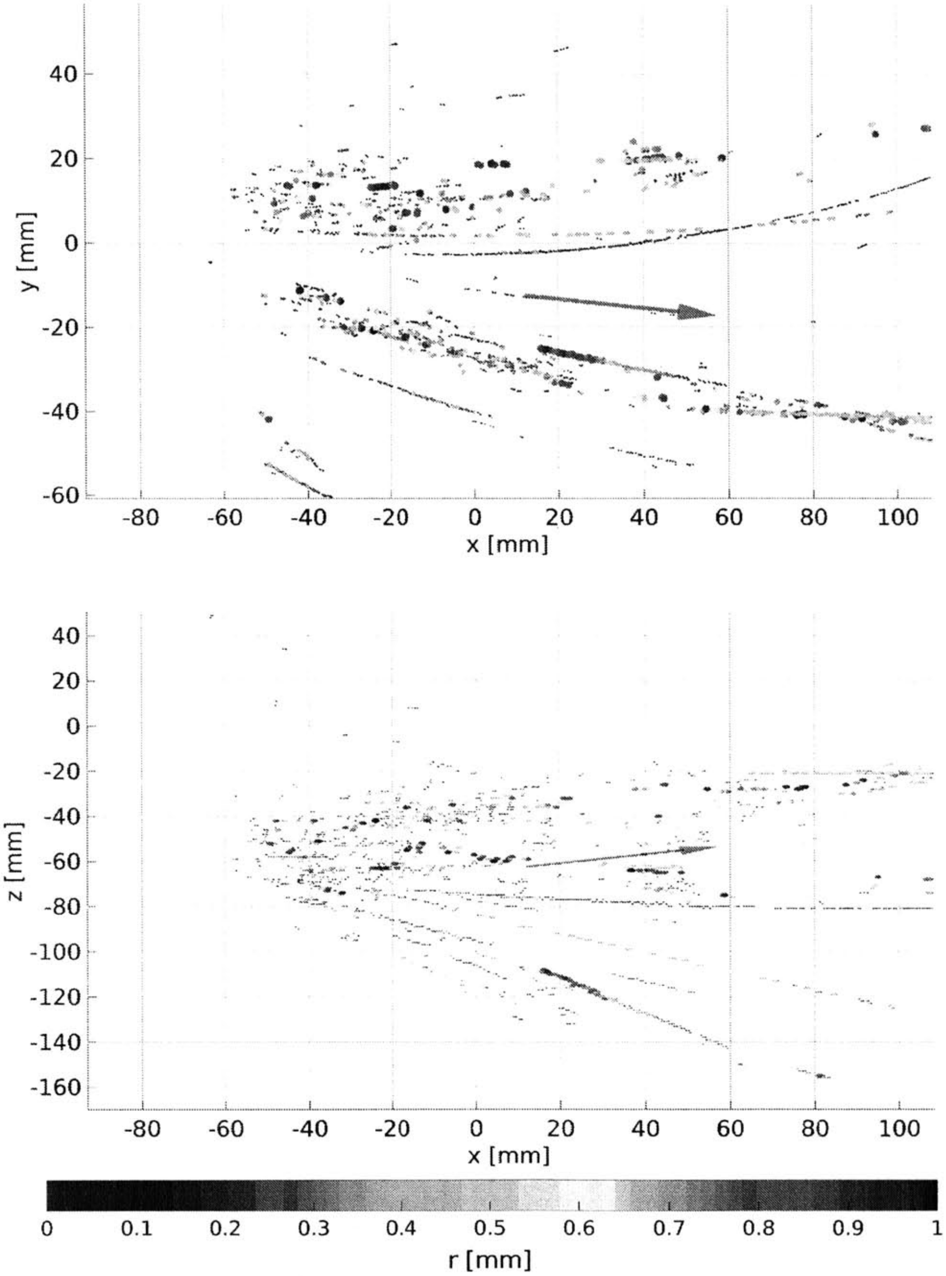

Figure 4-41: (Top) $x - y$ view of 3D sneeze cloud in Trial 3. (Bottom) $x - z$ view of 3D sneeze cloud. The gray arrow points in the direction of the overall mean velocity vector of all droplets.

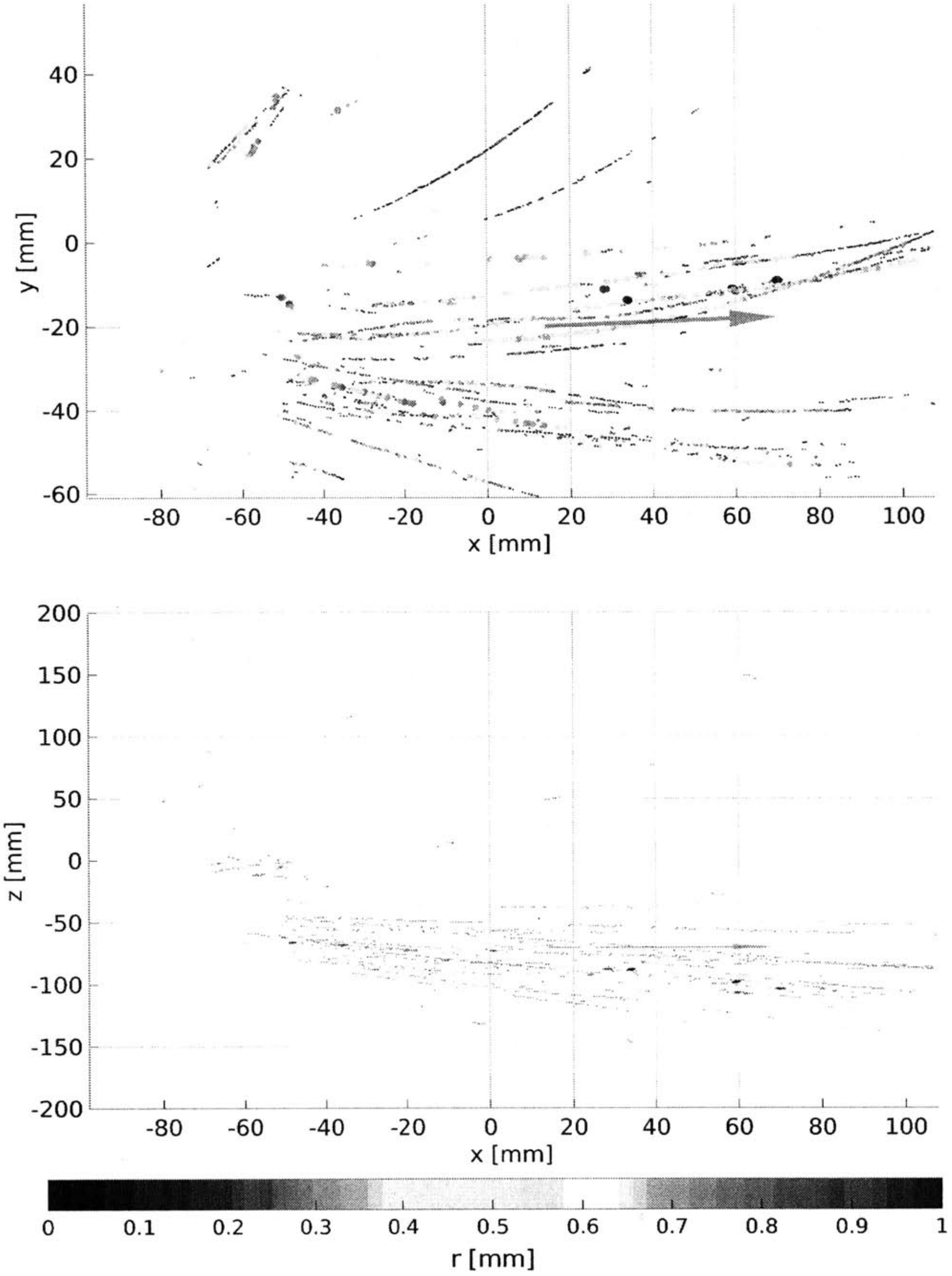

Figure 4-42: (Top) $x - y$ view of 3D sneeze cloud in Trial 4. (Bottom) $x - z$ view of 3D sneeze cloud. The gray arrow points in the direction of the overall mean velocity vector of all droplets.

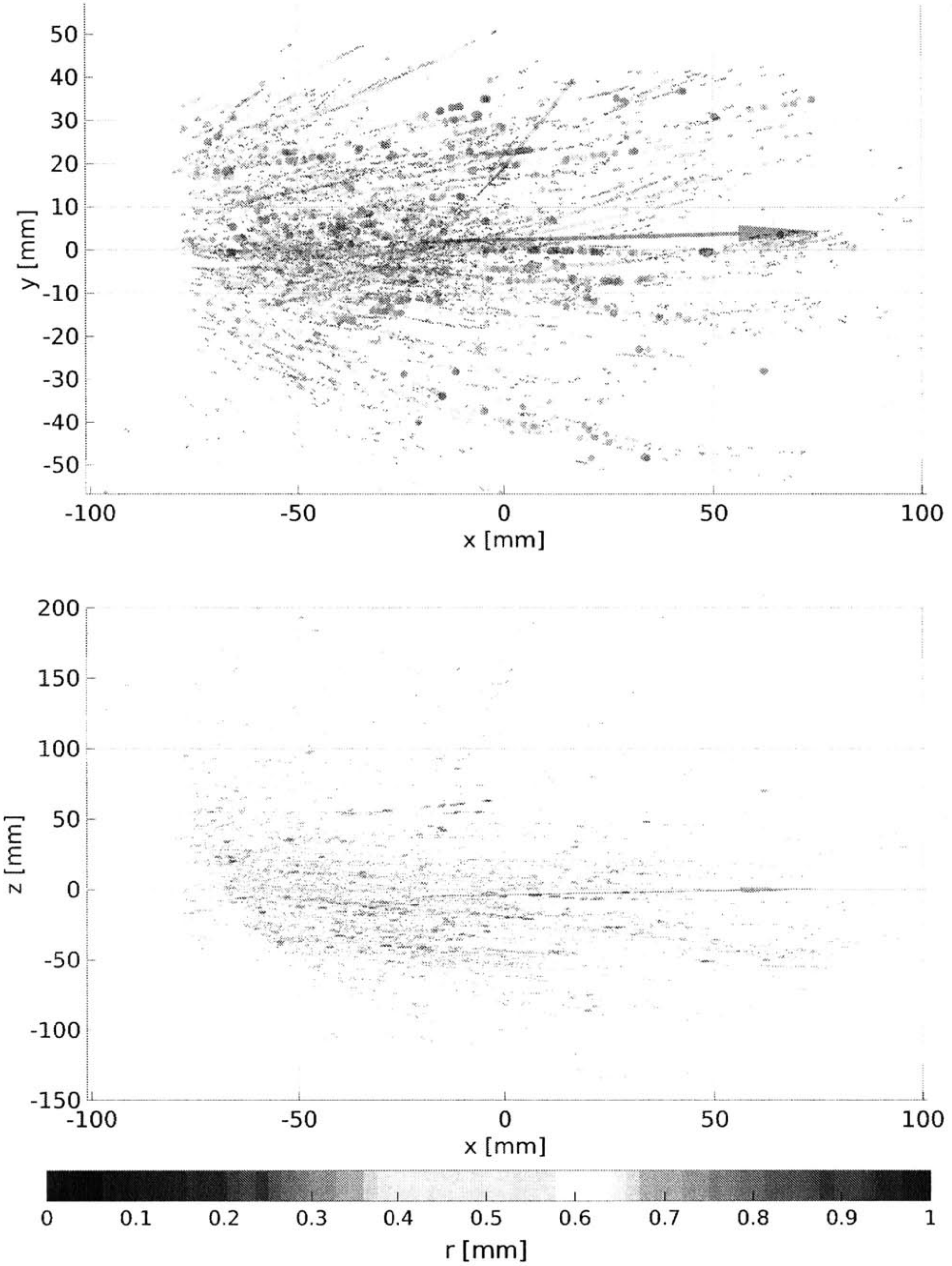

Figure 4-43: (Top) $x - y$ view of 3D sneeze cloud in Trial 5. (Bottom) $x - z$ view of 3D sneeze cloud. The gray arrow points in the direction of the overall mean velocity vector of all droplets.

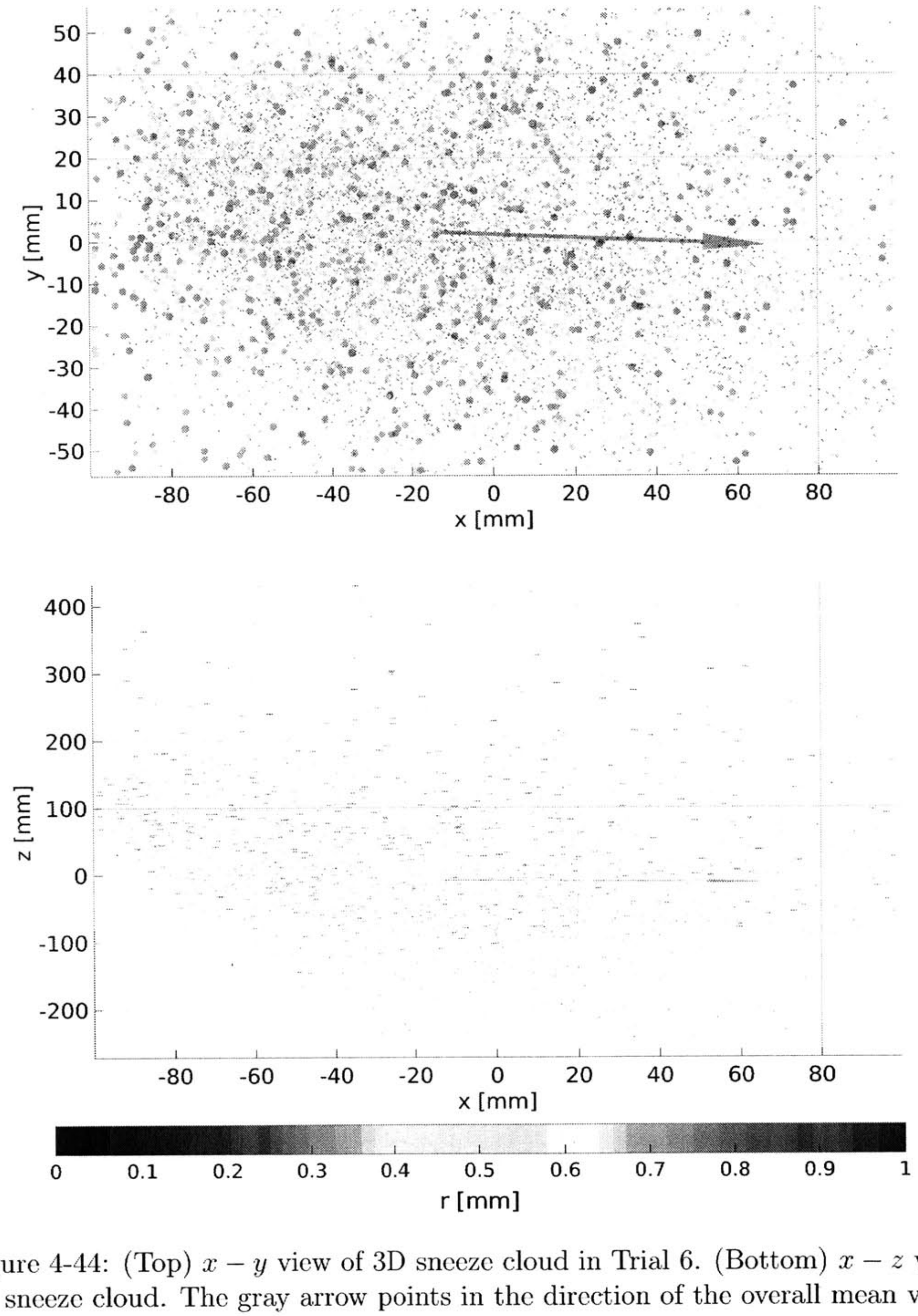

Figure 4-44: (Top) $x - y$ view of 3D sneeze cloud in Trial 6. (Bottom) $x - z$ view of 3D sneeze cloud. The gray arrow points in the direction of the overall mean velocity vector of all droplets.

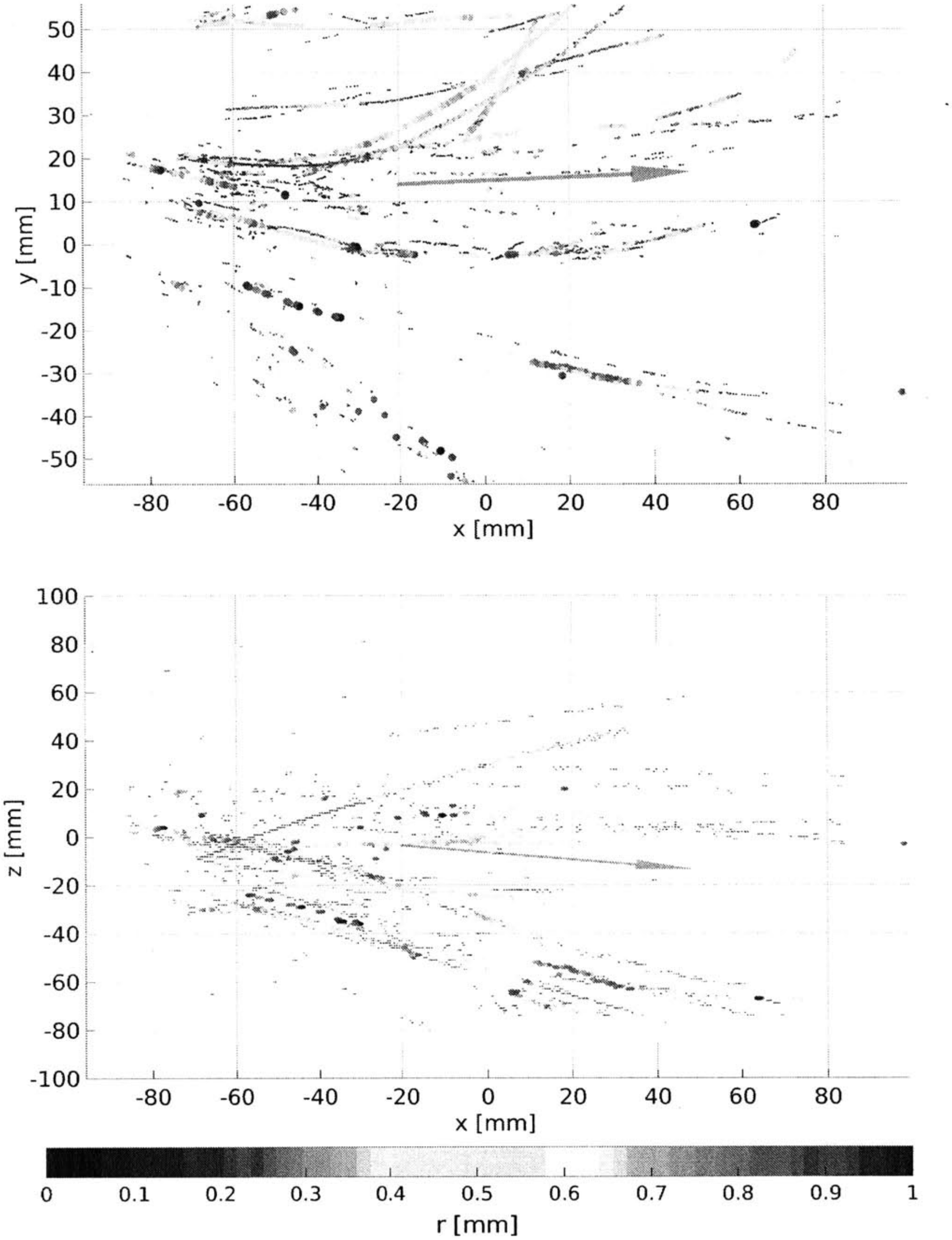

Figure 4-45: (Top) $x - y$ view of 3D sneeze cloud in Trial 7. (Bottom) $x - z$ view of 3D sneeze cloud. The gray arrow points in the direction of the overall mean velocity vector of all droplets.

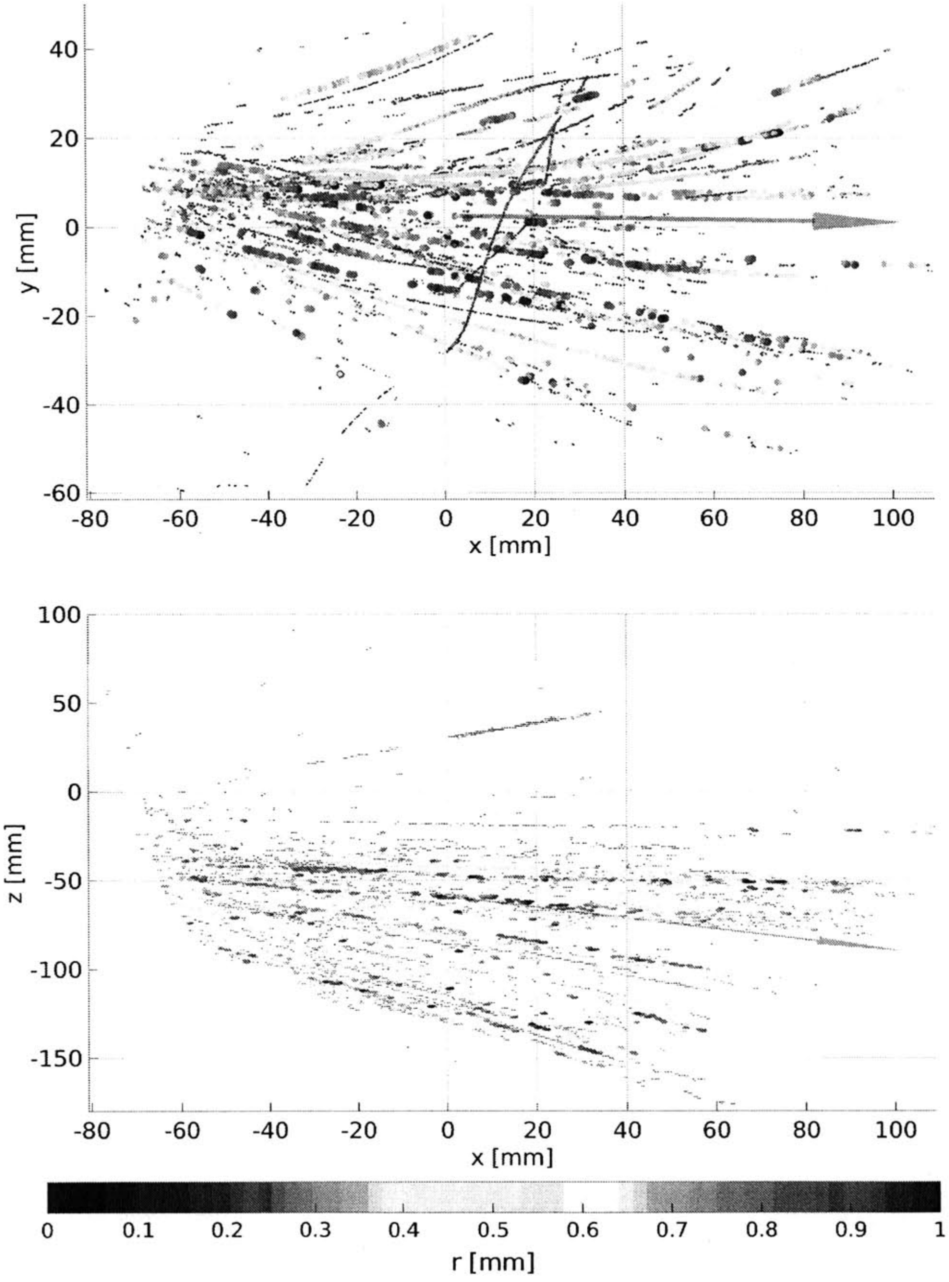

Figure 4-46: (Top) $x - y$ view of 3D sneeze cloud in Trial 8. (Bottom) $x - z$ view of 3D sneeze cloud. The gray arrow points in the direction of the overall mean velocity vector of all droplets.

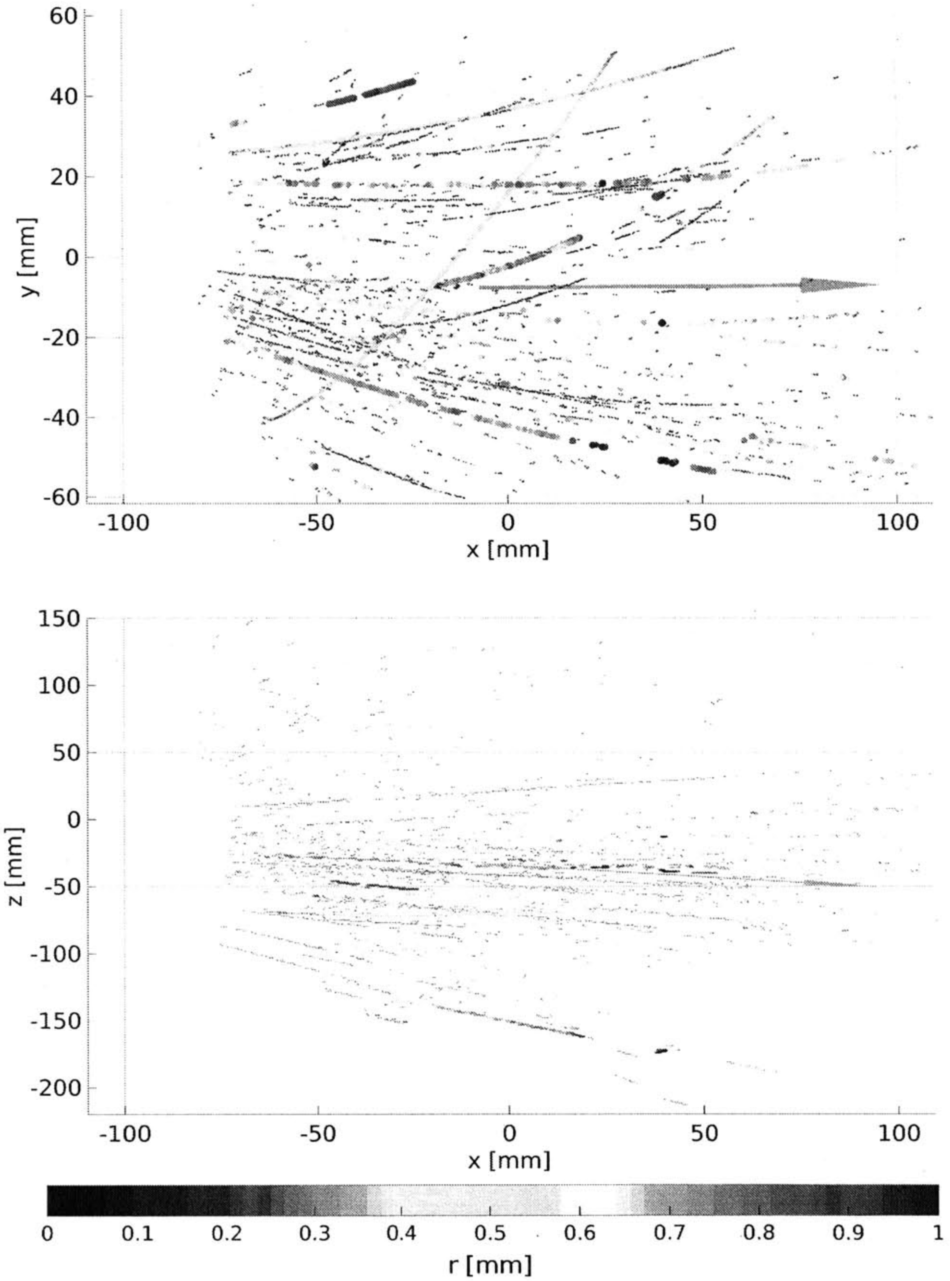

Figure 4-47: (Top) $x-y$ view of 3D sneeze cloud in Trial 9. (Bottom) $x-z$ view of 3D sneeze cloud. The gray arrow points in the direction of the overall mean velocity vector of all droplets.

Chapter 5

Summary and Conclusions

This thesis presents the analysis of several multiphase spray flows using advanced high speed imaging methods. Synthetic Aperture Feature Extraction (SAFE) is a new light-field imaging based method for identifying and quantifying flow features in a multiphase flow. SAFE is detailed herein and applied to bubble and sneeze flows. The use of high speed imaging combined with light field imaging allows for the resolution of flow features in three-dimensions and time (3D+T).

The SAFE technique allows the measurement of flow feature position and velocimetry in 3D+T, enabling a complete understanding of the flow dynamics. This thesis presents the first application of SAFE to sneeze flows, yielding a more complete description of the dynamics of sneeze droplets within a selected volumetric region. This type of analysis can potentially lead to a reduction in airborne disease transmission and improvements in ventilation system design. The insight gained into viscoelastic sneeze flows and the discovery of new sneeze related fluid phenomena, can also lead to a more thorough understanding of other flows that share similar characteristics.

The generality and resolving capabilities of the SAFE method make it ideal for the analysis of a wide variety of 3D scenes as long as features are visible and not completely occluded. SAFE is independent of the phases of matter being imaged and the nature of the scene, as well as the Reynolds number and other dimensionless parameter regimes of the flow. As long as the cameras and lighting are sufficient to image the flow without streaking or blur, the flow features of interest can be determined with adequate spatial and temporal resolution. SAFE only requires cameras to be located on one side of the scene being imaged, making it ideal for problems where optical access is limited. Also, since the cameras are clustered in an array in one main location, the lighting setup can be simplified as well.

The SAFE method is compatible with existing and emerging light field imaging hardware implementations that have been developed for use in both research and commercial applications. The inclusion of light field imaging sensors in mobile devices could enable new applications that rely on depth or size information or the ability to refocus images and view scenes from different angles. The combination of the Synthetic Aperture Feature Extraction method with the appropriate hardware can enable better engineering designs, improved measurements of natural phenomena, and validation of theory and numerical codes.

In this thesis, SAFE was applied to two distinct fluid problems: soap bubbles flowing in air and sneeze flows. The flow of soap bubbles in air was investigated experimentally as a proof of concept of the SAFE technique. Simulations using the open source software package Blender [18] were also used to validate this method. Cameras, lights, and spherical objects in a scene were simulated in both dark field and light field setups to test 3D scene reconstruction.

Sneeze ejecta emitted close to the mouth exit were studied using both 2D high-speed imaging, as well as the 3D SAFE method. 2D videos of these viscoelastic fluid flows were recorded simultaneously using both side and top view high-speed cameras to investigate the dynamics of ejecta and the stages of atomization. Sheet, or "bag" formation, ligament appearance and elongation, beads-on-a-string, and droplet merger were observed during the lifetime of each sneeze recorded. The top and side views demonstrated the highly 3D nature of sneezes. To capture the extent of sneezes in 3D, an array of nine high-speed cameras (in addition to a separate side camera to track the sneezer's head motion) was used to perform SAFE 3D reconstruction of the flow over time. Droplet centroids, radii, velocities, accelerations, and other flow characteristics were extracted over the course of the sneeze.

In summary, the main contributions of this thesis include:

- Development of the Synthetic Aperture Feature Extraction (SAFE) method as an extension of the SA refocusing technique. This method enables the reconstruction of sphere-like blobs in 3D over time.

- Validation of the SAFE method via camera, scene, and light simulations with both dark and light field setups. The impact of camera array configuration on the percent error in reconstruction was also evaluated.

- Three-dimensional experimental analysis of flow of soap bubbles in air to validate the SAFE method.

- Identification of previously unobserved dynamics and features of sneeze ejecta near the exit of the mouth, including bags and beads-on-a-string.

- Quantitative analysis of near-field sneeze flow features. Droplets of mucosalivary fluid were located in both 2D and 3D over time using high speed video and the SAFE method. Centroids, radii, velocities, and other flow measurements were calculated over time.

Moving forward there are several areas that still warrant further investigation with the SAFE method:

- Further analysis of 3D sneeze ejecta in both the near and far field. Collecting data from more sneezer test subjects would yield more statistically robust sneeze ejecta data.

- Automation of the selection of appropriate pre-processing and clustering algorithms and parameters to be used for SAFE when processing a particular data set, possibly via machine learning.

- Application of the SAFE method to other types of multiphase flows that have previously been difficult to measure in 3D+T, including optically dense fuel sprays.

- Comparison of experimental SAFE results with 3D computational fluid dynamics simulations for further validation.

- Application of the SAFE method to three-phase flows consisting of liquid, solid, and gaseous matter.
- Extension of the SAFE method to resolve shapes in 3D that are not well approximated by spheres.

Bibliography

[1] Nasser Ashgriz. *Handbook of atomization and sprays: theory and applications.* Springer Science & Business Media, 2011.

[2] T. J. Atherton and D. J. Kerbyson. Size invariant circle detection. *Image and Vision Computing*, 17:795–803, 1999.

[3] Abhishek Bajpayee. *3D Particle Tracking Velocimetry using Synthetic Aperture Imaging.* PhD thesis, Massachusetts Institute of Technology, 2014.

[4] Abhishek Bajpayee and Alexandra H. Techet. 3d particle tracking velocimetry (ptv) using high speed light field imaging. In *PIV13; 10th International Symposium on Particle Image Velocimetry, Delft, The Netherlands, July 1-3, 2013.* Delft University of Technology, Faculty of Mechanical, Maritime and Materials Engineering, and Faculty of Aerospace Engineering, 2013.

[5] A. S. Banner. Cough: physiology, evolution, and treatment. *Lung*, 164:79–92, 1986.

[6] R. Bansil and B. S. Turner. Mucin structure, aggregation, physiological functions and biomedical applications. *Current Opinion in Colloid & Interface Science*, 11:164–170, 2006.

[7] Raynal Bde, T. E. Hardingham, D. J. Thornton, and J. K. Sheehan. gel-forming properties of saliva. *Biochem J*, 296:289–296, 2002.

[8] Jesse Belden, Tadd T. Truscott, Michael Axiak, and Alexandra H. Techet. Three-dimensional synthetic aperture particle image velocimetry. *Measurement Science and Technology*, 21:1–21, 2010.

[9] Jesse Belden, Tadd T. Truscott, Sai Ravela, and Alexandra H. Techet. Three-dimensional bubble field resolution using synthetic aperture imaging: Application to a plunging jet. *Experiments in Fluids*, 53:839–861, 2012.

[10] Simon Benita. *Microencapsulation.* Marcel Dekker, 1996.

[11] Pradeep P Bhat, Santosh Appathurai, Michael T Harris, Matteo Pasquali, Gareth H McKinley, and Osman A Basaran. Formation of beads-on-a-string structures during break-up of viscoelastic filaments. *Nature Physics*, 6(8):625–631, 2010.

[12] D. Blair and E. Dufresne. *The Matlab Particle Tracking Code Repository.* Georgetown University, 2015. URL `http://site.physics.georgetown.edu/matlab/`.

[13] L. Bourouiba. Understanding the transmission of H5N1. *CAB Reviews: Perspectives in Agriculture, Veterinary Sciences, Nutrition and Natural Resources*, 17:1–9, 2013.

[14] L. Bourouiba, E. Dehandschoewercker, and J. W. M. Bush. The fluid dynamics of coughing and sneezing. In *Refereed proceedings of the International Society of Indoor Air Quality and Climate 10th Healthy Buildings Conference Brisbane.* AU, 2012.

[15] L. Bourouiba, E. Dehandschoewercker, and J. W. M. Bush. Violent expiratory events: on coughing and sneezing. *J Fluid Mech*, 745:537–563, 2014.

[16] Lydia Bourouiba, Eline Dehandschoewercker, and John W. M. Bush. Violent expiratory events: on coughing and sneezing. *Journal of Fluid Mechanics*, 745: 537–563, 2014.

[17] CDC. Emergence of avian influenza A(H7N9) virus causing severe human illness. Report. *Morbidity and Moratlity Weekly*, 62(18):366–371, 2013.

[18] Blender Online Community. *Blender - a 3D modelling and rendering package.* Blender Foundation, Blender Institute, Amsterdam, 2015. URL `http://www.blender.org`.

[19] F. Culick. Comments on a Ruptured Soap Film. *Air pp*, pages 1128–1129, 1960.

[20] J. Dekker, Rossen Jwa, H. A. Büller, and Einerhand Awc. The MUC family: an obituary. *Trends in Biochemical Sciences*, 27:126–131, 2002.

[21] J. P. Duguid. The size and the duration of air-carriage of respiratory droplets and droplet-nuclei. *The Journal of Hygiene*, 44(6):471–479, 1946.

[22] J. Duparre. Fabrication process for mastering imaging lens arrays, July 31 2012. URL `https://www.google.com/patents/US8231814`. US Patent 8,231,814.

[23] J. Eggers and E. Villermaux. Physics of liquid jets. *Reports on Progress in Physics*, 71, 2008.

[24] Liang-Shih Fan and Chao Zhu. Size and properties of particles. In *Principles of Gas–Solid Flows*, pages 3–45. Cambridge University Press, 1998. ISBN 9780511530142. URL `http://dx.doi.org/10.1017/CBO9780511530142.002`. Cambridge Books Online.

[25] Todd D Fansler and Scott E Parrish. Spray measurement technology: a review. *Measurement Science and Technology*, 26(1):012002, 2015. URL `http://stacks.iop.org/0957-0233/26/i=1/a=012002`.

[26] ASTM (American Society for Testing and Materials). Standard e 1620: standard terminology relating to liquid particles and atomization. *Annual book of ASTM standards*, 2004.

[27] J. B. Grotberg. Pulmonary flow and transport phenomena. *Annu Rev Fluid Mech*, 26:529–571, 1994.

[28] J. K. Gupta, C.-H. Lin, and Q. Chen. Flow dynamics and characterization of a cough. *Indoor air*, 19(6):517–525, 2009.

[29] Richard Hartley and Andrew Zisserman. *Multiple view geometry in computer vision.* Cambridge university press, 2003.

[30] S. Haward, J. Odell, M. Berry, and T. Hall. Extensional rheology of human saliva. *Rheologica Acta*, 50:869–879, 2011.

[31] Philip A. Hughes. *Beams and jets in astrophysics*, volume 19. Cambridge University Press, 1991.

[32] Google Inc. Google jump, 2015. URL `https://www.google.com/get/cardboard/jump/`.

[33] Aaron Isaksen, Leonard McMillan, and Steven J. Gortler. Dynamically reparameterized light fields. In *Proceedings of the 27th annual conference on Computer graphics and interactive techniques*, pages 297–306. ACM Press/Addison-Wesley Publishing Co., 2000.

[34] James Jea. de Burgh Daly m Nasal Reflexes: Section of Laryngology. *Proc Roy Soc Med*, 62:1287–1293, December 1969.

[35] G. Johnson, L. Morawska, Z. Ristovski, M. Hargreaves, K. Mengersen, C. Chao, M. Wan, Y. Li, X. Xie, D. Katoshevski, and S. Corbett. Modality of human expired aerosol size distributions. *Journal of Aerosol Science*, 42:839–851, 2011.

[36] M. Kesimer, A. M. Makhov, J. D. Griffith, P. Verdugo, and J. K. Sheehan. Unpacking a gel-forming mucin : a view of MUC5B organization after granular release. *Au J Physiol Lung Cell Mol Physiol*, 289:15–22, 2010.

[37] JC Lasheras and EJ Hopfinger. Liquid jet instability and atomization in a coaxial gas stream. *Annual Review of Fluid Mechanics*, 32(1):275–308, 2000.

[38] Henri Lhuissier and Emmanuel Villermaux. Bursting bubble aerosols. *Journal of Fluid Mechanics*, 696:5–44, 2012.

[39] Sung-Piau Lin. *Breakup of liquid sheets and jets.* Cambridge University Press, 2003.

[40] Kyle Lynch. *Development of a 3-D fluid velocimetry technique based on light field imaging.* PhD thesis, Auburn University, 2011.

[41] Jiri Matas, Ondrej Chum, Martin Urban, and Tomás Pajdla. Robust wide-baseline stereo from maximally stable extremal regions. *Image and vision computing*, 22(10):761–767, 2004.

[42] Leah Mendelson and Alexandra H. Techet. Quantitative wake analysis of a freely swimming fish using 3d synthetic aperture piv. *Experiments in Fluids*, 56(7):1–19, 2015.

[43] L. Morawska, G. Johnson, Z. Ristovski, M. Hargreaves, K. Mengersen, S. Corbett, C. Chao, Y. Li, and D. Katoshevski. Size distribution and sites of origin of droplets expelled from the human respiratory tract during expiratory activities. *J Aerosol Sci*, 40:256–269, 2009.

[44] Arrate Muñoz, Thierry Blu, and Michael Unser. Least-squares image resizing using finite differences. *Image Processing, IEEE Transactions on*, 10(9):1365–1378, 2001.

[45] Ren Ng. *Digital light field photography*. PhD thesis, stanford university, 2006.

[46] Ren Ng, Marc Levoy, Mathieu Brédif, Gene Duval, Mark Horowitz, and Pat Hanrahan. Light field photography with a hand-held plenoptic camera. *Computer Science Technical Report CSTR*, 2(11), 2005.

[47] David Nistér and Henrik Stewénius. Linear time maximally stable extremal regions. In David Forsyth, Philip Torr, and Andrew Zisserman, editors, *Computer Vision - ECCV 2008*, volume 5303 of *Lecture Notes in Computer Science*, pages 183–196. Springer Berlin Heidelberg, 2008.

[48] R. S. Papineni and F. S. Rosenthal. The size distribution of droplets in the exhaled breath of healthy human subjects. *J Aerosol Med*, 10:105–116, 1997.

[49] Ulrich Perwass and Christian Perwass. Digital imaging system, plenoptic optical device and image data processing method, December 31 2013. US Patent 8,619,177.

[50] A Picard, RS Davis, M Gläser, and K Fujii. Revised formula for the density of moist air (cipm-2007). *Metrologia*, 45(2):149–155, 2008.

[51] M. Pilch and C. A. Erdman. Use of breakup time data and velocity history data to predict the maximum size of stable fragments for acceleration-induced breakup of a liquid drop. *Int J Multiphase Flow*, 13:741–757, 1987.

[52] Stephen B Pope. *Turbulent flows*. Cambridge university press, 2000.

[53] E Reyssat, F Chevy, A-L Biance, L Petitjean, and D Quéré. Shape and instability of free-falling liquid globules. *EPL (Europhysics Letters)*, 80(3):34005, 2007.

[54] K. A. Sallam, C. Aalburg, and G. M. Faeth. Breakup of Round Nonturbulent Liquid Jets in Gaseous Crossflow. *AIAA Journal*, 42:2529–2540, 2004.

[55] B. E. Scharfman and A. H. Techet. Bag instabilities. *Physics of Fluids*, 24, 2012.

[56] B. E. Scharfman, Bush Jwm, and A. Techet. Hydrodynamic instabilities in round liquid jets in gaseous crossflow. *Proc*, 25, 2013.

[57] Barry E. Scharfman and Alexandra H. Techet. Bag instabilities. *Physics of Fluids (1994-present)*, 24(9):091112, 2012.

[58] Barry E. Scharfman and Alexandra H. Techet. Three-dimensional spray analysis using light field imaging. In *Proceedings of ILASS Europe 26th Annual Conference on Liquid Atomization and Spray Systems*, Bremen, Germany, 2014.

[59] Barry E. Scharfman and Alexandra H. Techet. Three-dimensional droplet centroid and size measurement using light field imaging. In *Proceedings of ILASS Americas 26th Annual Conference on Liquid Atomization and Spray Systems*, Portland, OR, USA, 2014.

[60] Barry E. Scharfman and Alexandra H. Techet. Three-dimensional synthetic aperture feature extraction in multiphase flows. In *Proceedings of ILASS Americas 27th Annual Conference on Liquid Atomization and Spray Systems*, Raleigh, North Carolina, USA, 2015.

[61] Barry E. Scharfman, Douglas P. Hart, and Alexandra H. Techet. Light field imaging of turbulent liquid sheet breakup in air. In *Proceedings of the 10th International Symposium on Particle Image Velocimetry - PIV13*, Deflt, The Netherlands, 2013.

[62] R. G. Schipper, E. Silletti, and M. H. Vingerhoeds. Saliva as research material: Biochemical, physicochemical and practical aspects. *Archives of Oral Biology*, 52:1114–1135, 2007.

[63] G. S. Settles. Fluid mechanics and homeland security. *Annu Rev Fluid Mech*, 38:87–110, 2006.

[64] C. M. Sipperley and W. D. Bachalo. Volumetric imaging and multi-angle illumination for dense sprays characterization. In *Proceedings of the 25th ILASS Annual Conference on Liquid Atomization and Spray Systems*, Pittsburgh, PA, USA, 2013.

[65] J. R. Stokes and G. A. Davies. Viscoelasticity of human whole saliva collected after acid and mechanical stimulation. biorheology. *Biorhelogy*, 44:141–160, 2007.

[66] G. I. Taylor. The dynamics of thin sheets of fluid. iii. disintegration of fluid sheets. *Proc R Soc Lond Ser A*, 253:313–321, 1959.

[67] Alexandra H. Techet, Barry Ethan Scharfman, Thomas B. Milnes, and Douglas P. Hart. Light field imaging of fuel droplets and sprays. In *Proceedings of the 16th International Symposium on Applications of Laser Techniques to Fluid Mechanics*, Lisbon, Portugal, 2012.

[68] Clair E. Turner, Marshall W. Jennison, and Harold E. Edgerton. Public health applications of high-speed photography. *American Journal of Public Health and the Nations Health*, 31(4):319–324, 1941.

[69] Vaibhav Vaish, Bennett Wilburn, Neel Joshi, and Marc Levoy. Using plane + parallax for calibrating dense camera arrays. In *CVPR '04: Proceedings of the 2004 IEEE Computer Society Conference on Computer Vision and Pattern Recognition (CVPR'04) - Workshops*, pages 2–9, Washington, DC, USA, 2004. IEEE Computer Society.

[70] Vaibhav Vaish, Gaurav Garg, Eino-Ville Talvala, Emilio Antunez, Bennett Wilburn, M. Horowitz, and Marc Levoy. Synthetic aperture focusing using a shear-warp factorization of the viewing transform. In *CVPR '05: Proceedings of the 2005 IEEE Computer Society Conference on Computer Vision and Pattern Recognition (CVPR'05) - Workshops*, page 129, Washington, DC, USA, 2005. IEEE Computer Society.

[71] E. Villermaux. Fragmentation. *Annu Rev Fluid Mech*, 39:419–446, 2007.

[72] Emmanuel Villermaux and Benjamin Bossa. Single-drop fragmentation determines size distribution of raindrops. *Nature Physics*, 5(9):697–702, 2009.

[73] J. G. Widdicombe. Reflexes from the upper respiratory tract. *In: Handbook of physiology: the respiratory system II, pp*, pages 363–394, 1979.

[74] Bennett Wilburn, Neel Joshi, Vaibhav Vaish, Eino-Ville Talvala, Emilio Antunez, Adam Barth, Andrew Adams, Mark Horowitz, and Marc Levoy. High performance imaging using large camera arrays. *ACM Transactions on Graphics (TOG)*, 24(3):765–776, 2005.

[75] S. Yang, Lee Gwm, C. M. Chen, C. C. Wu, and K. P. Yu. The size and concentration of droplets generated by coughing in human subjects. *J Aerosol Med*, 20: 484–494, 2007.

[76] G. Zayas, M. Chiang, E. Wong, F. MacDonald, C. Lange, A. Senthilselvan, and M. King. Cough aerosol in healthy participants: fundamental knowledge to optimize droplet-spread infectious respiratory disease management. *BMC Pulmonary Medicine*, 12:1, 2012.

[77] Richard A. Zsigmondy and J. Alexander. *Colloids and the ultramicroscope; a manual of colloid chemistry and ultramicroscopy.* John Wiley & Sons, New York, 1909.